

Piezoelectrically Tunable Optical Cavities for the Gravitational Wave Detector LISA

DISSERTATION

zur Erlangung des akademischen Grades
doctor rerum naturalium
(Dr. rer. nat.)
im Fach Physik

eingereicht an der
Mathematisch-Naturwissenschaftlichen Fakultät I
Humboldt-Universität zu Berlin

von
Dipl.-Phys. Katharina Möhle

Präsident der Humboldt-Universität zu Berlin:
Prof. Dr. Jan-Hendrik Olbertz

Dekan der Mathematisch-Naturwissenschaftlichen Fakultät I:
Prof. Stefan Hecht, Ph.D.

Gutachter:

1. Prof. Achim Peters, Ph.D.
2. Prof. Dr. Oliver Benson
3. Prof. Dr. Claus Braxmaier

Tag der mündlichen Prüfung: 25.04.2013

Abstract

The Laser Interferometer Space Antenna (LISA) is a proposed space-based gravitational wave detector that aims to detect gravitational waves in the low frequency range from 0.1 mHz to 1 Hz, which is not accessible by ground-based detectors. It consists of three satellites whose distance is monitored by laser interferometry. The high frequency stability of the lasers required for this purpose is to be achieved with a three level noise reduction scheme. This includes a pre-stabilization stage that has to feature not only high stability but also tunability. The combination of these two requirements, in addition to the special demands of a space mission, are a challenging task for laser frequency stabilization.

One approach for such a tunable pre-stabilization is stabilizing a laser to an optical cavity with incorporated piezoelectric actuator. While this is not a new concept per se, it has never been realized with the required stability until now. Indeed, so far it has been generally assumed that piezo actuators so strongly affect the intrinsic stability of an optical cavity that they are not suited for high stability applications. The goal of this thesis was to close this gap of knowledge by investigating the performance of cavities with incorporated piezo actuators and to realize a highly stable version of such a cavity.

For this purpose a variety of piezo-tunable cavities have been built, using crystalline quartz, ceramic lead zirconate titanate (PZT), or lead zinc niobate - lead titanate (PZN-PT) single crystals. Lasers locked to these cavities show a frequency noise below $30 \text{ Hz}/\sqrt{\text{Hz}}$ for Fourier frequencies above 4 mHz and a relative frequency instability of 7×10^{-15} at integration times from 0.3 s to 8 s, which is the best result achieved with piezo-tunable cavities so far. By applying a voltage, the resonance frequencies of the cavities can be slowly tuned over more than one free spectral range ($> 1.5 \text{ GHz}$) with only a minor decrease in frequency stability. This wide tuning range allows full flexibility in the choice of the corresponding laser frequency. Small but fast frequency changes of a few ten MHz can be made without increase in frequency noise. Furthermore, the piezo-tunable cavities can be locked to a more stable reference with a bandwidth $> 5 \text{ kHz}$.

It has thus been shown that the piezo-tunable cavities fulfill all requirements for a tunable laser pre-stabilization for LISA. As a first step towards a space qualified piezo-tunable cavity, a novel cavity design was implemented considering the high forces that arise during the launch of a space mission. In this design the piezo actuator is prestressed between the cavity spacer components, which suppresses tensile and shear forces at the piezo actuator.

The work presented here gives a new insight into the potential of piezo-tunable cavities. Their performance is only one order of magnitude below that of the best non-tunable cavities of the same length. Furthermore, the measured noise can not be attributed to the integration of the piezo actuators, so, in principal, an even better performance should be achievable with piezo-tunable cavities. Indeed, theoretical considerations performed within this thesis reveal that the intrinsic stability of piezo-tunable cavities is only slightly inferior to that of rigid cavities.

Beyond an application in LISA, highly stable piezo-tunable cavities are also valuable devices for numerous other applications. They can be used in cavity enhanced spectroscopy, as transfer cavities or as optical local oscillators in atomic and molecular spectroscopy.

Zusammenfassung

Der geplante Gravitationswellendetektor LISA (Laser Interferometer Space Antenna) soll aus drei Satelliten bestehen, deren Abstand mit Hilfe von Laserinterferometrie überwacht wird. Die hohe Frequenzstabilität der Laser, die dafür benötigt wird, soll mit einem dreistufigen Verfahren erreicht werden. Dieses beinhaltet eine Vorstabilisierung, die nicht nur hohe Stabilität sondern auch Durchstimmbarkeit aufweisen muss. Die Kombination dieser beiden Anforderungen stellt insbesondere in Verbindung mit den speziellen Ansprüchen einer Weltraummission eine große Herausforderung für die Laser-Frequenzstabilisierung dar.

Eine Möglichkeit eine durchstimbare Vorstabilisierung zu realisieren ist die Verwendung eines optischen Resonators mit eingebautem Piezoaktuator. Dies ist an sich kein neuer Ansatz, wurde bisher allerdings noch nicht mit der geforderten Stabilität realisiert. In der Tat wurde bisher allgemein angenommen, dass Piezoaktuatoren die intrinsische Stabilität eines optischen Resonators so stark beeinflussen, dass sie nicht für Anwendungen geeignet sind die hohe Stabilität erfordern. Ziel dieser Arbeit war es diese Wissenslücke durch sorgfältige Untersuchungen von optischen Resonatoren mit eingebautem Piezoaktuator zu schließen und einen hoch-stabilen piezoelektrisch durchstimbaren Resonator zu realisieren.

Für diesen Zweck wurden vier verschiedene piezoelektrisch durchstimbare Resonatoren unter der Verwendung von kristallinem Quarz, PZT Keramik und einkristallinem PZN-PT zusammengebaut. Auf diese Resonatoren stabilisierte Laser weisen ein Frequenzrauschen kleiner als $30 \text{ Hz}/\sqrt{\text{Hz}}$ für Fourier Frequenzen oberhalb von 4 mHz und eine relative Instabilität von 7×10^{-15} bei Integrationszeiten von 0.3 s bis 8 s auf, was das bisher beste Ergebnis ist, das mit piezoelektrisch durchstimbaren Resonatoren erreicht wurde. Mit nur geringen Einbußen in der Frequenzstabilität können die Resonatoren langsam über mehr als einen freien Spektralbereich ($> 1.5 \text{ GHz}$) elektrisch durchgestimmt werden. Dieser große Durchstimbereich ermöglicht volle Flexibilität in der Wahl der Laserfrequenz. Kleine, aber schnelle Frequenzänderungen von wenigen zehn MHz können ohne Verschlechterung der Frequenzstabilität durchgeführt werden. Außerdem können die piezoelektrisch durchstimbaren Resonatoren auf eine stabilere Referenz mit einer Regelbandbreite von $> 5 \text{ kHz}$ stabilisiert werden.

Somit konnte gezeigt werden, dass die piezoelektrisch durchstimbaren Resonatoren alle Anforderungen an eine durchstimbare Vorstabilisierung für LISA erfüllen. Als erster Schritt in Richtung eines weltraumtauglichen piezoelektrisch durchstimbaren Resonators wurde ein neues Resonatordesign realisiert, das große Kräfte wie sie beim Start einer Satellitenmission auftreten berücksichtigt. In diesem Design ist der Piezoaktuator durch die Resonatorkomponenten vorgespannt, was Zug- und Scherkräfte am Piezoaktuator unterdrückt.

Die hier präsentierte Arbeit gibt einen neuen Einblick in das Potential von piezoelektrisch durchstimbaren Resonatoren. Ihre Stabilität ist nur eine Größenordnung geringer als die der besten nicht durchstimbaren Resonatoren der gleichen Länge. Dabei kann das hier gemessene Rauschen nicht den Piezoaktuatoren zugeordnet werden. Es sollte also prinzipiell möglich sein noch bessere Stabilitäten mit piezoelektrisch durchstimbaren Resonatoren zu erzielen. In der Tat zeigen theoretische Untersuchungen, die im Rahmen dieser Arbeit durchgeführt wurden, dass die intrinsische Stabilität eines Resonators durch den Einbau eines Piezoaktuators nur geringfügig herab gesetzt wird.

Hoch-stabile piezoelektrisch durchstimbare Resonatoren können über eine Verwendung in LISA hinaus auch bei zahlreichen anderen Anwendungen zum Einsatz kommen, wie z.B. in der Cavity Enhanced Spektroskopie als Transfer Resonatoren oder als optische Lokalisatoren in der Atom- und Molekülspektroskopie.

Contents

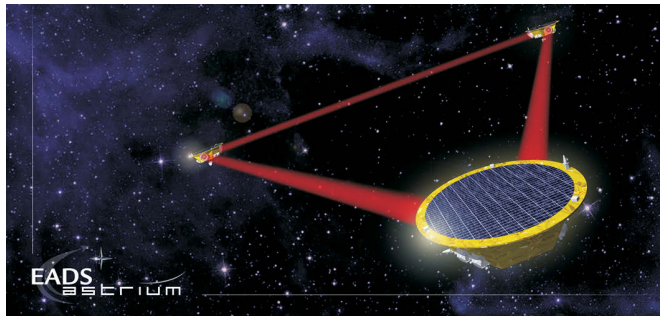
1. Introduction	1
2. A Tunable Frequency Reference for LISA	5
2.1. Gravitational waves	5
2.2. The gravitational wave detector LISA	7
2.2.1. Laser frequency stabilization for LISA	11
2.3. Tunable pre-stabilization for LISA	14
2.3.1. Requirements	14
2.3.2. Possible implementations	14
3. Theory	17
3.1. Optical resonators	17
3.1.1. Optical transfer functions	18
3.1.2. Cavity modes and mode matching	21
3.2. Laser frequency stabilization to a cavity	22
3.2.1. Feedback control loop for laser frequency stabilization	22
3.2.2. The Pound Drever Hall technique	23
3.3. Piezoelectric actuation	27
3.3.1. Fundamentals of piezoelectricity	27
3.3.2. Ferroelectricity	29
3.3.3. Piezoelectric materials	33
3.3.4. Piezoelectric actuators	35
4. Experimental Implementation	39
4.1. Cavities with incorporated piezo actuator	39
4.1.1. The piezoelectric actuators	39
4.1.2. The cavities	41
4.2. Noise sources and environmental disturbances	45
4.2.1. Effects independent of the piezo actuator	45
4.2.2. Effects influenced by the piezo actuator	50
4.2.3. Effects due to the piezo actuator - noise of piezo supply voltage	56
4.2.4. Summary	58
4.3. Test setup	59
4.3.1. Test environment	60
4.3.2. Read-out, stabilization and measurement	65

5. Characterization of the Piezo-Tunable Cavities	69
5.1. Cavity properties	69
5.2. Frequency noise with short circuited piezo actuator	72
5.2.1. Measurement and evaluation method	72
5.2.2. Results	72
5.2.3. Analysis of effects influencing the frequency stability	76
5.3. Applying a voltage	89
5.3.1. Tuning range	89
5.3.2. Voltage noise	89
5.3.3. Influence of a varying piezo driving voltage	92
5.4. Stabilization of the piezo-tunable cavity - use as transfer cavity	97
5.4.1. Implementation	97
5.4.2. Results	98
5.5. Conclusion	99
6. Cavity with Prestressed Piezo Actuator	101
6.1. Design	102
6.1.1. Calculations	103
6.1.2. Simulations	104
6.2. Assembly	106
6.3. Measurements	108
6.3.1. Cavity properties	108
6.3.2. Frequency noise	108
6.3.3. Tuning of the cavity with prestressed piezo actuator	109
6.3.4. PDH locking with modulated cavity	112
6.4. Conclusion	113
7. Summary and Outlook	115
A. Noise and Stability Estimations	117
B. Electrostatic Effect of the Quartz Cavity	119
C. Assembly of the prestressed cavity	121
Bibliography	131
List of Figures	133
List of Tables	134
List of Abbreviations	136
Acknowledgments	137

1. Introduction

The existence of gravitational waves was predicted by Albert Einstein in the context of his theory of general relativity [1] already in the year 1916. More than 50 years later Taylor and Hulse succeeded in providing an indirect proof of gravitational waves by measuring the energy loss due to gravitational radiation of the binary star system PSR B1913+16, which consists of two neutron stars including a pulsar [2]. Since the early 1960s, efforts have been made to directly measure gravitational waves, however, none of which have been successful so far. A direct measurement of gravitational waves would not only be a further proof of Einstein's theory of general relativity, but would open a new window to the exploration of our universe. All we currently know about the universe outside our own solar system was discovered by electromagnetic radiation or cosmic rays. Objects which do not radiate or emit cosmic particles and do not interact with electromagnetic radiation could thus not have been observed up to now. In these cases, gravitational waves can provide valuable new information. Furthermore, gravitational waves propagate nearly undisturbed through space and thus allow the observation of astronomical objects which are out of sight for electromagnetic waves.

Today, several detectors on Earth try to directly measure gravitational waves by using resonant mass antennas [3] or laser interferometers [4–6]. Laser interferometers use highly stable laser light to measure the proper distance between test masses. Since these masses are strongly influenced by seismic noise, it is effectively impossible to observe gravitational waves in the low frequency range with ground based detectors. So the plan of a space based gravitational wave detector emerged with the aim to complement



Artist's impression of the three LISA spacecraft. Courtesy EADS Astrium.

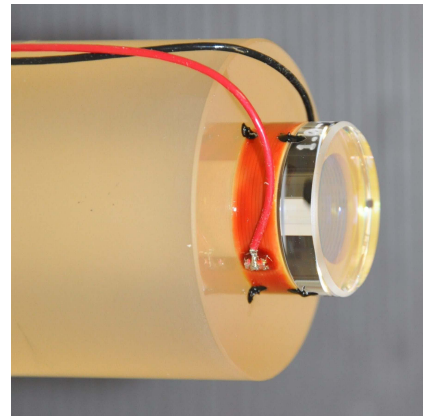
the frequency spectrum of gravitational wave observation. The proposed Laser Interferometer Space Antenna (LISA) [7, 8] consists of three spacecraft whose distance is monitored to sense spacetime strain variations. With the aid of precision laser interferometry, LISA aims for measuring gravitational waves with a strain as low as 10^{-23} . To reach such a sensitivity an extremely high stability of the employed lasers is required. The free-running laser noise has to be suppressed more than 12 orders of magnitude, which cannot be achieved in a single step. Indeed a three level noise reduction approach is proposed for LISA. This approach includes, in addition to a post processing technique, a pre-stabilization stage that has not only to provide high frequency stability but also tunability.

1. Introduction

Frequency stabilization of a laser is usually implemented by using either a resonance of an optical cavity [9] or an atomic or molecular transition [10] as a reference. In both methods only discrete laser frequencies, determined by the specific reference, can be selected. For stabilization to arbitrary frequencies within the laser tuning range, different techniques can be employed including the application of an acousto-optic modulator (AOM), serrodyne modulation [11], or an additional offset frequency locked laser [12]. These methods mostly require components with high power consumption or complex additional hardware. Therefore, further options that are better suited for the application in space have been studied, such as the use of an unequal arm-length interferometer [13, 14] or a sideband locking scheme [15]. In this thesis, another such approach is presented, namely to tune the resonance frequency of a cavity by changing the cavity length itself with a piezo actuator.

The concept to tune the cavity length with a piezo actuator is certainly not a new approach. Piezo-tunable cavities are already used as laser resonators or transfer cavities [16]. More stable versions have been realized for frequency noise characterization [17] or frequency stabilization [18]. However, both implementations do not fulfill the LISA requirements, especially not in the low frequency range. This work tries to push the frequency stabilization with piezo-tunable cavities to its limits with the aim to learn more about the potential and limitations of such a stabilization and to test its qualification for LISA.

The best cavity stabilized lasers have currently a relative frequency stability in the low 10^{-16} range [19–21], which can only be achieved by suppressing all fluctuations of the cavity length. Therefore, highly stable cavities are typically made of glass materials which have a low coefficient of thermal expansion (CTE) and feature special vibration insensitive designs [22–24]. Piezo actuators with their less favorable mechanical and thermal properties are thus expected to have a negative influence on the stability. Furthermore, the application of piezo actuators introduces frequency noise due to voltage noise in the piezo supply voltage and effects such as hysteresis and creep have to be handled. The goal of this thesis was to investigate how the stability of a cavity is influenced by the integration of a piezo-actuator by carefully evaluating the performance of a variety of such tunable systems, including ones that offer unprecedented stability. The results should not only be interesting for LISA, but for all applications where a highly stable and tunable frequency reference is required.



Piezo-tunable cavity.

Organization of the thesis

The next chapter gives a brief overview of gravitational waves and the gravitational wave detector LISA. The issue of frequency stabilization for LISA will be addressed, explaining the need for a tunable frequency reference, and possible implementations will be presented including the concept of a piezoelectrically tunable cavity.

Chapter 3 describes some theoretical foundations of Fabry-Pérot resonators, frequency stabilization and piezoelectricity, which are needed to understand how an optical resonator incorporating

a piezoelectric actuator can serve as a tunable frequency reference.

In Chapter 4 the experimental implementation of such piezo-tunable cavities and an adequate test setup will be presented including a detailed discussion of expected noise sources and sensitivities of the cavities to environmental disturbances.

Chapter 5 presents the performed measurements and obtained results including the frequency stability of the cavities, the performance with applied voltage, as well as the integration of a piezo-tunable cavity in an external feed-back loop.

Finally, in Chapter 6 a novel piezo-tunable cavity design with prestressed piezo actuators is introduced, before the thesis concludes with a short summary and outlook in Chapter 7.

2. A Tunable Frequency Reference for LISA

The demand of a tunable frequency reference for the Laser Interferometer Space Antenna (LISA) gave rise to the investigations of piezo-tunable cavities presented in this work. Therefore, after a short overview on gravitational waves, this chapter will give an introduction to the LISA mission. To understand the requirements on the tunable frequency reference, the proposed laser frequency stabilization scheme will be described including the single stages such as arm-locking and time delay interferometry (TDI). Finally, possible implementations for a tunable pre-stabilization will be presented including piezo-tunable cavities.

2.1. Gravitational waves

In his theory of general relativity [1] Einstein describes the interaction between matter, space, and time. Einstein's surprising innovation was that he considered space and time no longer as a fixed background frame as it is done in Newton's mechanics. He combined them to a four dimensional spacetime which can be deformed by matter. Gravitation manifests in this theory by the fact that matter causes spacetime to curve and a curved spacetime causes masses to accelerate.

In the theory of general relativity the curvature of spacetime is represented by the Einstein tensor $G^{\mu\nu}$ and the matter by the stress-energy tensor $T^{\mu\nu}$. The relation between matter and spacetime is formally expressed by Einstein's famous field equation

$$G^{\mu\nu} = \frac{8\pi G}{c^4} T^{\mu\nu} \quad (\mu, \nu = 0, 1, 2, 3), \quad (2.1)$$

where G is the gravitational constant and c the speed of light. The Einstein tensor is defined as

$$G^{\mu\nu} = R^{\mu\nu} - \frac{1}{2} g^{\mu\nu} R + g^{\mu\nu} \Lambda, \quad (2.2)$$

where $R^{\mu\nu}$ is the Ricci tensor, $g^{\mu\nu}$ the metric tensor, R the Ricci curvature and Λ the cosmological constant (see for example [25]).

The evolution in time of astronomical systems can be described by solving Einstein's equation. Equation (2.1) is, however, a system of at least ten coupled differential equations, which due to their complexity, can hardly be solved analytically. Therefore, Einstein's equations are often studied in the weak gravitational field approximation, which is also referred to as linearized theory of gravity.

In the absence of gravitation the spacetime is flat. With a weak gravitational field the space-

2. A Tunable Frequency Reference for LISA

time metric $g_{\mu\nu}$ deviates only slightly from a flat metric $\eta_{\mu\nu}$ [25, 26]

$$g_{\mu\nu} = \eta_{\mu\nu} + h_{\mu\nu} \quad \|h_{\mu\nu}\| \ll 1. \quad (2.3)$$

With this metric the linearized Einstein equation can be written as

$$\square \bar{h}^{\mu\nu} = (\Delta - \frac{1}{c^2} \partial_t^2) \bar{h}^{\mu\nu} = \frac{16\pi G}{c^4} T^{\mu\nu}, \quad (2.4)$$

using the trace reverse perturbation $\bar{h}^{\mu\nu} = h^{\mu\nu} - \frac{1}{2} \eta^{\mu\nu} h$, where $h = h^\mu_\mu$ is the trace of the metric perturbation, and choosing an appropriate gauge transformation which satisfies the Lorentz gauge condition $\partial_\mu \bar{h}^{\mu\nu} = 0$. Here and in the following, the Einstein summation convention applies ($x_\mu y^\mu = \sum_{\mu=0}^3 x_\mu y_\mu$). Equation (2.4) strongly resembles the wave equation in electromagnetism, and can also be solved accordingly by a superposition of plane waves. These solutions are called gravitational waves.

The propagation of gravitational waves is usually regarded in vacuum ($T^{\mu\nu} = 0$) where equation (2.4) simplifies to the homogeneous version

$$\square \bar{h}^{\mu\nu} = (\Delta - \frac{1}{c^2} \partial_t^2) \bar{h}^{\mu\nu} = 0. \quad (2.5)$$

A solution of this equation has the form

$$\bar{h}^{\mu\nu} = A^{\mu\nu} \exp(ik_\mu x^\mu), \quad (2.6)$$

where $A^{\mu\nu}$ is a complex amplitude tensor and k_μ a four dimensional wave vector. From the Lorentz gauge condition follows $A^{\mu\nu} k_\mu = 0$. The amplitude of the gravitational waves is thus orthogonal to their direction of propagation; gravitational waves are transversal.

The Lorentz gauge condition is fulfilled by a class of gauges. For a further description of gravitational waves it is useful to apply additional restrictions on the Lorentz gauge using the so called transverse-traceless gauge from this class. This gauge makes the metric perturbation $h_{\mu\nu}$ purely spatial ($h_{\mu 0} = 0$) and traceless ($h^\mu_\mu = 0$). With this restriction, a wave traveling in z-direction has the form

$$h_{\mu\nu}^{TT} = \begin{pmatrix} 0 & 0 & 0 & 0 \\ 0 & h_{xx} & h_{xy} & 0 \\ 0 & h_{xy} & -h_{xx} & 0 \\ 0 & 0 & 0 & 0 \end{pmatrix} = h_{xx} h_+ + h_{xy} h_\times. \quad (2.7)$$

The two independent components h_{xx}^{TT} and h_{xy}^{TT} are interpreted as two orthogonal polarization components of the gravitational wave, which are called + (plus) and \times (cross), respectively.

To learn how a gravitational wave effects free particles, the proper distance L' of two particles separated by a coordinate distance L is calculated. The distance ds between two points in spacetime with coordinates x^μ and $x^\mu + dx^\mu$ is given by

$$ds^2 = g_{\mu\nu} dx^\mu dx^\nu. \quad (2.8)$$

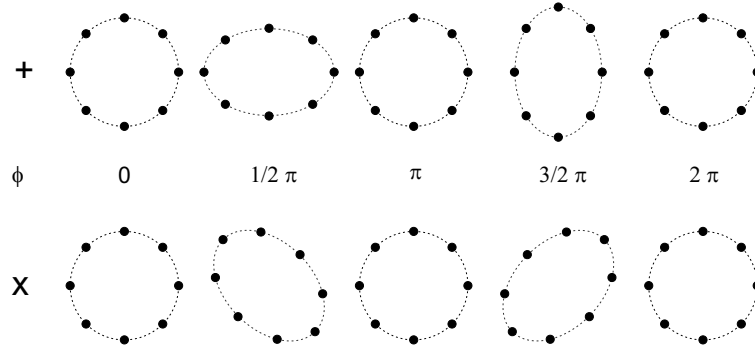


Figure 2.1.: Effect of a gravitational wave with + or \times polarization on a ring of test masses, which are arrayed in a plane perpendicular to the propagation direction of the wave, depicted for different phase ϕ of the wave.

L' can thus be calculated by [25]

$$\begin{aligned}
 L' &= \int_0^L |ds^2|^{1/2} = \int_0^L |g_{\mu\nu} dx^\mu dx^\nu|^{1/2} = \int_0^L |g_{xx}|^{1/2} dx \\
 &\approx |g_{xx}|^{1/2} L = (1 + h_{xx}^{TT})^{1/2} L \\
 &\approx [1 + \frac{1}{2} h_{xx}^{TT}] L.
 \end{aligned} \tag{2.9}$$

Two test masses separated by a distance L experience thus a strain of

$$\frac{\delta L}{L} = \frac{1}{2} h_{xx}^{TT}. \tag{2.10}$$

The influence of purely \times or $+$ polarized waves on a ring of particles is illustrated in Figure 2.1.

Laser interferometer gravitational wave detectors monitor the change in separation between two masses, so called test masses. Since the distance change is proportional to the original distance of the test masses, the laser interferometers use very large interferometer arms (> 300 m) and form in this way the most sensitive detectors to date. In addition to the already existing interferometers on Earth [4–6] a space based interferometer is planned which allows even longer distances between the test masses.

2.2. The gravitational wave detector LISA

The Laser Interferometer Space Antenna (LISA) [7, 8] is a proposed space mission which has the aim to observe gravitational waves in the low frequency range which is not accessible with ground based gravitational wave detectors. The mission was planned as a joint ESA and NASA mission. Since NASA recently withdrew funds, a down scaled mission was formulated, called New Gravitational Wave Observatory (NGO). In the following the original LISA mission will be described and the differences to NGO will only be pointed out shortly at the end of this section.

2. A Tunable Frequency Reference for LISA

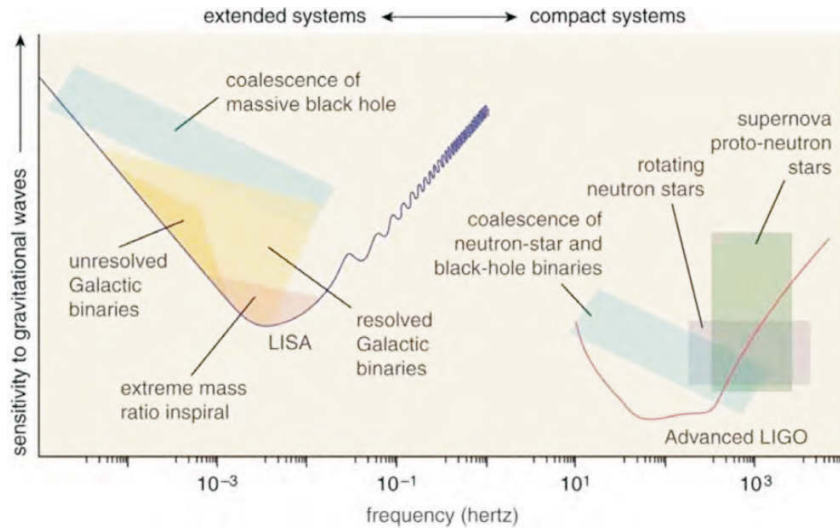


Figure 2.2.: Strain sensitivity predicted for LISA and the ground-based gravitational wave detector advanced LIGO [4], as well as relevant sources of gravitational waves in the respective frequency range. From [27], courtesy NASA.

Sources of gravitational waves in the LISA measurement band

Gravitational radiation is generated by accelerated mass and energy. The periodic motion of a system creates gravitational waves, whose strain amplitude depends on the mass, size, and distance of the system. The frequency of the motion determines the frequency of the created gravitational wave. LISA is designed to observe gravitational waves in the frequency range between 0.1 mHz and 1 Hz with a strain sensitivity down to 10^{-23} (Figure 2.2). For comparison, the ground based detectors have a measurement band between 10 Hz and 10 000 Hz and envisage a strain sensitivity down to 10^{-24} when the current upgrades are accomplished.

LISA will be able to trace the inspiral and merger history of massive black hole (MBH) binaries, which are the strongest sources in the LISA measurement band. Estimates from standard galaxy formation theory suggest that LISA will detect MBH coalescences about once or twice every weak. LISA will thus provide a direct record of the history of galaxy formation and central black hole growth in the observable Universe.

Smaller galactic objects can be captured by a massive black hole building an extreme mass-ratio inspiral (EMRI) with frequencies and strains in the measurement band. Compact objects such as degenerate dwarfs, neutron stars, and black holes which get in the vicinity of a MBH will orbit the latter until they finally plunge into the black hole's event horizon. The gravitational waves emitted during this process will provide interesting information about the spacetime geometry around the MBH.

The most frequently observed objects will be binary stars, consisting, e.g., of two white dwarfs or two neutron stars. Binary systems in our vicinity have already been observed by electromagnetic observations and their known periods and positions will appear in the LISA data with predictable, distinctive signatures.

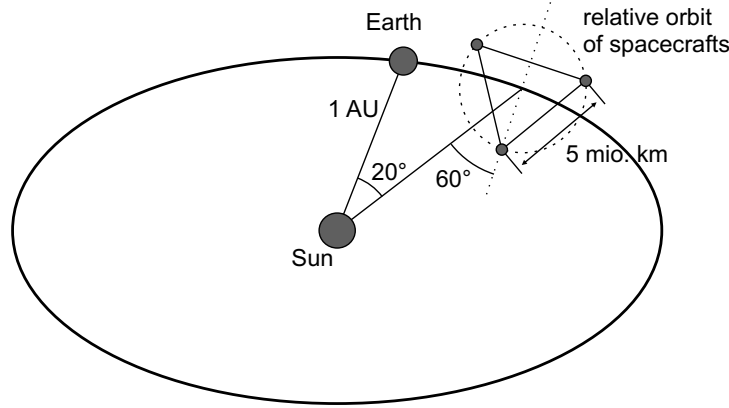


Figure 2.3.: The LISA satellite constellation. The LISA interferometer is depicted disproportionately large in comparison to the other astronomical distances.

The frequency range and strain amplitude of gravitational waves from massive black hole binaries, extreme mass-ratio inspirals and binary stars, which are the most important sources in the LISA measurement band, are indicated in Figure 2.2. In addition, LISA has scientific objectives like measuring the cosmic expansion, testing models of new physics of dark energy or detecting the gravitational radiation background generated at the Big Bang. More information on the scientific objectives of LISA can be found, e.g., in [8, 27].

Mission and payload

LISA can be thought of as a vast Michelson interferometer in space with an additional redundant third arm. The mission consists of three spacecrafts forming a triangle with an arm length of 5 million kilometers. Each spacecraft follows its own orbit around the sun so that the center of the triangle is in the ecliptic plane following the orbit of the Earth 20° behind the Earth, while the plane of the triangle has an inclination of 60° to the ecliptic (Figure 2.3).

The elliptical orbits as well as planetary perturbations will cause small changes in the distance of the spacecrafts (Figure 2.4). This implicates a changing relative velocity between the satellites which imposes Doppler shifts on the interferometer signals (Figure 2.5). These Doppler shifts are the reason for the demand of a tunable frequency stabilization as explained later.

LISA senses the effect of a passing gravitational wave by monitoring the changes in the distances between inertial test masses. Each spacecraft houses one of those test masses, which is shielded by the spacecraft from non-gravitational disturbances such as solar radiation pressure. The position of the spacecraft relative to the test mass is measured by optical and capacitive sensing and controlled via a feed back loop using micro-Newton thrusters as actuators.

Two telescopes on each spacecraft are used to send 2 W of laser power at 1064 nm to one of the other spacecrafts. There, the telescope is used to focus the weak incoming laser beam. Due to beam expansion, only about 100 pW can be collected after the distance of 5 mio. km. Instead of back reflecting the light directly, the laser on the receiving spacecraft is phase-locked to the incoming light in order to have a reflected beam with full intensity. When the transmitted laser

2. A Tunable Frequency Reference for LISA

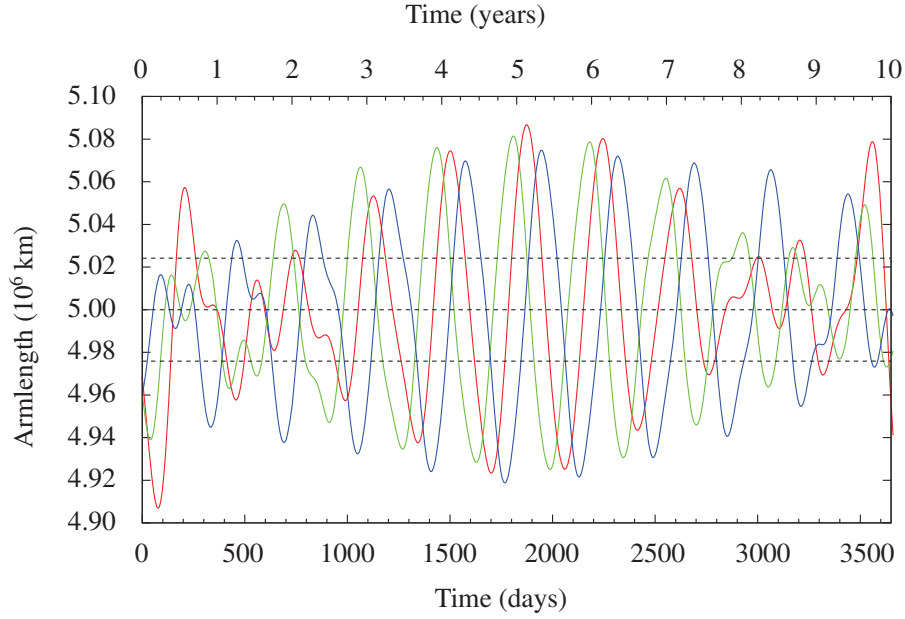


Figure 2.4.: Variation of the satellite distance in the course of the LISA mission. Each color stands for one satellite distance. Reprinted from [8] with permission.

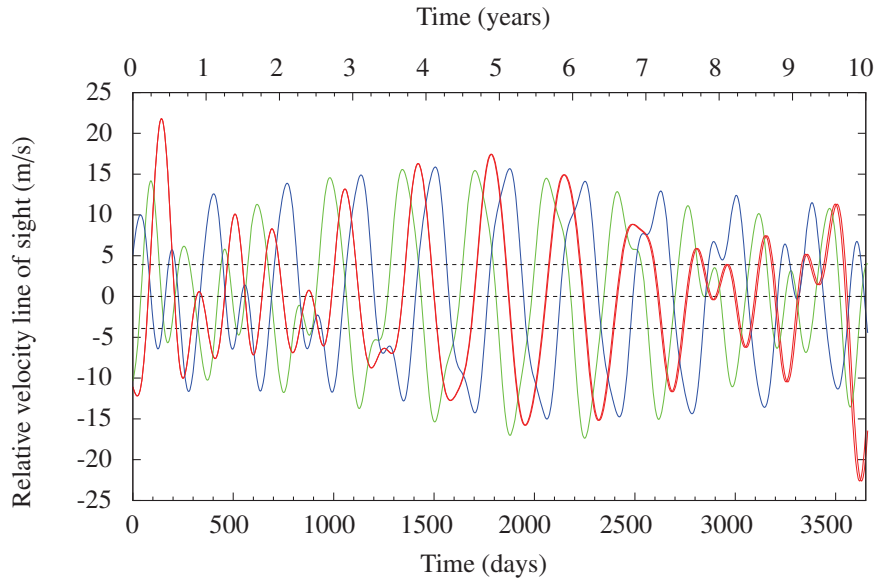


Figure 2.5.: Variation in the velocity between the satellites. This variation determines the doppler shift between received and emitted beam. For the wavelength chosen for LISA, 1 m/s corresponds to 1 MHz Doppler shift. Reprinted from [8] with permission.

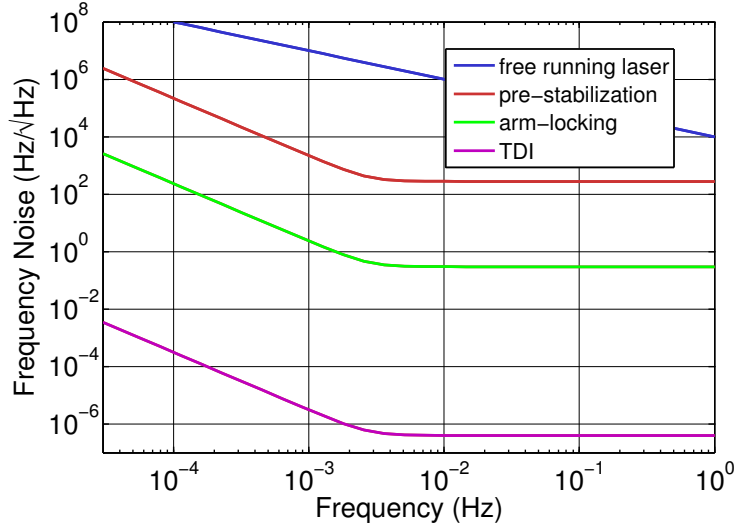


Figure 2.6.: LISA requirements on the different stages of frequency noise reduction.

light arrives back at the original spacecraft, it is superimposed with a portion of the original laser beam. A relative phase measurement gives information about the length of the interferometer arm. By comparing the relative length changes in two interferometer arms, the gravitational wave signal can be observed.

The NGO mission differs from the LISA mission mainly in the absence of a third redundant interferometer arm and a shorter arm length of 1 million kilometers which leads to a reduction of the sensitivity in the lower end of the measurement band.

2.2.1. Laser frequency stabilization for LISA

Laser frequency stabilization is an important point in the LISA technology development. Frequency fluctuations $\delta\nu$ cause noise in the interferometric length measurement δx , that is proportional to the arm length difference ΔL :

$$\delta x = \Delta L \frac{\delta\nu}{\nu}. \quad (2.11)$$

The length changes of a single arm are expected to be up to 2 % (Figure 2.4), which leads to length differences between two arms of up to $\Delta L = 1 \times 10^5$ km. The equivalent pathlength noise contribution due to frequency noise has to be below $\delta x = 0.4 \text{ pm}/\sqrt{\text{Hz}}$. Consequently, a laser frequency noise below $1.2 \times 10^{-6} \text{ Hz}/\sqrt{\text{Hz}}$ is required, which equals a relative stability of 4.3×10^{-21} . For comparison, the best actively stabilized lasers nowadays have a relative stability of 1×10^{-16} at integration times of 1 s. This shows already that the desired sensitivity can only be achieved applying an adequate post processing technique. The frequency noise of a free-running laser has to be suppressed by about 12 orders of magnitude which cannot be achieved in a single step. Therefore, a three level approach is the current baseline for frequency noise reduction for LISA. The first stage includes a tunable pre-stabilization technique. In the second

2. A Tunable Frequency Reference for LISA

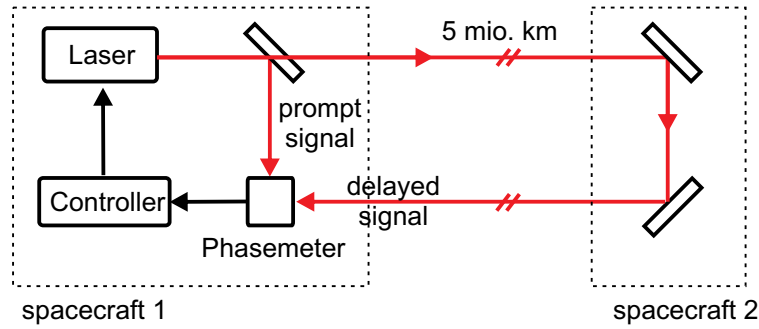


Figure 2.7.: Self phase locking scheme. The beam coming back from the distant spacecraft has a time delay of $\tau = 33$ s in comparison to the prompt signal. In this way the present laser phase can be compared with the past laser phase and a signal for stabilization can be derived.

stage the long LISA arms itself are used as a frequency reference in a technique called arm-locking. The third step is a post processing technique called time delay interferometry (TDI) in which the arm length difference is formally canceled out. The three stabilization stages will be described in more detail in the following. An overview of the frequency noise requirements on the different stabilization stages is given in Figure 2.6.

All in all, the three LISA satellites house six lasers. Only one laser is stabilized according to the above described scheme. The other lasers will be offset phase locked to this master laser.

Pre-stabilization

The first stage of the LISA noise reduction scheme comprises pre-stabilization to a local reference. Such a reference could be an optical cavity, a molecular resonance or an unequal pathlength interferometer. The special challenge is, that the frequency reference not only has to provide high stability but also tunability. This demand arises from the combination with the arm-locking technique, described in the following. Detailed requirements on such a tunable reference and possible implementations are described in the next section.

Arm-locking

In the LISA measurement band the 5 mio. km long LISA arms will have a relative length stability of approximately $\delta L/L \sim 10^{-21}/\sqrt{\text{Hz}}$. (The slow arm length variations shown in Figure 2.4 are below the LISA measurement band.) Arm-locking uses this highly stable interferometer arms as frequency reference and derives an error signal by self-phase-locked delay interferometry. In this technique, a fraction of the laser light from one spacecraft interferes with the light which is transmitted back from another spacecraft. Since the back-transmitted light is phase locked to the original laser light, the configuration forms a Mach-Zehnder interferometer with a large time delay in one arm (Figure 2.7). With a suitable control law, noise at frequencies below the round-trip frequency $f_0 = 1/\tau = 30$ mHz can be reduced, leading however to an unwanted amplification of noise at integer multiples of f_0 [28]. This drawback could already be solved using the phase difference of two interferometer arms in sum and difference [29].

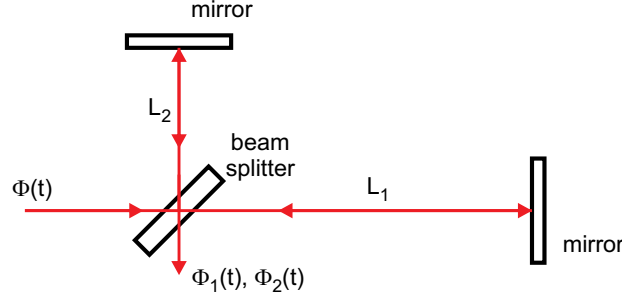


Figure 2.8.: Scheme of an unequal arm length interferometer.

When applying arm-locking, one has to consider the relative motion of the spacecrafts up to 18 m/s which leads to Doppler shifts up to 18 MHz (Figure 2.5). During the LISA mission the Doppler shifts will be estimated and removed from the phase signal. However, small errors in the Doppler frequency estimation ν_{DE} cannot be avoided and lead to a continuous change of the closed loop laser frequency $\delta\nu_{cl}$ with a rate of [30]

$$\frac{\delta\nu_{cl}}{\delta t} = \nu_{DE} \frac{c}{2L}. \quad (2.12)$$

This frequency pulling can be minimized using advanced arm-locking schemes (modified dual arm-locking) and adequate control electronics. With these techniques the frequency pulling can be kept below 8 MHz [30]. When arm-locking is combined with some kind of pre-stabilization, the pre-stabilization has to be able to follow those frequency changes. With other words, it has to feature tunability.

Time delay interferometry (TDI)

The last step in the frequency reduction scheme, is not an active frequency stabilization technique, but a post processing technique. The continuously recorded phase informations of the outgoing and ingoing light from one or more spacecrafts are used to computationally suppress the laser phase noise.

If $\Phi(t)$ is the phase noise of a laser which enters a simple interferometer (Figure 2.8), the phase at the beam splitter after passing way L_1 or L_2 is

$$\Phi_1(t) = \Phi\left(t - 2\frac{L_1}{c}\right) - \Phi(t) \quad (2.13)$$

and

$$\Phi_2(t) = \Phi\left(t - 2\frac{L_2}{c}\right) - \Phi(t). \quad (2.14)$$

For the case of an unequal arm length interferometer ($L_1 \neq L_2$) the difference $\Phi_2 - \Phi_1$ is obviously not zero.

2. A Tunable Frequency Reference for LISA

The basic idea of TDI is to additionally delay the phases by a specific value and combine them in such a way that the laser phase noise cancels out [31]

$$X(t) = [\Phi_2(t - 2\frac{L1}{c}) - \Phi_2(t)] - [\Phi_1(t - 2\frac{L2}{c}) - \Phi_1(t)] = 0. \quad (2.15)$$

For LISA this scheme gets way more complex, due to the existence of three spacecrafts and changing interferometer arm lengths. Nevertheless, the problem can still be solved using the same principle [31, 32].

2.3. Tunable pre-stabilization for LISA

The combined requirements of high stability and tunability are a challenging task for laser frequency stabilization. After shortly specifying the exact requirements, this section will give an overview how such a tunable reference could be realized and which work has already been done on this topic.

2.3.1. Requirements

In the LISA pre-Phase A report [7] first frequency stability requirements for a tunable pre-stabilization were allocated to

$$S_\nu = 30 \text{ Hz}/\sqrt{\text{Hz}} \cdot \sqrt{1 + (3 \text{ mHz}/f)^4}. \quad (2.16)$$

Later, TDI and arm-locking turned out to be more powerful than initially expected and the requirements were relaxed to [33]

$$S_\nu = \begin{cases} 282 \text{ Hz}/\sqrt{\text{Hz}} \cdot \sqrt{1 + (2.8 \text{ mHz}/f)^4} & \text{for } 0.1 \text{ mHz} < f < 1 \text{ Hz} \\ 3000 \text{ Hz}/\sqrt{\text{Hz}} \cdot 1 \text{ Hz}/f & \text{for } 1 \text{ Hz} < f < 1 \text{ MHz}. \end{cases} \quad (2.17)$$

The tuning requirements of $\pm 30 \text{ MHz}$ [33] arise from the expected frequency pulling in the arm-locking feed back loop due to errors in the Doppler shift estimation. The required tuning bandwidth of 1 kHz [33] ensures that the tunability has a sufficient frequency response to support a high gain auxiliary locking scheme such as arm-locking. When using a cavity as reference, a tunability over more than one free spectral range (FSR) would be desirable. In this case the cavity can be tuned to every laser frequency, which provides the greatest flexibility.

2.3.2. Possible implementations

There are several ways to realize a tunable frequency reference. A common method is to stabilize the laser to a fixed frequency reference such as a cavity or a molecular reference and shift the frequency of the stabilized laser with an AOM. Due to the Doppler effect the diffracted beam is shifted in frequency by the magnitude of the sound wave frequency, which is adjustable. The tuning range is limited to a few ten MHz. AOMs are usually avoided in space missions, due to the large RF power consumption and the low operating power efficiency.

Another possibility is to use an additional laser and perform an offset phase lock with the stabilized laser. The beat frequency of the two lasers is compared with a stable RF oscillator. By changing the oscillator frequency the frequency of the phase locked laser can be tuned. This well known technique allows for a high tuning range but requires an additional laser. Since this additional laser would add to cost and power consumption, the phase lock approach is considered unfavorable for a space mission.

Since these standard laboratory techniques have the stated drawbacks, further techniques, which agree better with the conditions of a space mission have been developed and tested.

Sideband locking

Sideband locking uses a fixed frequency reference and a modified Pound Drever Hall (PDH) locking scheme. The easiest realization of sideband locking is that not the carrier, but the sideband is stabilized to the reference line (single sideband locking). Thus, when changing the modulation frequency the sideband stays locked to the reference line and the carrier frequency is shifted relative to the reference frequency. If the sideband is additionally modulated (dual sideband locking), the second modulation frequency can be used for demodulation of the signal. This brings the advantage of an unchanging demodulation frequency, which is not the case for the single sideband approach.

Sideband locking to a cavity was demonstrated and analyzed at NASA's Goddard Space Flight Center [15, 34]. They obtained a frequency noise of $100 \text{ Hz}/\sqrt{\text{Hz}}$ for Fourier frequencies above 1 mHz, which fulfills the LISA requirements for a tunable pre-stabilization. Sideband locking is thus suitable for LISA. The disadvantages of this method are a complex modulation spectrum of the laser carrying the risk, that the carrier or higher order sidebands couple into higher order modes of the cavity. Furthermore, in order to obtain a large tuning range, a frequency synthesizer which provides GHz frequencies is required.

Unequal pathlength interferometer

In an interferometer with equally long interferometer arms frequency fluctuations cancel out. This is not the case when the arms have different pathlengths. The interferometer gets sensitive to frequency fluctuations and can thus be used for sensing frequency changes and for frequency stabilization. The advantage of such an interferometer is that it can be operated at any laser frequency. The frequency discrimination signal, necessary for locking, is available at every laser frequency and not only at certain reference lines. Tuning of the laser frequency can thus be done by merely adding an electronic offset to the error signal.

Unequal pathlength interferometers have been realized in fiber coupled versions allowing for a large length mismatch. With fiber interferometers, good frequency stabilities at high frequencies have been achieved ($100 \text{ mHz}/\sqrt{\text{Hz}}$ at a Fourier frequency of 1 kHz [13]) and tunability has already been demonstrated [35]. However, fibers are very sensitive to temperature variations changing the optical path length. Thus, in the low frequency range a free beam version is preferable. Such a free beam version was set up for LISA Pathfinder [36] and is suggested to be used in LISA for pre-stabilization [14]. The performance with 50 cm pathlength difference is estimated to $800 \text{ Hz}/\sqrt{\text{Hz}}$ from 10 mHz to 1 Hz.

2. A Tunable Frequency Reference for LISA

Piezoelectrically tunable resonator

Tuning of a cavity stabilized laser can easily be achieved by changing the cavity length. The resonance frequencies of a cavity are given by

$$\nu_q = q \frac{c}{2L}, \quad (2.18)$$

where L is the cavity length, c the speed of light and q an integer. A cavity laser lock is usually performed by using one of those resonance lines as frequency reference. Changing the cavity length, tunes the resonance frequency and thus the laser frequency. The cavity length can be changed slowly by temperature: $\delta\nu/\nu = \alpha T$, where α is the coefficient of thermal expansion (CTE) of the cavity spacer material. With a piezoelectric actuator, the cavity length can be manipulated in a fast and defined way.

Piezo-tunable cavities are already commonly used for laser resonators or as transfer cavities [16]. A piezo-tunable cavity where the cavity spacer is compressed with an extrinsic actuator [17] has been implemented with stabilities in the 10^{-13} range, allowing however only a few 10 kHz tuning range. Furthermore, it has been demonstrated that a laser system including stabilization to a cavity with an intrinsic piezo actuator can be realized with a few kHz linewidth [18]. However, the real potential and limitations of tunable high finesse cavities have so far not been thoroughly investigated.

The aim of the work presented in this thesis was to test, if the requirements for a tunable pre-stabilization can be fulfilled with a piezoelectrically tunable resonator and to investigate the characteristics and limitations of such a stabilization. The experimental investigations are intended to give a proof of principle in a laboratory environment and do at first not deal with special conditions in space.

3. Theory

In order to understand how an optical resonator incorporating a piezoelectric actuator can serve as a tunable frequency reference, some basic understanding of optical cavities, piezoelectricity, and laser stabilization is needed. This will be provided in this chapter.

3.1. Optical resonators

With an appropriate locking scheme, the length stability of an optical resonator can be transferred to the frequency stability of a laser. This is possible because optical cavities have a strongly frequency dependent reflection and transmission as will be derived in the following.

The simplest configuration of an optical cavity is a Fabry-Pérot resonator, which consists of two parallel mirrors (Figure 3.1). The two mirrors are characterized by their dimensionless reflection coefficients r_1 and r_2 , their transmission coefficients t_1 and t_2 and their loss coefficients l_1 and l_2 . These coefficients describe the behavior of the amplitude of the electromagnetic wave, impinging on the mirrors. When regarding the intensity of a light field instead of the amplitude, the intensity coefficients of reflection, transmission, and losses have to be used. They are the square of the amplitude coefficients, e.g. $R_1 = r_1^2$, and fulfill the energy conservation relation $R + T + L = 1$.

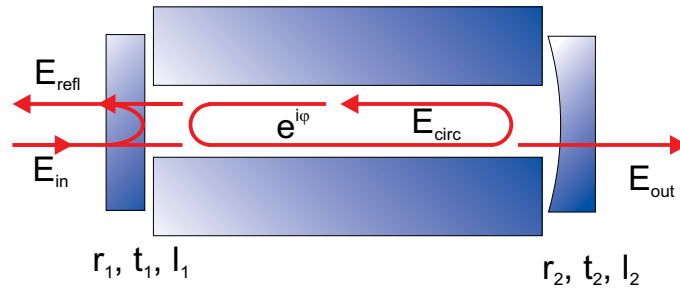


Figure 3.1.: Schematic of a Fabry-Pérot cavity. The two mirrors have (amplitude) reflection coefficients $r_{1,2}$, transmission coefficients $t_{1,2}$ and loss coefficients $l_{1,2}$. The incoming laser light E_{in} is either reflected or transmitted. The transmitted light circulates in the cavity (E_{circ}) until it is transmitted through the outcoupling mirror (E_{out}) or through the incoupling mirror where it adds to the directly reflected light (E_{refl}). During one round trip in the cavity the light accumulates the phase φ .

3. Theory

3.1.1. Optical transfer functions

The transmission through a Fabry-Pérot cavity or the reflection at the cavity are described by the cavity transfer functions, which will be derived in the following summarizing from literature [37–39]. These transfer functions help to gain a better understanding of cavity characteristics and are needed for the description of the laser stabilization theory in the next section. The transfer functions of the amplitude and intensity of the electric field are first derived with the assumption of no intra cavity losses. The modification of the formulas in presence of intra cavity losses will be presented and the special case of high finesse cavities will be discussed.

Transfer functions of the electric field

A light wave of frequency ω and amplitude E_{in} impinging on the incoupling mirror of a cavity is partly reflected, partly transmitted and partly absorbed or scattered according to the respective coefficients. The transmitted light combines with the light field E_{circ} already circulating in the cavity. In steady state ($\dot{E}_{\text{circ}} = 0$), the electric field inside the cavity is a superposition of light coming through the incoupling mirror and the light which has made one round trip in the cavity

$$E_{\text{circ}} = t_1 E_{\text{in}} + r_1 r_2 e^{i\varphi} E_{\text{circ}} = \frac{t_1}{1 - r_1 r_2 e^{i\varphi}} E_{\text{in}}. \quad (3.1)$$

φ is the phase which is accumulated during one round trip of the circulating light

$$\varphi(\omega) = \frac{\omega}{\Delta_{\text{FSR}}}, \quad (3.2)$$

where Δ_{FSR} is the free spectral range (FSR) of the resonator, which is defined as the inverse of the round trip time

$$\Delta_{\text{FSR}} = \frac{1}{\tau_{\text{rt}}} = \frac{c}{2L}. \quad (3.3)$$

With equation (3.1) the electric field in transmission of the cavity can be calculated by

$$E_{\text{trans}} = t_2 e^{i\varphi/2} E_{\text{circ}} = \frac{t_1 t_2 e^{i\varphi/2}}{1 - r_1 r_2 e^{i\varphi}} E_{\text{in}}. \quad (3.4)$$

The factor $e^{i\varphi/2}$ accounts for the half round trip, which the light travels on its way to the outcoupling mirror.

The light in reflection is a superposition of the directly reflected light and the light leaking out from the cavity through the incoupling mirror

$$E_{\text{refl}} = r_1 E_{\text{in}} - t_1 r_2 e^{i\varphi} E_{\text{circ}} = \frac{r_1 - r_2 (r_1^2 + t_1^2) e^{i\varphi}}{1 - r_1 r_2 e^{i\varphi}} E_{\text{in}}, \quad (3.5)$$

where the minus sign accounts for the phase jump, which occurs when the light is reflected on the outcoupling mirror.

3.1. Optical resonators

For some calculations the approximation of a lossless cavity ($t^2 + r^2 = 1$) with identical mirrors ($r_1 = r_2 = r$) is useful. With these restrictions the reflection coefficient r_C becomes

$$r_C(\omega) = \frac{E_{\text{refl}}}{E_{\text{in}}} = r \frac{1 - e^{i\varphi}}{1 - r^2 e^{i\varphi}} = r \frac{1 - e^{i\omega/\Delta_{\text{FSR}}}}{1 - r^2 e^{i\omega/\Delta_{\text{FSR}}}}, \quad (3.6)$$

and the transmission coefficient

$$t_C(\omega) = \frac{E_{\text{refl}}}{E_{\text{in}}} = \frac{t^2 e^{i\varphi/2}}{1 - r^2 e^{i\varphi}} = \frac{t^2 e^{i\omega/2\Delta_{\text{FSR}}}}{1 - r^2 e^{i\omega/\Delta_{\text{FSR}}}}. \quad (3.7)$$

Intensity transfer functions

Since usually the intensity of a light field is observed in a measurement, the corresponding transfer functions will be introduced. The intensity of the transmitted field is proportional to the absolute square of the electric field ($E_{\text{trans}} E_{\text{trans}}^*$):

$$I_{\text{trans}} = I_{\text{in}} \frac{T_1 T_2}{|1 - \sqrt{R_1 R_2} e^{i\varphi}|^2} = I_{\text{in}} \frac{T_1 T_2}{(1 - \sqrt{R_1 R_2})^2} \frac{1}{1 + (\frac{2\mathcal{F}}{\pi})^2 \sin^2(\varphi/2)}, \quad (3.8)$$

where

$$\mathcal{F} = \frac{\pi \sqrt[4]{R_1 R_2}}{1 - \sqrt{R_1 R_2}} \quad (3.9)$$

is the cavity finesse. The finesse is defined as the ratio of the FSR and the linewidth Γ_ν (full width at half maximum (FWHM)) of the cavity resonance

$$\mathcal{F} = \frac{\Delta_{\text{FSR}}}{\Gamma_\nu}. \quad (3.10)$$

The linewidth of a cavity is thus determined by the cavity length and its mirror reflectivities.

The second factor of equation (3.8)

$$A(\varphi) = \frac{1}{1 + (\frac{2\mathcal{F}}{\pi})^2 \sin^2(\varphi/2)} \quad (3.11)$$

is called Airy function. The function has maxima at multiples of $\Delta\varphi = 2\pi$ or $\Delta\nu = \Delta_{\text{FSR}}$ (Figure 3.2). The width of the maxima depends on the cavity finesse. The higher the finesse, the sharper the maxima. In case of a high finesse, the cavity acts as a mirror for all laser frequencies except for multiples of the FSR where the cavity gets totally transparent.

Using the Airy function, the transmission T_C of a cavity can be expressed by

$$T_C = \frac{I_{\text{trans}}}{I_{\text{in}}} = \frac{T_1 T_2}{(1 - \sqrt{R_1 R_2})^2} A(\varphi). \quad (3.12)$$

3. Theory

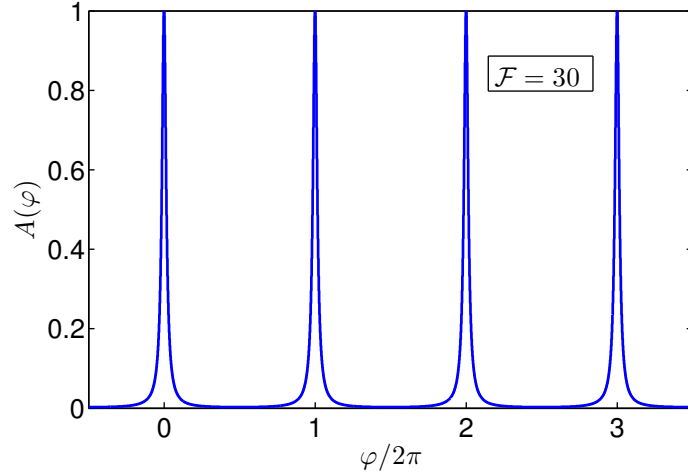


Figure 3.2.: Plot of the Airy function with a Finesses of $\mathcal{F} = 30$. The Airy function has sharp transmission peaks at integer multiples of $\varphi/2\pi = \nu/\Delta_{\text{FSR}}$.

Accordingly, the cavity reflectivity R_C is

$$R_C = \frac{I_{\text{refl}}}{I_{\text{in}}} = (R_1 + T_1) - \left((R_1 + T_1) - \frac{[\sqrt{R_1} - (R_1 + T_1)\sqrt{R_2}]^2}{(1 - \sqrt{R_1 R_2})^2} \right) A(\varphi). \quad (3.13)$$

Cavity with round trip losses

For a real cavity not only the mirror losses have to be considered, but also the losses inside the cavity, the so called round trip losses V . With these additional losses equation (3.9) changes to

$$\mathcal{F} = \frac{\pi \sqrt[4]{R_1 R_2 (1 - V)}}{1 - \sqrt{R_1 R_2 (1 - V)}}. \quad (3.14)$$

State of the art cavity experiments use high reflectivity mirrors ($R_i > 99.997\%$) leading to a finesse above 100 000. For such high finesse mirrors, the expression for the finesse simplifies to

$$\mathcal{F} \approx \frac{\pi}{1 - \sqrt{R_1 R_2 (1 - V)}} \approx \frac{\pi}{1 - \sqrt{1 - T_1 - T_2 - L_1 - L_2 - V}} \approx \frac{2\pi}{T_1 + T_2 + L_1 + L_2 + V}, \quad (3.15)$$

using the identity $R_i + T_i + L_i = 1$ and neglecting the terms $\mathcal{O}(T^2, L^2)$ as well as any mixing products of T, L , and V . In the same way, the cavity reflectivity in resonance ($A(\varphi) = 1$) can be estimated to

$$R_C = \frac{I_{\text{refl}}}{I_{\text{in}}} = \left(\frac{\mathcal{F}}{2\pi}\right)^2 (T_2 + L_1 + L_2 + V - T_1)^2 = \left(\frac{\mathcal{F}}{2\pi}\right)^2 \left(\frac{2\pi}{\mathcal{F}} - 2T_1\right)^2 = \left(1 - T_1 \frac{\mathcal{F}}{\pi}\right)^2. \quad (3.16)$$

An important issue in cavity experiments is the percentage of light that can be coupled into the resonator. When all light is coupled into the cavity, the cavity is called impedance matched.

This is the case when the cavity reflectivity (3.16) is zero, i.e., when the transmission of the incoupling mirror equals all losses of the cavity: $T_1 = T_2 + L_1 + L_2 + V$.

3.1.2. Cavity modes and mode matching

Light emitted from a laser has a non uniform intensity distribution. The beam profile can be derived from the wave equation for the electric field using the paraxial approximation. One solution is the well known Gaussian amplitude distribution representing the fundamental mode. But there exist also higher order modes, the so called Hermite-Gaussian modes or transverse electromagnetic (TEM) modes.

In a cavity with curved mirrors the different modes have different resonance conditions, since the eigenfrequencies not only depend on the length L of the cavity but also on the mirror curvatures $C_{1,2}$ [40]:

$$\nu_{q,m,n} = \frac{c}{2L} \left[q + \frac{m+n+1}{\pi} \arccos \sqrt{(1-L/C_1)(1-L/C_2)} \right]. \quad (3.17)$$

q is the longitudinal mode index and m and n are the TEM mode numbers.

Adjacent cavity modes with the same TEM mode number are separated by the free spectral range. For the TEM₀₀ modes the equation simplifies to

$$\nu_q = q \frac{c}{2L} = q \Delta_{\text{FSR}}. \quad (3.18)$$

The TEM₀₀ modes have a Gaussian intensity profile. Thus, a Gaussian laser beam can be matched best to these modes. To get a high percentage of the laser light coupled into the cavity, the laser beam has to be formed to match the cavity mode as exactly as possible. This process is referred to as mode matching. The fraction of light which couples into the cavity thus depends on mode matching and impedance matching.

3. Theory

3.2. Laser frequency stabilization to a cavity

The frequency of a laser can be stabilized to a resonance frequency of a cavity using feed back techniques. Therefore, a short, general description of feedback control loops is given in the following and a commonly used stabilization technique for performing a cavity lock, namely the Pound Drever Hall technique, is presented. With this technique the length stability of a cavity can be transferred to the frequency stability of a laser and a low noise laser can be realized. In this work, however, the stability transfer is used to obtain information on the piezo-tunable cavities by comparing the stabilized laser to an even more stable laser.

3.2.1. Feedback control loop for laser frequency stabilization

In a feedback loop the value of a physical quantity is compared with a reference and the difference is fed back to change or actuate the value. The schematic of a feedback loop for laser frequency stabilization is shown in Figure 3.3. The laser frequency is compared with the resonance frequency of a cavity. The cavity in combination with the detection system converts a frequency change into a voltage change and is thus referred to as discriminator. The voltage signal is processed in a servo controller and fed to an actuator which changes the laser frequency according to the voltage error signal. Discriminator, servo, and actuator are described by their transfer functions D , G , and K .

The free running laser noise S_L is suppressed by the control loop to a closed loop laser noise $S_{L,cl}$ of [41]

$$S_{L,cl}^2 = \frac{S_L^2 + |KS_G|^2 + |KGS_D|^2}{|1 + KGD|^2}. \quad (3.19)$$

S_G and S_D are additional noise added by the servo or discriminator, respectively. In the case of high gain G of the servo, this formula can be simplified such that the minimum closed loop

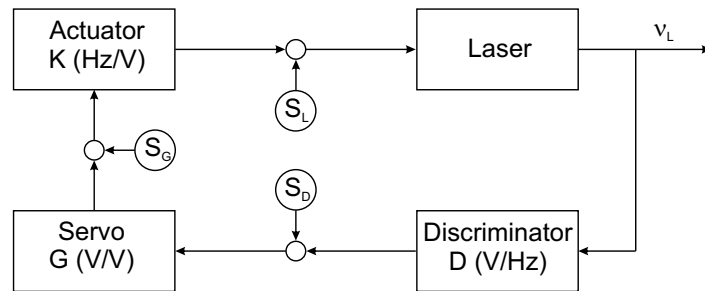


Figure 3.3.: Feedback control loop. Adapted from [41]. The control loop consists of laser with frequency ν_L , discriminator (cavity plus detection system), servo, and actuator, whose transfer functions are described by D , G , and K . In addition to the laser and actuator noise S_L , discriminator and servo contribute excess noise that is described by S_D and S_G , respectively.

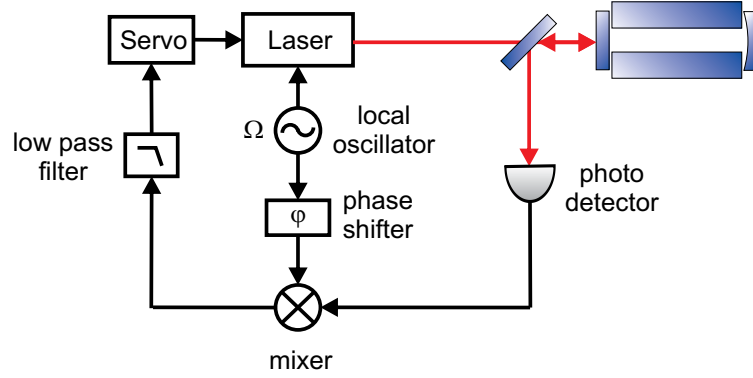


Figure 3.4.: Laser frequency stabilization with the Pound Drever Hall technique. The modulated laser light reflected from the cavity is measured with a photo detector. The obtained signal is demodulated, low pass filtered and directed to a servo controlling the laser frequency.

laser noise depends only on the discriminator transfer function and noise:

$$S_{L,cl} = \frac{S_D}{D}. \quad (3.20)$$

The discriminator noise includes, e.g., fluctuations in the resonant frequency of the cavity, residual AM noise, and quantum noise associated with the measurement of the laser frequency. The possible noise sources will be discussed in detail in the next chapter. The discriminator transfer function for the PDH stabilization scheme is derived in the following.

3.2.2. The Pound Drever Hall technique

The Pound Drever Hall (PDH) technique is a widely used method to transfer the length stability of an optical cavity to a laser frequency by actively stabilizing the laser to a cavity resonance. Based on microwave technology [42] the method was developed and elaborated for optical applications by Drever and Hall [9]. As shown in Section 3.1.1, cavities have a frequency dependent transmission such that the phase of the light reflected from a cavity shows dispersion. In the PDH technique this dispersion is detected by using a modulation technique. In the following only the steady-state case will be considered. A derivation of the dynamic response of a cavity and the effect of the time response of the resulting cavity field on the PDH error signal can be found in [43].

Phenomenological description

The basic setup for laser stabilization to a cavity with the PDH technique is shown in Figure 3.4. The laser is phase modulated with a frequency Ω , which is much larger than the cavity linewidth Γ_ν . When the laser frequency is near a resonance of the cavity the modulation sidebands are reflected unmodified, while the carrier experience a phase shift. The superposition of the directly reflected field and the field leaking back from the cavity is measured by a photo detector. Due

3. Theory

to the phase shift of the carrier, the mixing products of carrier and upper sideband and carrier and lower sideband no longer perfectly cancel out, as it is the case for purely phase modulated light. As a consequence, the measured beat signal contains an amplitude modulated term at the modulation frequency. To extract the DC component of this term the signal is demodulated with a mixer at the modulation frequency Ω and subsequently low pass filtered. The result is an error signal which is proportional to the difference between laser frequency and cavity resonance frequency. It can thus be used for building a feed back loop which matches the laser frequency to the cavity resonance frequency.

Mathematical description

In the following, a mathematical derivation of the PDH error signal will be given summarizing from literature [38, 39, 44]. The electric field of a laser beam is given by $E_0 e^{i\omega t}$. If the laser is phase modulated with Ω the electric field becomes

$$E(t) = E_0 e^{i(\omega t + \beta \sin \Omega t)} \quad (3.21)$$

$$= E_0 \sum_{k=-\infty}^{\infty} J_k(\beta) e^{i(\omega + k\Omega)t}, \quad (3.22)$$

where $J_k(\beta)$ are Bessel functions of order k with a modulation depth β , which fulfill the relation $J_{-k}(\beta) = (-1)^k J_k(\beta)$.

The modulated laser beam couples into the cavity and is modified by its transfer function $H(\omega)$

$$E_H(t) = E_0 \sum_{k=-\infty}^{\infty} J_k(\beta) H(\omega + k\Omega) e^{i(\omega + k\Omega)t}. \quad (3.23)$$

This light field is detected by a photo diode, whose signal is proportional to the intensity $I_H \sim |E_H|^2$ of the reflected or transmitted light

$$I_H(t) = I_0 \sum_{k,k'=-\infty}^{\infty} J_k(\beta) J_{k'}(\beta) H(\omega + k\Omega) H^*(\omega + k'\Omega) e^{i(k'-k)\Omega t}, \quad (3.24)$$

with $I_0 = c\epsilon_0 |E_0|^2$, where c is the speed of light and ϵ_0 the vacuum permittivity.

The signal that is of interest for a PDH lock is carried at the modulation frequency Ω . Thus, considering only the contributions with $k - k' = \pm 1$, the intensity signal simplifies to

$$I_\Omega(t) = I_0 \sum_{k=-\infty}^{\infty} [J_k(\beta) J_{k+1}(\beta) H(\omega + k\Omega) H^*(\omega + (k+1)\Omega) e^{i\Omega t} + J_k(\beta) J_{k-1}(\beta) H(\omega + k\Omega) H^*(\omega + (k-1)\Omega) e^{-i\Omega t}]. \quad (3.25)$$

To further simplify this equation only the first order sidebands of the modulation are taken into

3.2. Laser frequency stabilization to a cavity

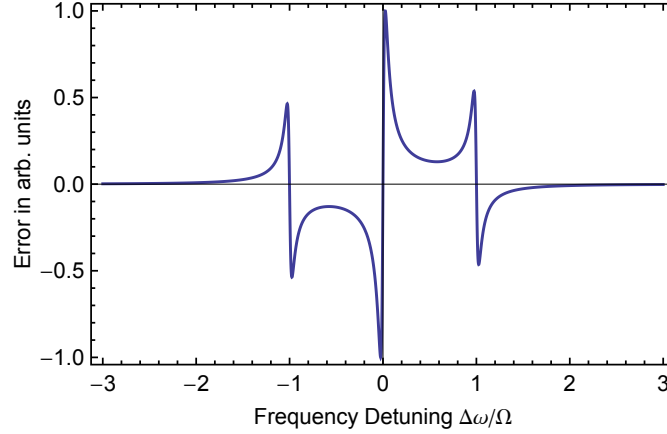


Figure 3.5.: Error signal of the Pound Drever Hall technique. The graph is calculated with a modulation frequency of 1 MHz, a cavity linewidth of 50 kHz and a finesse of 30 000.

account

$$I(t) \approx I_0 J_0(\beta) J_1(\beta) \left\{ [H(\omega)H^*(\omega + \Omega) - H^*(\omega)H(\omega - \Omega)]e^{i\Omega t} + [H^*(\omega)H(\omega + \Omega) - H(\omega)H^*(\omega - \Omega)]e^{-i\Omega t} \right\}. \quad (3.26)$$

This is equivalent to

$$I(t) = 2I_0 J_0(\beta) J_1(\beta) \left\{ \Re[H(\omega)H^*(\omega + \Omega) - H^*(\omega)H(\omega - \Omega)] \cos \Omega t - \Im[H(\omega)H^*(\omega + \Omega) - H^*(\omega)H(\omega - \Omega)] \sin \Omega t \right\}, \quad (3.27)$$

using the identity $Ae^{-i\omega t} + A^*e^{i\omega t} = 2\Re(A) \cos \omega t + 2\Im(A) \sin \omega t$.

The PDH error signal ϵ is obtained by mixing the measured intensity with $\sin(\Omega t + \phi_\Omega)$. By adjusting the phase of the demodulation signal either the cosine or the sine term can be extracted. For fast frequency modulation ($\Omega \gg \Gamma_\nu$, where Γ_ν is the cavity linewidth) the sidebands are totally reflected ($H(\omega \pm \Omega) = -1$) when the carrier is near resonance. The term

$$H(\omega)H^*(\omega + \Omega) - H^*(\omega)H(\omega - \Omega) = -2i\Im[H(\omega)], \quad (3.28)$$

then gets purely imaginary, which implies that the cosine term in equation (3.27) has no contribution from the carrier and is thus not suitable for locking. Hence, the PDH error signal is derived from the sine term of equation (3.27)

$$\epsilon = -2I_0 J_0(\beta) J_1(\beta) \Im[H(\omega)H^*(\omega + \Omega) - H^*(\omega)H(\omega - \Omega)]. \quad (3.29)$$

To obtain the error signal in reflection, the cavity reflection coefficient (3.6) has to be inserted as transfer function. Figure 3.5 shows a plot of this error signal. It has steep zero crossings when the detuning is zero or equals the modulation frequency.

Near resonance the error signal has a linear steep slope and is thus well suited for feedback

3. Theory

control. Using equation (3.28), the error signal near resonance can be approximated to

$$\epsilon = -4J_0(\beta)J_1(\beta)I_0 \Im[H(\omega)]. \quad (3.30)$$

The imaginary part of the reflectivity function can be calculated from equation (3.6) to

$$\Im[H(\omega)] = \frac{\frac{\mathcal{F}}{\pi} \sin(\frac{\omega}{\Delta_{\text{FSR}}})}{1 + (\frac{2\mathcal{F}}{\pi})^2 \sin^2(\frac{\omega}{2\Delta_{\text{FSR}}})}. \quad (3.31)$$

Since the transfer function at frequencies near a cavity resonance ω_q is of interest, ω is replaced by $\Delta\omega_q = \omega - \omega_q$. Together with the approximation $\Delta\omega_q \ll \Delta_{\text{FSR}}$ this leads to

$$\Im[H(\Delta\omega_q)] = \frac{\frac{\mathcal{F}}{\pi}(\frac{\Delta\omega_q}{\Delta_{\text{FSR}}})}{1 + (\frac{2\mathcal{F}}{\pi})^2(\frac{\Delta\omega_q}{2\Delta_{\text{FSR}}})^2} = \frac{\frac{\Delta\omega_q}{\pi\Gamma_\nu}}{1 + (\frac{\Delta\omega_q}{\pi\Gamma_\nu})^2}. \quad (3.32)$$

When the detuning is smaller than the cavity linewidth ($\Delta\omega_q \ll \Gamma_\nu$), the denominator in equation (3.32) can be neglected and the transfer function can finally be approximated to

$$\Im[H(\Delta\omega_q)] \approx -\frac{\Delta\omega_q}{2\pi\Gamma_\nu} = -\frac{\Delta\nu_q}{\Gamma_\nu}. \quad (3.33)$$

This results in a linear error signal ($\epsilon = D\Delta\nu_q$) with a proportionality constant of

$$D = \frac{8J_0(\beta)J_1(\beta)I_0}{\Gamma_\nu}, \quad (3.34)$$

which is called the frequency discriminant.

Equation (3.20) reveals that the closed loop laser noise scales with the inverse of the frequency discriminant. Hence, it has to be as high as possible, which is achieved with a small cavity linewidth and a high intensity. The product $J_0(\beta)J_1(\beta)$ gets maximal for a modulation index of $\beta = 1.08$. At this modulation index the power in each sideband is half of the power in the carrier.

3.3. Piezoelectric actuation

With the presented PDH technique a laser can be stabilized to any resonance frequency of a cavity. In high finesse cavities these resonances are clearly separated from each other and the laser can thus only be stabilized to discrete frequencies. Since these frequencies are determined by the length of the cavity, this can be resolved by inserting a length changing element like a piezoelectric actuator into the optical cavity.

This section will give some basics on piezoelectricity and ferroelectricity before introducing some piezoelectric materials and treating piezoelectric actuators in more detail.

3.3.1. Fundamentals of piezoelectricity

When pressure is applied to certain electrically non-conductive materials an electric potential can be generated. This phenomenon is called piezoelectric effect and was first demonstrated in 1880 by Jacques and Pierre Curie when studying the properties of crystals like tourmaline and quartz. The piezoelectric effect can be observed in crystalline materials without inversion symmetry, which means that they have at least one polar axis. 21 of the 32 crystallographic point groups fulfill this requirement and 20 of those exhibit piezoelectricity.

Pressure along a polar axis leads to a displacement of the atoms of the unit cell in such a way, that an electric dipole forms (Figure 3.6). This change in polarization results in a change of surface charge of the crystalline material and hence in an electric field. If otherwise an electric field is applied to a piezoelectric material, the formation of an electric dipole is forced, which results in deformation of the crystal.

This inverse piezo electric effect is utilized in piezo electric actuators. The actuator length can be changed by voltage. Hence, the length and thus the resonance frequency of a cavity with incorporated piezo actuator can be changed by voltage as well.

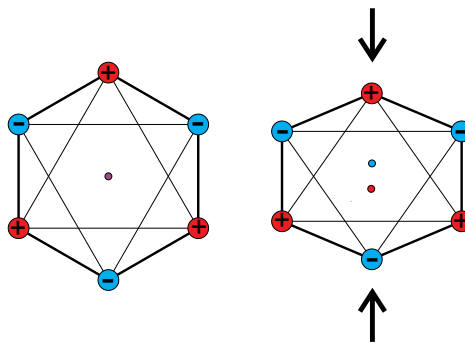


Figure 3.6.: Deformation of a piezoelectric crystal leading to a separation of the positive and negative center of charge. The result is an electric dipole.

3. Theory

Mathematical description of piezoelectricity

For a mathematical description of the piezoelectric effect four physical relations have to be considered. When an electric field E_j is applied to a dielectric material the charge separation is described by the polarization vector $P_i = \chi_{ij}E_j$ ($i,j=1,2,3$), where χ_{ij} is the susceptibility. When the polarization of the free space ($\epsilon_0 E$) is also taken into account, the total surface charge density is given by the dielectric displacement vector D :

$$D_i = \epsilon_0 E_i + P_i = \epsilon_0 \delta_{ij} E_j + \chi_{ij} E_j = \epsilon_{ij} E_j, \quad (3.35)$$

where δ_{ij} is the Kronecker delta and $\epsilon_{ij} = \epsilon_0 \delta_{ij} + \chi_{ij}$ is the dielectric permittivity.

Piezoelectric materials cannot only be polarized by an electric field but also by mechanical stress X_{ij} . The so called direct piezoelectric effect can be written by

$$D_i = d_{ijk} X_{jk}, \quad (3.36)$$

where d_{ijk} is a third rank tensor containing the piezo electric coefficients.

The relationship between stress X_{ij} applied upon an elastic material and the resulting strain x_{ij} can be described in linear approximation by Hookes's law

$$x_{ij} = s_{ijkl} X_{kl}, \quad (3.37)$$

where s_{ijkl} is the elastic compliance. In piezoelectric materials strain can also be caused by an applied electric field as described by the converse piezoelectric effect

$$x_{ij} = d_{kij} E_k = d_{ijk}^t E_k, \quad (3.38)$$

where d_{ijk}^t is the transposed of the tensor introduced in equation (3.36).

The coupling between the elastic and electrical parameters of a material can be introduced formally using the thermodynamic approach [45]. For isothermal processes equations (3.35)-(3.38) can be combined in the following set of equations

$$x_{ij} = s_{ijkl}^E X_{kl} + d_{kij}^X E_k \quad (3.39)$$

$$D_i = d_{ijk}^E X_{jk} + \epsilon_{ij}^X E_j, \quad (3.40)$$

where superscripts indicate variables held constant. Equations (3.39) and (3.40) are known as the piezoelectric constitutive equations. A further result of the thermodynamic approach is the thermodynamic equivalence of the direct and converse piezoelectric effect

$$d_{kij}^X = d_{ijk}^E = d_{ijk}. \quad (3.41)$$

Since the piezoelectric tensor, the strain tensor, the compliance tensor, and the stress tensor are symmetric, the Voigt notation can be used to simplify their form. The tensor entries $ii = 11, 22, 33$ become $m = 1, 2, 3$, which corresponds to the x, y, and z axis of the crystal, and the shear entries $ij = 23$ or $32, 13$ or $31, 12$ or 21 become $m = 4, 5, 6$. Thus, the constitutive

equations can be written as

$$x_m = s_{mn}^E X_n + d_{im} E_i \quad (3.42)$$

$$D_i = d_{im} X_m + \epsilon_{ij}^X E_j. \quad (3.43)$$

The piezoelectric tensor in this notation is a 3×6 matrix which is the form typically found in literature. The first index i denotes the component of electric displacement D or E in the Cartesian reference frame (x, y, z) and the second index m describes the mechanical stress. $m = 1, 2, 3$ corresponds to the normal stress along the x, y and z axes, respectively, whereas $m = 4, 5, 6$ corresponds to shear stress [46]. The entries of the tensor, the piezoelectric coefficients, are generally specified with the unit C/N which is equivalent to m/V.

Electrostrictive effect

When an electric field is applied to a dielectric material the induced strain has not only a linear dependency as described in equation (3.38), but also higher order terms. The second order effect

$$x_{ij} = M_{ijkl} E_k E_l. \quad (3.44)$$

is called electrostrictive effect. It is typically much smaller than the piezo effect and can thus be neglected in piezoelectric materials. However, the electrostrictive effect occurs in all dielectric materials and not only in the 20 piezoelectric point groups. There are, for example, the relaxor ferroelectrics which show not only an extremely large dielectric constant, but also an electrostrictive strain in the same order as typical piezoelectric strains.

3.3.2. Ferroelectricity

A special subset of piezoelectric materials are ferroelectrics. Ferroelectrics possess at least two equilibrium orientations of the spontaneous polarization vector whose direction can be switched between those orientations by an electric field. Ferroelectricity is thus the phenomena, that materials change their spontaneous polarization under the influence of an electric field.

Above a certain temperature called Curie temperature ferroelectrics have no spontaneous polarization and are thus not piezoelectric. Typical Curie temperatures of ferroelectrics are between 150°C and 500°C . When ferroelectrics are cooled through the phase transition at the Curie temperature, spontaneous polarization occurs whose direction does vary throughout the crystal. For example, in the perovskite structure (Figure 3.7) the spontaneous polarization takes the direction of all six axes of the cubic cell with the same probability. A ferroelectric crystal that is composed of many cells thus has a net polarization of zero and exhibits no piezoelectric properties.

The crystal tends to build regions with the same polarization which are called ferroelectric domains. Regions between two domains are called domain walls, analogous to the Weiss domains and Bloch walls in ferromagnetism. The ferroelectric domain walls are much narrower than the domain walls in ferromagnetic materials. They are in the order of 1 nm to 10 nm which corresponds to 2-3 crystal unit cells [45, 47]. By applying a strong electric field of several

3. Theory

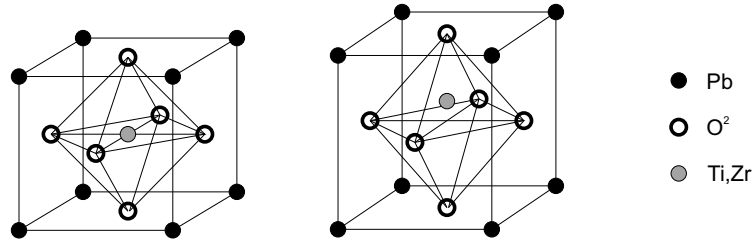


Figure 3.7.: Perovskite structure using the example of PbZrO_3 or PbTiO_3 . The solid solution of those two compounds is the most commonly used piezo material lead zirconate titanate (PZT). Left: in the cubic structure above the Curie temperature. Right: in the tetragonal structure below the Curie temperature. The center atom is randomly displaced in all six axes of the cubic cell.

ten kV/cm the domains can be reoriented along a common axis; the crystal becomes single-domain exhibiting strong piezoelectric properties.

Most ferroelectric materials are not single crystals but polycrystalline ceramics. They consist of a multitude of grains which are randomly oriented (Figure 3.8). Poling of these ceramics does not orient the grains but the domains within individual grains. The domains can be aligned along the directions that are permissible by the individual grain crystal symmetry and that lie as close as possible to the direction of the field. After this poling process the polycrystalline ferroelectric exhibits piezoelectric properties, even though there are still many domain walls present. The domain structure is an important feature of ferroelectrics that leads to special characteristics of this material class as presented in the following.

Hysteresis

When a certain voltage is applied to a ferroelectric material the resulting displacement is not only determined by the present voltage value but also by its previous displacement. This behavior is called hysteresis.

The domain structure of the ferroelectric material leads to the typical hysteresis loop as shown in Figure 3.9. For low electric fields the polarization shows a linear behavior ($P = \chi E$). When the field is strong enough to switch domains with unfavorable orientation the polarization shows a non linear behavior until all domains are aligned and the saturation polarization P_S is reached (segment a). When decreasing the electric field some domains start to switch back but at zero

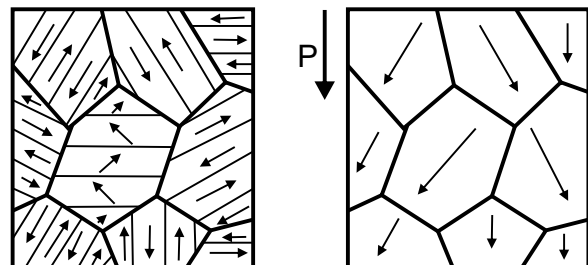


Figure 3.8: Schematic of the microstructure (grains and domains) of a ferroelectric polycrystal. Left: unpoled; right: after poling. Based on [48].

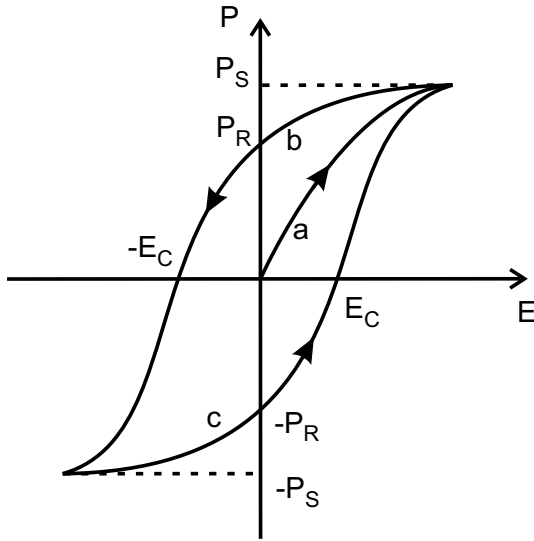


Figure 3.9: Hysteresis loop. Polarization P of a ferroelectric material as a function of the applied electric field E . P_S is the saturation polarization, P_R is the remnant polarization, and E_C the coercive field. See main text for further explanations.

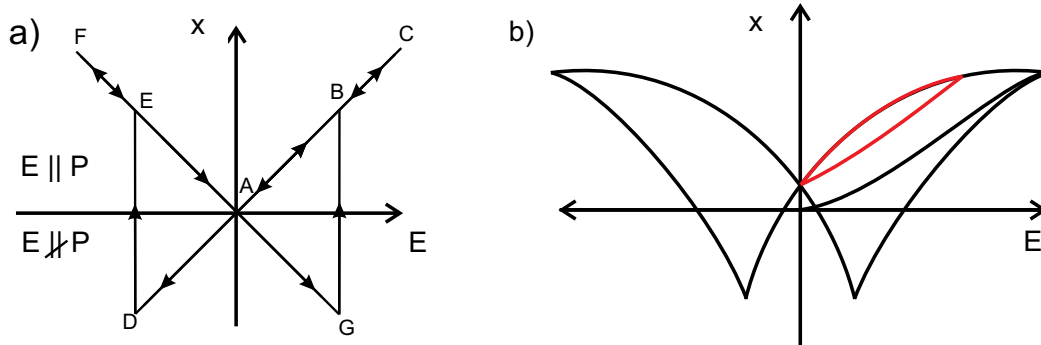


Figure 3.10.: Strain of a ferroelectric material as a function of the electric field. a) shows the typical butterfly loop for a single-domain single crystal (adapted from [45]). With increasing and decreasing electric field, the strain traces the loop ABCBA DEF EA GBCBA. When the electric field is antiparallel to the polarization, the crystal contracts until at point D and G, the electric field is strong enough to switch the polarization, so that it is again parallel to the electric field. b) shows the butterfly loop for a polycrystalline ceramic. The red marked hysteresis loop is typically observed with piezoelectric actuators, where no or only small negative electric fields are applied so that no domain switching occurs.

3. Theory

field there is still a non zero polarization, the so called remnant polarization P_R (segment b). To further decrease the polarization it is necessary to apply a negative electric field. At the coercive field E_C , the polarization finally becomes zero again. A stronger negative electric field leads to a negative polarization and continues the loop in the opposite direction (segment c).

The strain over voltage plot shows a hysteresis loop, too, which is called butterfly loop due to its characteristic shape. For an idealized single-domain single crystal the hysteresis loop has the form as depicted in Figure 3.10a. When an electric field is applied in the direction of the crystal polarization axis, a linear behavior of the strain following the converse piezoelectric effect ($x = dE$) can be observed. If the electric field is antiparallel to the polarization, the linear relation is only valid for small electric fields. Large fields switch the polarization direction so that it becomes again parallel to the electric field. For polycrystalline materials the butterfly curve has a more complicated form (Figure 3.10b) due to the various domains. In a typical actuator application the applied electric fields are kept so low that no domain switching occurs. In this case, the hysteresis loop has the form as depicted in red in Figure 3.10b.

Creep

Creep is another process which can be attributed to the domain structure of ferroelectric crystals. When a certain electric field is applied to the piezo material, a corresponding strain is induced in accordance with the converse piezoelectric effect (equation (3.38)). This ‘instant’ strain is followed by a slow additional strain change without any related voltage change. This can be explained by the fact that after changing the electric field not all domains are instantaneously oriented. The remaining unoriented domains get aligned by the resulting inner field, however with some delay. The rate of creep decreases logarithmically with time as phenomenological described by the following equation [49]

$$s(t) = s(0.1 \text{ s})[1 + \gamma \cdot \log(\frac{t}{0.1 \text{ s}})]. \quad (3.45)$$

$s(0.1 \text{ s})$ is the strain at 0.1 s after an abrupt voltage change and γ is the creep factor, which depends of the magnitude of the voltage change. For PZT ceramics it is in the order of 0.01 to 0.02 corresponding to 1% to 2% per time decade [50].

Aging

Ferroelectric materials show a time dependence of their elastic, dielectric and piezoelectric coefficients. The alteration of this coefficients in absence of external forces or temperature changes is known as aging. An important contribution to aging is the slow relaxation of the high stresses that are introduced into the ceramics during poling at elevated temperatures. The domain configuration tends to reach a new equilibrium state relieving some of the stresses. In PZT ceramics aging leads to a logarithmic decay of the piezoelectric coefficient of typically 0.01% to 2% per time decade.

3.3.3. Piezoelectric materials

There exist a large number of piezoelectric materials, which have quite different properties and are thus useful for different applications. In the following the most important types of materials will be presented including their most prominent representatives.

Natural crystals - quartz A large number of natural crystals exhibit piezoelectricity, like tourmaline or rochelle salt. The most important representative of this group is quartz. Due to its extremely low acoustic losses and the excellent stability of its piezoelectric properties with time and temperature, quartz is widely used as precision oscillator or for other applications in the field of frequency control. Quartz has the chemical composition SiO_2 arranged in a trigonal structure (α -quartz). Its piezoelectric coefficients are

$$d = \begin{pmatrix} d_{xxx} & d_{xyy} & d_{xzz} & d_{xyz} & d_{xxz} & d_{xxy} \\ d_{yxx} & d_{yyy} & d_{yzz} & d_{yyz} & d_{yxz} & d_{yyx} \\ d_{zxx} & d_{zyy} & d_{zzz} & d_{zyz} & d_{zxx} & d_{zxy} \end{pmatrix} = \begin{pmatrix} 2.3 & -2.3 & 0 & -0.67 & 0 & 0 \\ 0 & 0 & 0 & 0 & 0.67 & -4.6 \\ 0 & 0 & 0 & 0 & 0 & 0 \end{pmatrix} \cdot 10^{-12} \frac{\text{m}}{\text{V}}. \quad (3.46)$$

Like all natural crystals, quartz has a relatively small piezoelectric strain and is thus seldom used in actuator applications.

Ferroelectric ceramics - PZT In the 1940s, ferroelectric ceramics like Barium titanate were discovered to be piezoelectric during and after exposing the ceramic to a high electric field. A few years later, excellent piezoelectric performance was found in lead zirconate titanate (PZT). PZT is a ferroelectric solid solution with the chemical formula $\text{Pb}[\text{Zr}_x\text{Ti}_{1-x}]\text{O}_3$. Above the Curie temperature, PZT has cubic perovskite structure with a Zirconium or Titanium atom in the center (Figure 3.7). Below the Curie temperature, the lattice changes to a tetragonal or rhombohedral structure leading to a displacement of the center atom. At room temperature, the unit cell thus shows a dipole moment and has piezoelectric properties. Whether the lattice changes in a tetragonal or rhombohedral structure, depends on the mixing ratio of PbZrO_3 and PbTiO_3 [48] (Figure 3.11). Near the boundary between these two phases, the morphotropic phase boundary (MPB), the PZT ceramic exhibit a large piezoelectric coefficient. This is a result of enhanced polarizability, which arises from the coupling between the two equivalent energy states and allows optimum domain reorientation during the poling process.

The properties of the PZT ceramics can be modified by doping the material. Acceptor doping leads to hard PZT, donor doping to soft PZT. Soft PZT can be polarized more easily, leading to a higher piezoelectric constant, but lower electrical and mechanical resistivity. The exact values of the piezoelectric constant thus depend on the particular composition of the ceramic. For instance, the piezoelectric tensor of a typical PZT ceramic, PZT-5A, has the form

$$d = \begin{pmatrix} 0 & 0 & 0 & 0 & 584 & 0 \\ 0 & 0 & 0 & 584 & 0 & 0 \\ -171 & -171 & 374 & 0 & 0 & 0 \end{pmatrix} 10^{-12} \frac{\text{m}}{\text{V}} \quad (3.47)$$

3. Theory

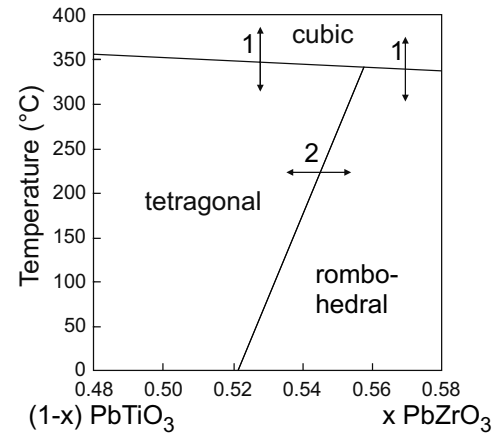


Figure 3.11: Phase transitions of PZT ceramics at the polymorphic (1) and at the morphotropic (2) phase boundary. Based on [48].

High piezoelectric coefficients, a simple fabrication process, the possibility of variable shaping, as well as low-cost manufacturing have made PZT the most widely used piezoelectric material. Thus, PZT has even become a synonym for piezoelectric elements in the everyday language.

Relaxor based ferroelectric single crystals - PZN-PT Relaxor ferroelectrics are characterized by a strong dispersion of the dielectric constant. The dielectric constant drops off rapidly with frequency, what led to the designation "relaxor". Like PZT, solid solutions of relaxor ferroelectrics and PbTiO_3 have a morphotropic phase boundary, but exhibit even higher piezoelectric coefficients near this boundary. One representative of this class is PZN-PT with the chemical formula $(1-x)\text{Pb}(\text{Zn}_{1/3}\text{Nb}_{2/3})\text{O}_3 - x\text{PbTiO}_3$. For $x < 8$ it shows a rhombohedral structure and, when oriented along its pseudocubic $\langle 001 \rangle$ direction, exhibits large piezoelectric coefficients ($d_{33} > 2500 \text{ pm/V}$) near the MPB. In contrast to PZT, PZN-PT can be grown in a single crystal form using the high temperature flux technique.

Electrostrictive materials Electrostrictive materials like the relaxor material lead magnesium niobate (PMN) are also used for actuator applications. In comparison to PZT, PMN shows lower hysteresis in a certain temperature range and is less sensitive to pulling forces. The disadvantages are a higher capacitance (and thus the need of a higher drive current) and a higher dependency on temperature changes.

Polymers Piezoelectricity is also present in polymers like polyvinylidene fluoride (PVDF). The piezoelectricity in this polymer class arises from the strong molecular dipoles within the polymer chain. PVDF has moderate piezoelectric coefficients (d_{33} around $20\text{-}30 \text{ pC/N}$) and is supplied in the form of a thin film. It is thus suitable for applications as ultrasonic transducers or pressure sensors, but is typically not used as actuator material.

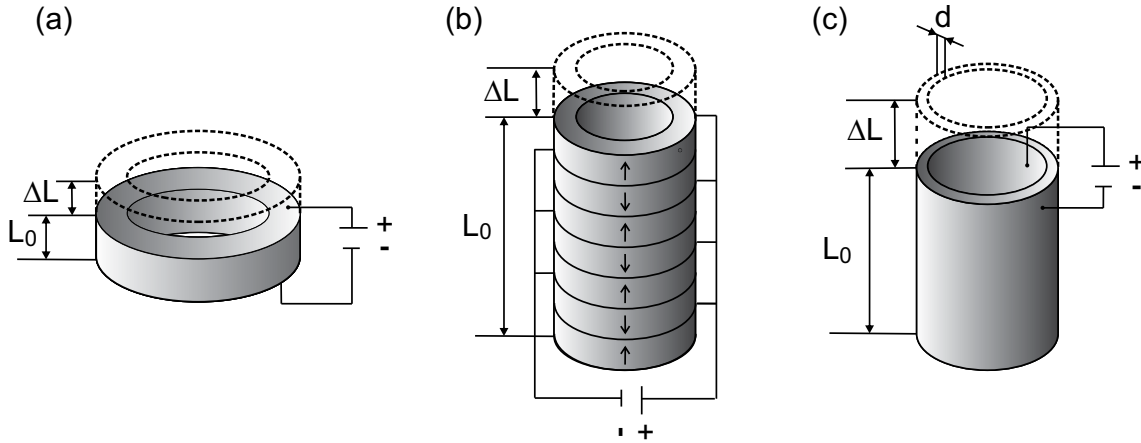


Figure 3.12.: Types of piezoelectric actuators. (a) piezoelectric ring actuator (b) stack actuator (c) tube actuator. The arrows in figure b) indicate the polarization of the individual actuators.

3.3.4. Piezoelectric actuators

The described materials can be used to build piezoelectric actuators. Piezoelectric actuators make use of the converse piezoelectric effect $x_j = d_{ij}E_i$. When the electric field is applied in poling direction, a longitudinal piezo effect

$$x_3 = d_{33} \cdot E_3 \quad (3.48)$$

can be observed, as well as a transversal piezo effect

$$x_1 = d_{31} \cdot E_3. \quad (3.49)$$

Actuator types

Disc or ring actuator The length change ΔL of an actuator along the direction of the electric field E_3 (Figure 3.12a) does only depend on the applied voltage U and the piezoelectric coefficient

$$\Delta L = x_3 L_0 = E_3 d_{33} L_0 = d_{33} \frac{U}{L_0} L_0 = d_{33} U. \quad (3.50)$$

The dimension of the piezoelectric device is of no importance. This can be explained by the fact that the charge displacements of the unit cells inside the crystal are compensated by the next unit cell. Only the unit cells at the end faces of the crystal contribute to the piezoelectric displacement. To increase stroke, several actuators either have to be connected in series or the transversal piezo effect must be used.

Stack actuators Several actuators in series are called stack actuator. A stack of ceramic layers is separated by thin metal electrodes. Two adjacent ceramic layers have opposite polarization,

3. Theory

as schematically shown in Figure 3.12b, so that the alternating positive and negative electrodes always generate an electric field along the polarization axis. The layer thickness is typically between 0.4 mm and 1 mm. The displacement of the n different layers accumulate and formula (3.50) changes to

$$\Delta L = n \cdot d_{33} \cdot U. \quad (3.51)$$

Typical PZT stack actuators have a potential strain of up to 1%.

Multilayer actuators A multilayer actuator is a special kind of stack actuator, where the thin PZT ceramic layers are provided with electrodes before sintering. These layers are stacked and then sintered together (cofired) to create a monolithic piezo ceramic block. The multilayer blocks produced in this way have a higher life time and reliability than conventional piezo stacks.

Tube actuators Piezo tubes make use of the transversal piezo effect. The electric field is applied between the inner and outer wall of a piezo electric tube with a wall thickness d as shown in Figure 3.12c. In this geometry, the resulting displacement depends on the dimensions of the actuator: the thinner the wall and the longer the tube the bigger the displacement:

$$\Delta L = d_{31} E_3 \cdot L = d_{31} \cdot \frac{U}{d} \cdot L. \quad (3.52)$$

Shear actuators If the electric field is not applied in poling direction but perpendicular to it, shear forces arises, which lead to a lateral displacement of the actuator surface. This displacement is larger than that of linear actuators, because the corresponding piezo coefficient d_{15} is larger (equation (3.47)). Shear actuators are used in applications such as piezo linear motors.

Operation of piezoelectric actuators

Voltages Commercially available piezo actuators are typically either designed for high voltage operation, which means that up to 1000 V can be applied to the actuator, or for low voltage operation, where a maximum voltage of 150 V can be applied. Ferroelectric actuators can only be operated with negative voltages of about 20% of the maximum applicable positive voltage, since higher negative electric fields would lead to depoling of the actuator.

Loads PZT ceramics are brittle and can thus not withstand high tensile or shear forces. They can be loaded with pressure of up to 250 MPa without breaking. However, depoling arises already at 20 to 30 % of this pressure. Maximum allowed tensile forces are only 5 to 10 % of this value and shear forces are to be avoided completely. Hence, prestressed actuators have to be used for applications with high tensile or shear forces.

If a piezoelectric actuator with a stiffness k_P is loaded with a constant force F , it is compressed by $\Delta L = F/k_P$, while the full displacement range of the actuator is still available. If the actuator is loaded with an elastic load, the maximum displacement is reduced and the effective displacement gets

$$\Delta L = \Delta L_0 \frac{k_P}{k_P + k_S}, \quad (3.53)$$

where k_S is the stiffness of the elastic load and ΔL_0 the nominal displacement without external force or restraint.

The stiffness of the piezo actuator depends on whether the actuator is short circuited or not. When an actuator with open electrodes is compressed, an electric field builds up (due to the piezo effect) which imposes a counterforce opposing the mechanical stress. Thus, actuators with open electrodes show a higher stiffness than short circuited piezo actuators. In typical actuator applications, the piezo is driven with a low output impedance voltage supply and consequently the short circuited stiffness has to be considered.

Dynamic operation A piezo actuator can be considered as a spring mass system with an effective mass of $m_{\text{eff}} = \frac{1}{3}m + M$ [51], where m is the mass of the actuator and M any additional mass attached to it. The resonance frequency of such a system is

$$f_0 = \frac{1}{2\pi} \sqrt{\frac{k_P}{m_{\text{eff}}}}. \quad (3.54)$$

PZT stack actuators typically have resonance frequencies of a few ten kilohertz. When operated in a servo loop, these resonances may limit the bandwidth of the feedback.

When a piezoelectric actuator is driven with a sinusoidal signal, the actuator is exposed to a force, which increases quadratically with the frequency [51]

$$F = \pm 4\pi^2 m_{\text{eff}} \left(\frac{\Delta L}{2}\right)^2 f^2. \quad (3.55)$$

Thus, to avoid excessive tensile forces, frequencies higher than a few hundred kilohertz can only be applied when the actuator is prestressed.

4. Experimental Implementation

The previous chapter provided theoretical foundations of piezo-tunable cavities and their application as frequency references. This chapter will now present the technical implementation of such a tunable frequency reference. Four cavities with different piezo actuators have been assembled to investigate the influence of piezo actuators on the frequency stability of an optical cavity. In the following, the tested cavities will be described in detail and it will be estimated how various external effects influence the frequency stability of these cavities. Furthermore, the test setup in which the piezo-tunable cavities were investigated will be presented.

4.1. Cavities with incorporated piezo actuator

The piezo-tunable cavities consist of a Zerodur spacer, one or two piezo actuators, and fused silica mirrors. The frequency stability of a cavity stabilized laser depends on the stability of the over all length of the cavity. Thus, the thermal and mechanical properties of the incorporated piezo actuators need to be carefully chosen. In the following, the employed piezo actuators will be described in detail before more information about the cavity assemblies will be given.

4.1.1. The piezoelectric actuators

The four different piezo actuators that were selected to be integrated in a cavity are a stack actuator and a tube actuator made from lead zirconate titanate (PZT), a quartz crystal, and a lead zinc niobate - lead titanate (PZN-PT) single crystal. The applied actuators are listed in Table 4.1 with supplier information, dimensions and nominal tuning range. Those actuators were chosen since, on the one hand, they were available in a ring shaped version, which is import for

actuator	supplier (type)	L (mm)	OD (mm)	ID (mm)	$\Delta L/U$ (nm/V)
PZT stack	PI (Pica™ Thru)	7	25	16	5
PZT tube	PI (PT tube)	10	20	18	2.1
PZN-PT	microfine	3	13	10	1.9
quartz	Boston piezo-optics	5	25	16	0.0023

Table 4.1.: List of the applied piezo actuators. L: length, OD: outer diameter, ID inner diameter. The tuning coefficients $\Delta L/U$ are calculated using equations (3.50) and (3.51) and the appropriate piezoelectric coefficients. In the case of the PZT stack actuator, the nominal tuning range was specified by the manufacturer.

4. Experimental Implementation

Material	d_{ij} (pm/V)	CTE ($10^{-6}/\text{K}$)	E (GPa)	Q
PZT (PIC151)	d_{33} : 500 d_{31} : -210	-5	60	100
quartz	d_{11} : -2.3	13	76.5	200 000
PZN-(6-7)%PT	d_{33} : 1910	< 10	62.5	100
Zerodur	-	<0.02		3100
ULE	-	<0.02		61 000

Table 4.2.: Relevant properties of the piezo materials used in this work: PZT (PI ceramics, PIC 151), quartz (Boston Piezo-Optics, crystal quartz) and PZN-PT (Microfine Materials Technologies, PZN-(6-7)%PT single crystals). d_{ij} denotes the piezoelectric coefficient, CTE the coefficient of thermal expansion, E the Young’s Modulus and Q the mechanical quality factor. For the PZN-PT single crystal no CTE value could be found in the literature; the given value is derived from own measurements. It should be noted that the listed values describe only the pure piezo material and do not account for adhesive or electrodes as used in the case of the PZT stack actuator. For these reasons, e.g, the stack actuator actually has a CTE of $3.5 \times 10^{-6} / \text{K}$.

the integration in a cavity configuration. On the other hand, they have quite different material properties whose influence on the frequency stability may provide interesting information.

The properties of the piezo materials which are relevant for the use in a cavity are given in Table 4.2. The CTE of all these piezo materials is more than two orders of magnitude higher than that of cavity spacer materials like Zerodur or ultra low expansion glass (ULE), which may influence the long term performance of a cavity with an incorporated piezo actuator. The Young’s modulus (E), which should be high to provide a low vibration sensitivity as well as a low thermal noise level, is of the same order of magnitude as that of Zerodur or ULE. The mechanical quality factor (Q), which should be high to achieve a low thermal noise level, shows significant differences between the piezo materials as well as in comparison to Zerodur and ULE.

PZT ceramic was selected as the typical actuator material; two different types of PZT actuators were tested as differences in the mechanical stability of a stack actuator, which consists of many PZT and electrode layers, and a tube actuator, where the transversal piezo effect is used, were expected. Quartz is typically not used in actuator applications due to its low piezoelectric coefficient, but it is nevertheless an interesting material because of its high Q-factor. The relaxor ferroelectric PZN-PT has a high piezoelectric coefficient and contrary to PZT, it is available as single crystal, which may have a better mechanical stability.

In the case of the PZT stack and PZT tube actuator, the wires for electrical control are positioned at the side of the actuator. In the case of the PZN-PT and the quartz actuator the wires would have to be contacted to the electrodes on the end faces of the actuators, which would interfere with a proper assembly of the cavity. For this reason, these two actuators had to be modified as shown in Figures 4.1a and 4.1b. The wiring of the PZT stack actuator was done by the manufacturer. The PZT tube actuator and the quartz actuator had to be electrically connected by soldering, taking care that the PZT ceramic does not get too hot ($< 250^\circ\text{C}$) to avoid depoling. The PZN-PT actuator is even more sensitive to high temperature, which is why

4.1. Cavities with incorporated piezo actuator

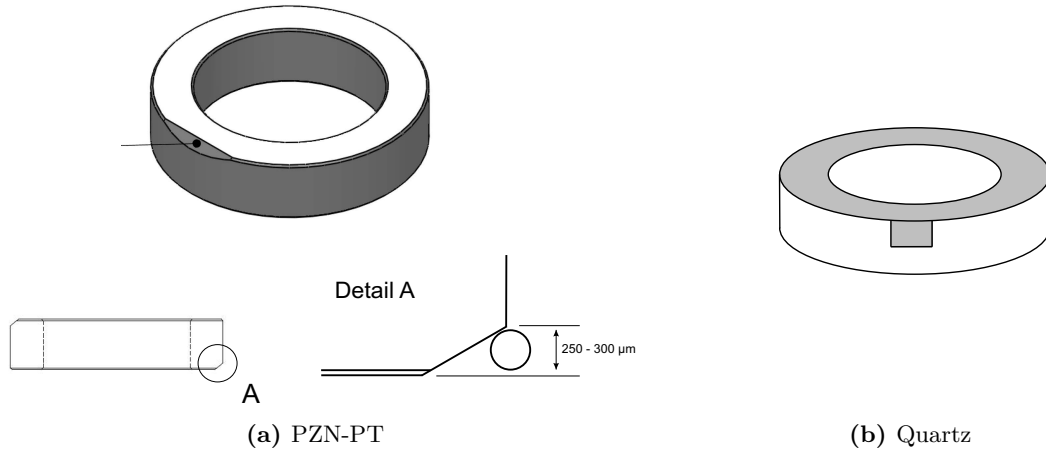


Figure 4.1.: Modifications of the actuators for proper wiring. The electrodes are applied to the end faces of the actuators. To allow wiring without corrupting the flatness of the end faces, a sort of pronounced chamfer was machined to the PZN-PT actuator (left). For the quartz actuators, this issue was solved by extending the electrodes to the circumference of the quartz rings in the form of two tabs (right).

the cables were connected by gluing using an electrically conductive adhesive (Chemtronics, CircuitWorks Conductive Epoxy).

4.1.2. The cavities

The actuators described above were used to build four cavities which consist of a Zerodur spacer, one or two piezo actuators, and one plane and one concave fused silica mirror. The Zerodur spacer is 10 cm long, 5 cm in diameter, and has a center borehole with a diameter of 1 cm. The 1 inch or 1/2 inch sized mirrors are coated for high reflectivity at 1064 nm with a targeted finesse of 300 000. The curved mirrors have a radius of curvature of 50 cm. The cavities have either been built by attaching one piezo between spacer and plane or curved mirror or by attaching piezo actuators between spacer and mirrors on both sides (Figure 4.2 and Table 4.3). For the assembly of the cavity with the PZT tube actuator, 1 inch Zerodur adapter rings with a thickness of 5 mm were installed between each actuator and mirror such that no adhesive had to be applied to the mirror surfaces. The same kind of adapter was used in the assembly of the cavity with PZN-PT actuator between spacer and actuator. In addition, a 2 mm thick fused silica adapter ring was applied between actuator and mirror. Here, the adapters were applied so that the electrical conductive adhesive used for wiring has no contact with the cavity mirror and spacer. Figure 4.3 shows photographs of the assembled piezo-tunable cavities, while Table 4.4 lists further specifications.

The cavity parts were joined together using the low-outgassing epoxy Eccobond 285, which has a high viscosity and a relatively low CTE ($3 \times 10^{-5} \text{ 1/K}$). The spacer was positioned vertically and the actuator and mirror were placed on top of it. A weight (200 g) was placed on top of the assembly to press the parts together during gluing and curing. The adhesive was not applied

4. Experimental Implementation

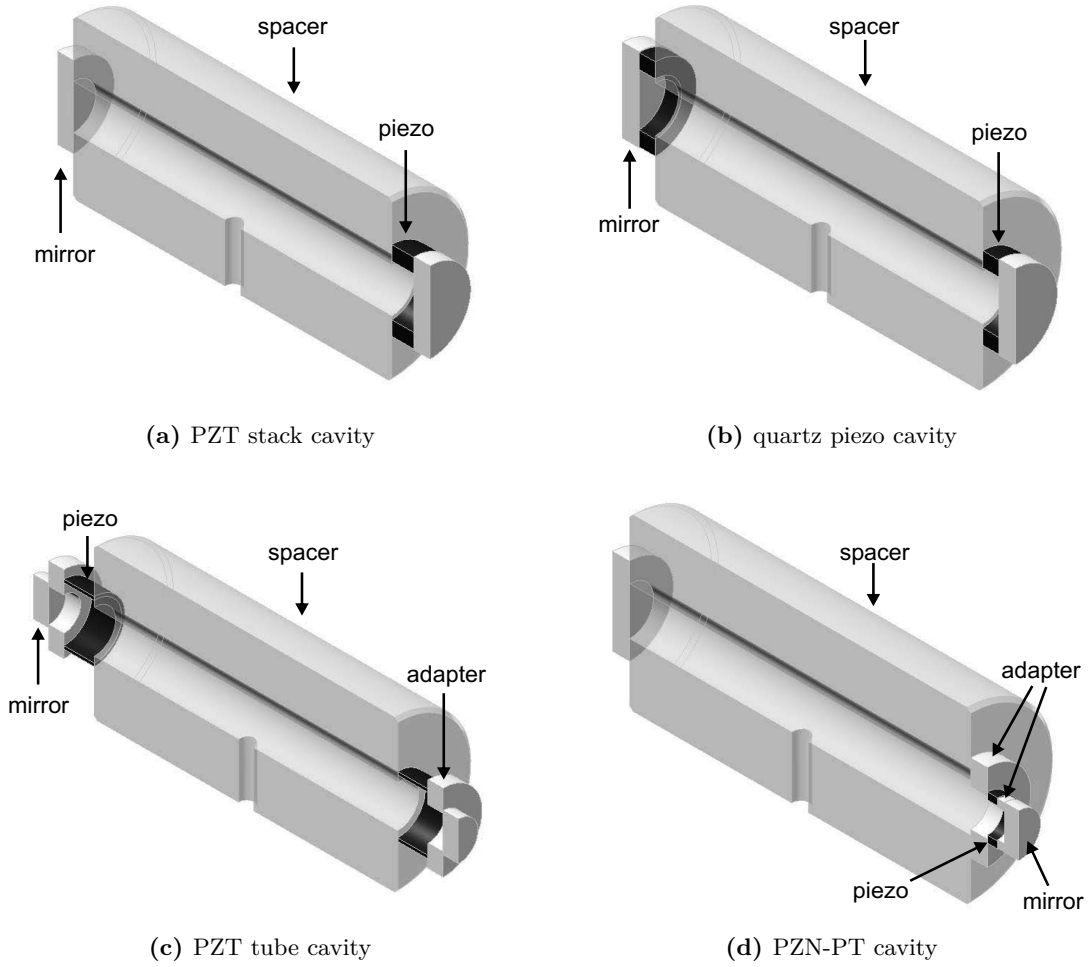


Figure 4.2.: Details on the assembly of the piezo-tunable cavities, cross-sectional view. The piezo actuator is always depicted in black.

		PZT stack	PZT tube	quartz	PZN-PT
piezo position		p	p+c	p+c	c
mirrors	plane	1"	1/2"	1"	1"
	curved	1"	1/2"	1"	1/2"
adapters		-	2·Z	-	Z+FS

Table 4.3.: Details on the cavity assembly. The piezo position ‘p’ denotes that the piezo actuator is attached on the side with the plane mirror and ‘c’ on the side with the curved mirror. The diameter of the plane and the curved mirror is stated in the next two lines. The row ‘adapters’ points out which adapters were used for building the cavities and in which quantity. ‘Z’ denotes the Zerodur adapter and ‘FS’ the fused silica adapter described in the main text.

4.1. Cavities with incorporated piezo actuator

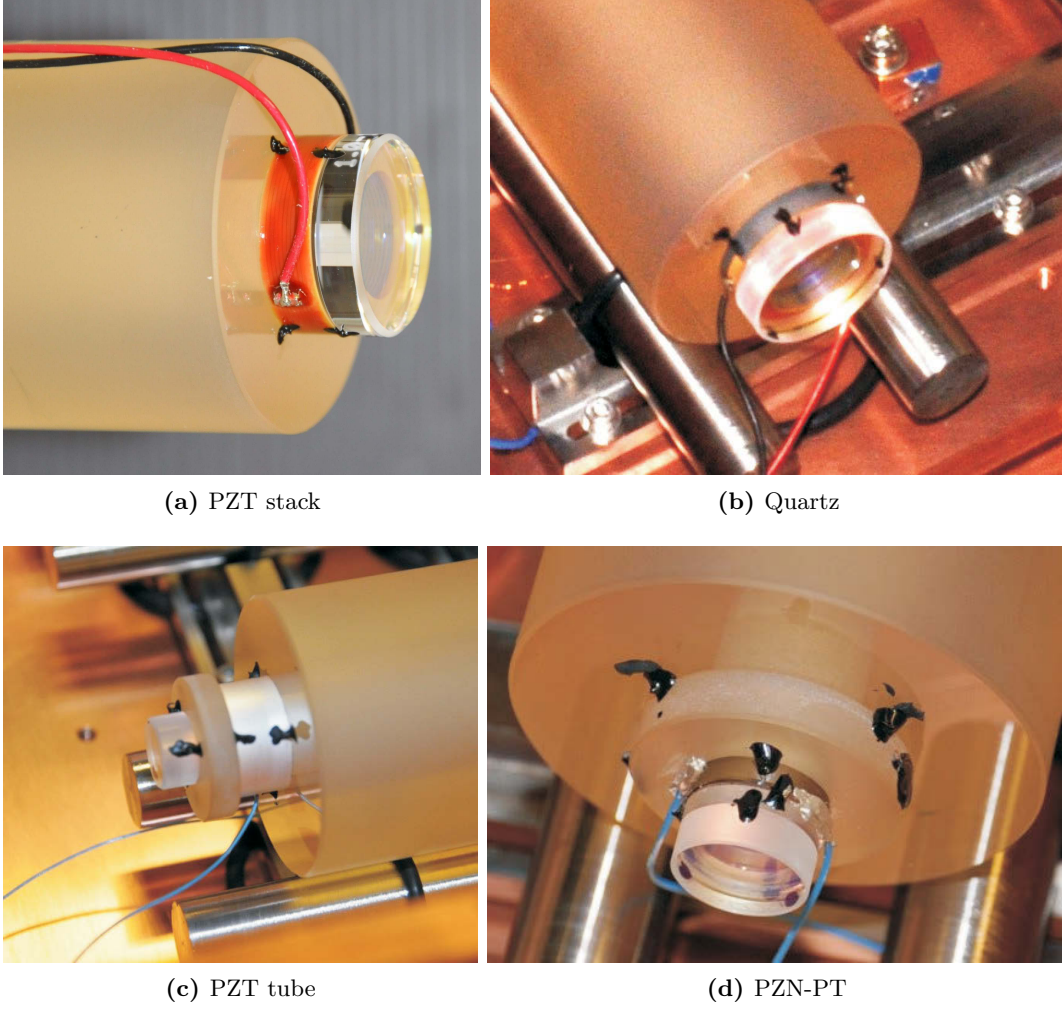


Figure 4.3.: Pictures of the cavities with incorporated piezo actuator. The adhesive is clearly visible as black spots.

		PZT stack	PZT tube	quartz	PZN-PT	fixed
L_C	(mm)	107	130	110	110	100
FSR	(GHz)	1.4	1.15	1.36	1.36	1.5
$w_{0,p}$	(μm)	264	273	265	265	260
$w_{0,c}$	(μm)	297	317	300	300	291
$\Delta\nu/U$	(MHz/V)	13.2	9.1	0.0012	4.9	-

Table 4.4.: Specifications of the piezo-tunable cavities assembled within this work. L_C is the length of the assembled cavity, FSR the free spectral range, $w_{0,p}$ the beam waist on the plane mirror, and $w_{0,c}$ the beam waist on the curved mirror. $\Delta\nu/U$ describes the expected frequency/voltage tuning coefficient of the cavities.

4. Experimental Implementation

between the parts but at the outside. Each attachment was done with three adhesive points or bridges to easily disassemble the cavities after characterization. Thus, it was possible to test different piezo materials in a cavity configuration using the same spacer.

Furthermore, a ‘fixed’ cavity with both mirrors optically contacted has been built using an identical spacer. This cavity serves as a reference to characterize the cavities with incorporated piezo actuator. Placed in the same test environment as the tunable cavities, the fixed cavity allows to distinguish between piezo related effects or environmental effects on the frequency stability. In this way, more information about the influence of the piezo actuators can be obtained.

4.2. Noise sources and environmental disturbances

The stability of a cavity stabilized laser depends on the cavity stability and on the laser lock performance

$$\frac{\delta\nu}{\nu} = -\frac{\delta L}{L} + \delta_{\text{lock}}. \quad (4.1)$$

There are several effects that degrade the frequency stability by either changing the cavity length or the lock error signal. The cavities have thus to be tested in an appropriate setup that suppresses most of the effects. To design such a test environment it is necessary to know potential noise sources and disturbances. Therefore, several effects that influence the frequency stability have been analyzed and will be described in the following. They are classified according to how the effect depends on the use of a piezo actuator within the cavity configuration.

4.2.1. Effects independent of the piezo actuator

The first examined effects have in common that their influence on the laser frequency stability does not depend on the piezo actuator. They either affect the lock performance or change the optical path length of the cavity without changing the actual spacer length. Thus, the suppression of those effects requires the same effort as in other cavity experiments.

Detector noise

According to equation (3.20), noise in the detection system may compromise the performance of a cavity stabilization system. Of special interest is the quantum shot noise of the light on the photo detector that sets a fundamental limit on the frequency stability.

The PDH stabilization scheme (Section 3.2.2) requires a phase modulated laser. When the frequency of this phase modulated laser is in resonance with the cavity, that is assumed to be perfectly impedance and mode matched, the carrier is completely transmitted and only the sidebands reflect off the cavity and fall on the photodetector. Considering only the two first order sidebands, the average intensity measured by the photodetector is thus $2J_1^2(\beta)P_0$. This intensity leads to a shot noise spectral density of [41]

$$S_A = \sqrt{2}\sqrt{2eI} = \sqrt{2}\sqrt{2e(2J_1^2(\beta)\frac{e\eta P_0}{h\nu})}, \quad (4.2)$$

where e is the elementary charge, I the detector photocurrent, $J_k(\beta)$ the Bessel function, η the quantum efficiency of the photo detector, P_0 the laser power impinging on the cavity, h the Planck constant, and ν the laser frequency. The frequency noise arising from this shot noise current can be calculated with the discriminator slope (3.34), which is expressed in units of A/Hz by

$$D_A = \frac{8J_0(\beta)J_1(\beta)}{\Gamma_\nu} \frac{e\eta P_0}{h\nu}. \quad (4.3)$$

Γ_ν is the linewidth of the cavity resonance.

4. Experimental Implementation

According to equation (3.20), the closed loop spectral density of the laser, when stabilized with sufficient servo gain, is thus

$$S_f = \frac{S_A}{D_A} = \frac{\Gamma_\nu}{J_0(\beta)} \sqrt{\frac{h\nu}{8\eta P_0}}. \quad (4.4)$$

Assuming typical values of a cavity stabilization setup, i.e. $\beta = 1.08$, $\eta = 0.7$, $P_0 = 20 \mu\text{W}$, and $\Gamma_\nu = 5 \text{ kHz}$ a value of

$$S_f = 0.3 \text{ mHz}/\sqrt{\text{Hz}} \quad (4.5)$$

can be calculated. This value is well below the required $30 \text{ Hz}/\sqrt{\text{Hz}}$ and also below the frequency noise of the best non-tunable cavities, which is about $50 \text{ mHz}/\sqrt{\text{Hz}}$. With this power level, detector noise should thus not be a critical noise source when realizing shot noise limited detection.

Intensity fluctuations

A small part of the laser light, which couples into the cavity is absorbed in the cavity mirrors. This leads to a heating of the cavity. Due to thermal expansion the length, and thus the resonance frequency of the cavity changes according to the light intensity. Consequently, intensity noise causes frequency noise. A model for this photothermal noise has been developed by Cerdonio *et al.* [52]. The frequency dependent displacement noise $S_x(\omega)$ caused by intensity noise $S_I(\omega)$ can be expressed by

$$S_x(\omega) = \frac{2}{\pi} (1 + \sigma) \frac{\alpha}{\kappa} A S_I(\omega) K(\omega/\omega_c), \quad (4.6)$$

where σ is the Poisson ratio, α the CTE, κ the thermal conductivity, A the absorption coefficient of the mirrors, and $K[\omega/\omega_c]$ a shape function. The shape function is $\sim \omega_c/\omega$ for $\omega \gg \omega_c$ and ~ 1 for $\omega \ll \omega_c$. The critical frequency ω_c is the inverse of the thermal relaxation time with

$$\omega_c = \frac{\kappa}{\rho C r_0^2}, \quad (4.7)$$

where ρ is the mass density, C the specific heat capacity and r_0 the laser beam radius.

With this model and using $\delta\nu/\nu = -\delta L/L$, the sensitivity to intensity changes in the low frequency range ($\omega \ll \omega_c$) can be estimated to

$$\frac{\delta\nu}{\delta I} = \frac{2}{\pi} (1 + \sigma) \frac{\alpha}{\kappa} \cdot A \cdot \frac{\nu}{L} \approx 800 \text{ Hz/W}. \quad (4.8)$$

For the calculation of the sensitivity, A was assumed to be 1 ppm and the material properties of fused silica were used. Typically, a few $10 \mu\text{W}$ are coupled into the cavities. Even with intensity fluctuations of 1 % the resulting frequency fluctuations are below 1 mHz.

Intensity fluctuations can also affect the stability performance by shifting the lock point. Intensity fluctuations cause amplitude changes of the error signal. If the error signal crosses zero exactly when the laser is on resonance, a change of the error signal amplitude has no impact on the lock point (Figure 4.4a). However, if an offset is present, a change in amplitude

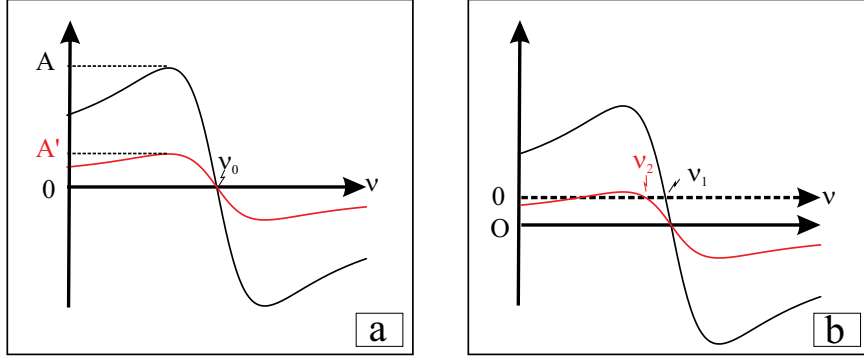


Figure 4.4.: Influence of amplitude changes of the error signal with (a) and without (b) an offset of the error signal. Graph adapted from [54].

causes a lock point shift (Figure 4.4b) and thus a frequency change. Constant error signal offsets are easily compensated electronically. Varying offsets caused, e.g. by residual amplitude modulation (RAM), parasitic resonators, or temperature changes in the lock electronics, would require an active compensation [53].

Beam pointing fluctuations

Beam pointing fluctuations change the incoupling in the cavity and thus the intensity in the cavity. If the incident beam has a parallel displacement of a_x to the fundamental mode, the percentage of the light that couples into the cavity is [55]

$$p(a_x) \approx 1 - (a_x/w_0)^2, \quad (4.9)$$

where w_0 is the waist of the fundamental mode. An angular misalignment of α_x leads to a percentage of

$$p(\alpha_x) \approx 1 - (\alpha_x/\frac{\lambda}{\pi w_0})^2 \quad (4.10)$$

that couples into the cavity. For example, with a beam waist of $260 \mu\text{m}$ and a displacement of $100 \mu\text{m}$ or an angular misalignment of 0.5 mrad only 85% of the light couples in the cavity. Beam pointing fluctuations thus lead to intensity fluctuations in the cavity, which causes frequency fluctuations as described in the previous section

Furthermore, beam position fluctuations on the photo detectors can shift the lock point and lead to frequency fluctuations. In general, photo diodes are not uniformly fabricated and the measured photo current depends on the exact position of the beam spot. Moreover, the imperfect incoupling into the cavity due to beam pointing fluctuations leads to interference effects between the TEM_{00} mode and non-resonant higher-order spatial modes, which are sensed by a not uniformly fabricated photo diode. The effect is similar to that intentionally used in the tilt locking technique [56]. To suppress beam pointing fluctuations highly stable optomechanics have to be used in the setup.

4. Experimental Implementation

Parasitic resonators

Reflecting elements in the optical setup can build a parasitic resonator, also called etalon, which acts as an additional frequency discriminator and does thus influence the PDH error signal. Hence, for the calculation of the error signal, equation (3.23) has to be modified by combining the modulated laser field not only with the cavity transfer function H , but also with the transfer function of the parasitic resonator H_E :

$$E_H(t) = E_0 \sum_{k=-\infty}^{\infty} J_k(\beta) H(\omega + k\Omega) H_E(\omega + k\Omega) e^{-i(\omega + k\Omega)t}. \quad (4.11)$$

A parasitic resonator as a resonator with very low finesse causes an oscillation of the error signal baseline (Figures 4.5a and 4.5b). The position of the oscillation relative to the error signal depends on the frequency where the parasitic resonator has maximum transmission in comparison to the cavity resonance frequency. When the length of the parasitic resonator is varying due to temperature fluctuations, the offset of the two frequency changes which leads to fluctuations of the error signal zero point and thus to lock-point shifts (Figure 4.4).

The influence of a parasitic resonator depends on the length and finesse of the parasitic resonator, the linewidth and coupling efficiency of the high finesse cavity as well as on the modulation frequency. When the modulation frequency is equal to the FSR of the parasitic resonator, carrier and sidebands are shifted equally and the parasitic resonator has no effect on the error signal. Accordingly the maximal effect is given when the modulation frequency is half the FSR.

To minimize the influence of parasitic resonators, it must be ensured that all optical parts have an antireflection coating and are mounted slightly tilted in the beam path, if possible. Also a compact optical setup with a short beam path is helpful. A further possibility is to actively stabilize the length of the parasitic resonator, e.g. by stabilizing the length of an optical fiber that is in the optical beam path of the parasitic resonators [57, 58].

Residual amplitude modulation

In a real system, phase modulation of the laser light cannot be done without residual amplitude modulation (RAM). The purely phase modulated laser beam from equation 3.21 becomes

$$E_{\text{RAM}}(t) = E_0(1 + A \cos(\Omega t + \phi)) e^{i(\omega t + \beta \sin \Omega t)} \quad (4.12)$$

$$= E_0 [e^{i(\omega t + \beta \sin \Omega t)} + \frac{A}{2} e^{i((\omega + \Omega)t + \beta \sin \Omega t + \phi)} + \frac{A}{2} e^{i((\omega - \Omega)t + \beta \sin \Omega t - \phi)}], \quad (4.13)$$

where A is the amplitude and ϕ the phase of the residual amplitude modulation. Using Bessel functions, this can be expressed by

$$E_{\text{RAM}}(t) = E_0 \sum_{m=-\infty}^{\infty} J_m^a(\beta) e^{i(\omega + m\Omega)t} \quad (4.14)$$

4.2. Noise sources and environmental disturbances

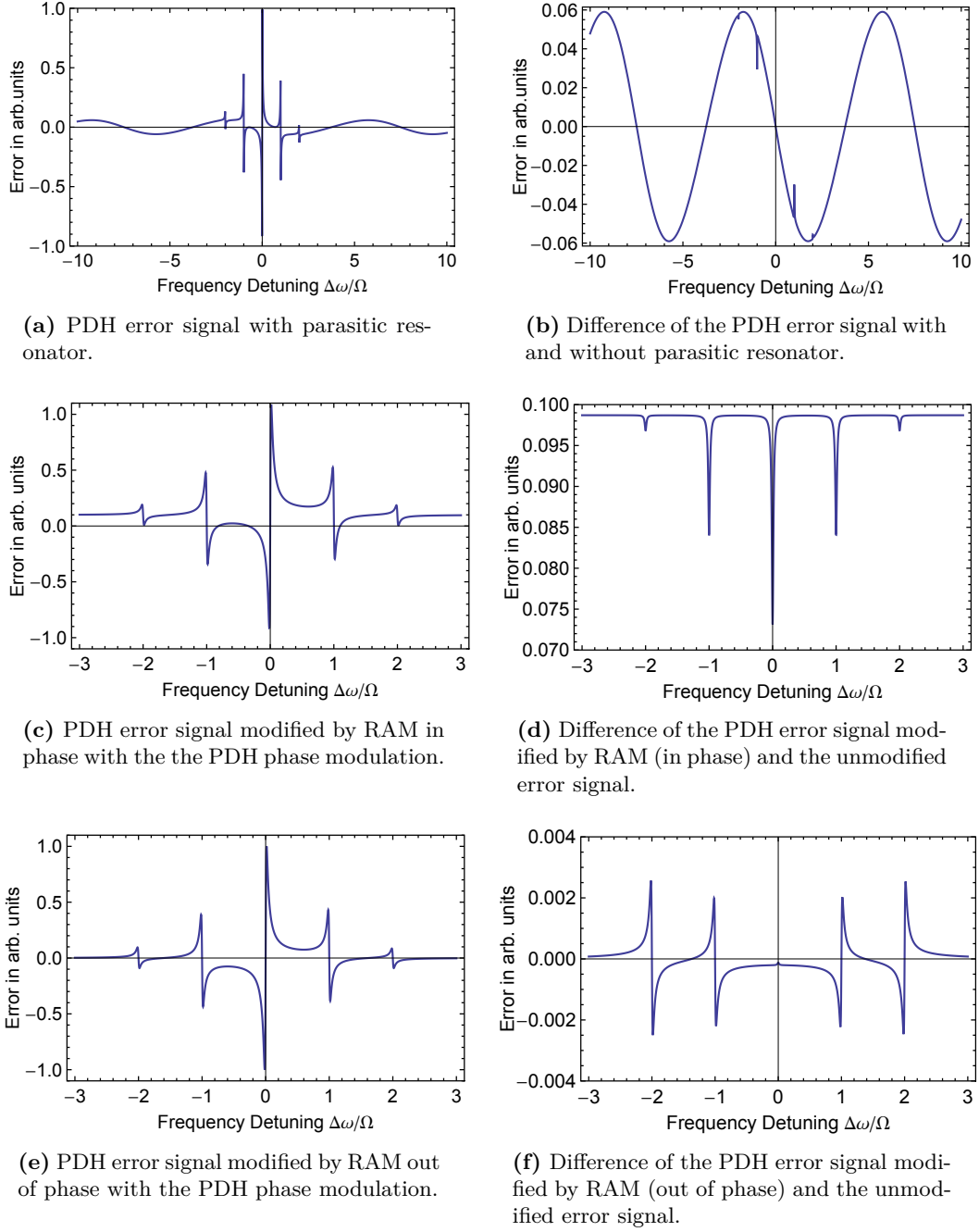


Figure 4.5.: Modification of the error signal by a parasitic resonator and RAM. The graphs are calculated for a cavity resonance linewidth of 15 kHz, a finesse of 100 000, a coupling efficiency of 50% and a PDH modulation frequency of 1 MHz. For the parasitic resonator a reflectivity of 2% for both mirrors and an optical path length of 20 m was taken for calculation. The RAM amplitude is 10% of the modulation amplitude.

4. Experimental Implementation

with

$$J_k^a(\beta) = J_k(\beta) + \frac{A}{2} J_{k-1}(\beta) e^{i\phi} + \frac{A}{2} J_{k+1}(\beta) e^{-i\phi}. \quad (4.15)$$

For the calculation of the PDH error signal the Bessel functions $J_k(\beta)$ in equation (3.29) and (3.34) have to be substituted with $J_k^a(\beta)$, which leads to a modified error signal dependent of the amplitude and phase of the residual amplitude modulation. When the RAM signal is in phase with the PDH phase modulation, RAM leads to an offset in the error signal (Figure 4.5e). This offset is constant when the laser frequency is off resonance. When the carrier or the sidebands couple into the cavity, a part of the light is transmitted and the missing information at the detector in reflection leads to a smaller offset (Figure 4.5f). In the case of a perfectly mode and impedance matched cavity all light is transmitted at resonance and RAM causes no shift of the error signal zero crossing. When the RAM signal is out of phase, the error signal is only slightly modified in comparison to the error signal without RAM (Figures 4.5c and 4.5d). Thus, a changing RAM amplitude or RAM phase leads to offset shifts and thus to frequency fluctuations.

Pressure fluctuations

The resonant frequency of a cavity depends on the optical path length and thus not only on the distance of the mirrors but also on the refractive index of the material in between. Since high performance cavities are usually operated in vacuum the refractive index was treated as exactly one in the previous chapters of this thesis (equations (2.18) and (3.18)). Actually, the refractive index depends on the pressure with

$$n(p) = 1 + (n_0 - 1) \frac{p}{p_0}. \quad (4.16)$$

It follows that small pressure fluctuations changes the frequency according to

$$-\frac{\delta\nu}{\nu} = \frac{\delta n}{n} = \frac{1}{n} \frac{n_0 - 1}{p_0} \delta p \approx 3 \times 10^{-7} \frac{\delta p}{\text{mbar}}, \quad (4.17)$$

or

$$\frac{\delta\nu}{\delta p} = -84.6 \frac{\text{MHz}}{\text{mbar}}, \quad (4.18)$$

where $n_0 = 1.00029$ and $p_0 = 1013.25 \text{ mbar}$ has been used. Hence, it can be estimated that pressure fluctuations have to be below $3.5 \times 10^{-7} \text{ mbar}/\sqrt{\text{Hz}}$ to get resulting frequency fluctuations below $30 \text{ Hz}/\sqrt{\text{Hz}}$.

4.2.2. Effects influenced by the piezo actuator

This section presents effects that change the length of the cavity spacer. In the case of the piezo-tunable cavities, the Zerodur spacer plus the actuator (and adapters) form the cavity spacer. The properties of the piezo actuator thus have an influence on the sensitivity of the cavity to such effects as presented in the following.

Temperature fluctuations

Temperature fluctuations affect the stability of a cavity directly via the relation

$$\frac{\delta L}{L} = \alpha T. \quad (4.19)$$

The CTE α for typical cavity materials such as Zerodur is in the 10^{-8} 1/K range. Piezo materials show a higher coefficient as can be seen in Table 4.2. When considering the CTE of the assembled cavity, the individual coefficients have to be weighted with their corresponding length:

$$\alpha_{\text{cavity}} = \frac{\alpha_{\text{spacer}} L_{\text{spacer}} + \alpha_{\text{piezo}} L_{\text{piezo}}}{L_{\text{spacer}} + L_{\text{piezo}}}. \quad (4.20)$$

The effective CTE of the piezo-tunable cavities is thus between 10^{-7} 1/K and 10^{-6} 1/K. The exact calculated values are given in Table 4.5.

		PZT stack	PZT tube	PZN-PT	quartz	fixed
α_{cavity}	(10^{-6} /K)	0.35	-0.75	0.28*	1.2	0.02

Table 4.5.: Estimated thermal expansion coefficients of the cavities. The value of the cavity with PZN-PT actuator is not a calculated value but derived from own measurements (Section 5.2.3), since no information could be found in literature. For the calculation of the effective CTE of the assembled cavities the contribution of the adhesive was neglected.

Vibrations

A cylindrical cavity of length L which is compressed along its axis by gravity experiences a fractional length change of [59]

$$\frac{\Delta L}{L} = -\frac{\rho g L}{2E}, \quad (4.21)$$

where ρ is the mass density and E the Young's modulus. With this relation the vibration sensitivity of a cavity with a 10 cm long Zerodur spacer standing on one of its ends can be estimated to 4 MHz/g. With an incorporated 1 cm long PZT piezo actuator the sensitivity increases to 6 MHz/g. In the experiments carried out in this work, the cavities are mounted horizontally. In this case, gravity compresses the cavity diameter d and thus leads to an expansion of the cavity length suppressed by the Poisson ratio σ [59]

$$\frac{\Delta L}{L} = -\frac{\rho g d \sigma}{2E}. \quad (4.22)$$

A horizontally mounted cavity with a Zerodur spacer of 5 cm diameter would thus feature a vibration sensitivity of 470 kHz/g.

These simple models only roughly describe how the cavity length is affected by vibrations. The actual sensitivity depends strongly on the exact mounting of the cavity. Therefore several

4. Experimental Implementation

vibration insensitive cavity designs have been developed [22–24] using for example cut-outs of the spacer. To find out how the application of a piezo actuator changes the sensitivity to vibrations, the vibration sensitivity of the different piezo-tunable cavities when supported by a V-shaped mount was calculated with a finite element method using the program COMSOL Multiphysics. The results can be seen in Figure 4.6. The influence of the adhesive was neglected in the modelling. Even though there are big differences in the way the mirrors are deformed, all cavities show a displacement of about 2×10^{-10} m along the optical axis which corresponds to a vibration sensitivity of $v_{\text{cavity}} = \sim 500 \text{ kHz/g}$ (the exact values are given in Table 4.6). Thus, to reach the required frequency noise level of $30 \text{ Hz}/\sqrt{\text{Hz}}$, the seismic noise has to be below $6 \times 10^{-5} \text{ g}/\sqrt{\text{Hz}}$.

	PZT stack	PZT tube	PZN-PT	quartz	fixed
v_{cavity} (kHz/g)	553	369	487	513	564

Table 4.6.: Estimated vibration sensitivity derived from simulations.

Tilt fluctuations

A tilting of the cavity leads to deformation of the cavity due to changing gravitational forces. A cylindrical cavity whose optical axis is tilted against the horizontal by an angle of α changes its length according to (4.21) and (4.22) by

$$\frac{\Delta L}{L} = \frac{\gamma \rho L g}{E} \sin \alpha + \frac{\sigma \rho d g}{E} \cos \alpha. \quad (4.23)$$

γ accounts for the mounting conditions of the cavity. If the cavity is only fixed at one side ($\gamma = 1$), the cavity is fully stretched. If the cavity is symmetrically mounted in its center ($\gamma = 0$) the first term would vanish since the upper part of the cavity would be compressed to the same amount as the lower part is stretched.

For small variations of the tilt angle $\Delta\alpha$ with $\alpha + \Delta\alpha < 100 \mu\text{rad}$, (4.23) can be expressed by [54]

$$\frac{\Delta L}{L} = A \Delta\alpha + B \Delta\alpha^2 \quad (4.24)$$

with

$$A = \frac{\rho L g}{E} \left(\gamma - \frac{\eta d}{L} \alpha \right) \quad (4.25)$$

and

$$B = \frac{\eta \rho d g}{2E}. \quad (4.26)$$

When considering only small tilt angles the quadratic term B can be neglected. The composed tilt sensitivity for a cavity with incorporated piezo actuator is approximately the sum of the sensitivity of the two components, spacer and actuator:

$$A_{\text{cavity}} = A_{\text{spacer}} + A_{\text{piezo}}. \quad (4.27)$$

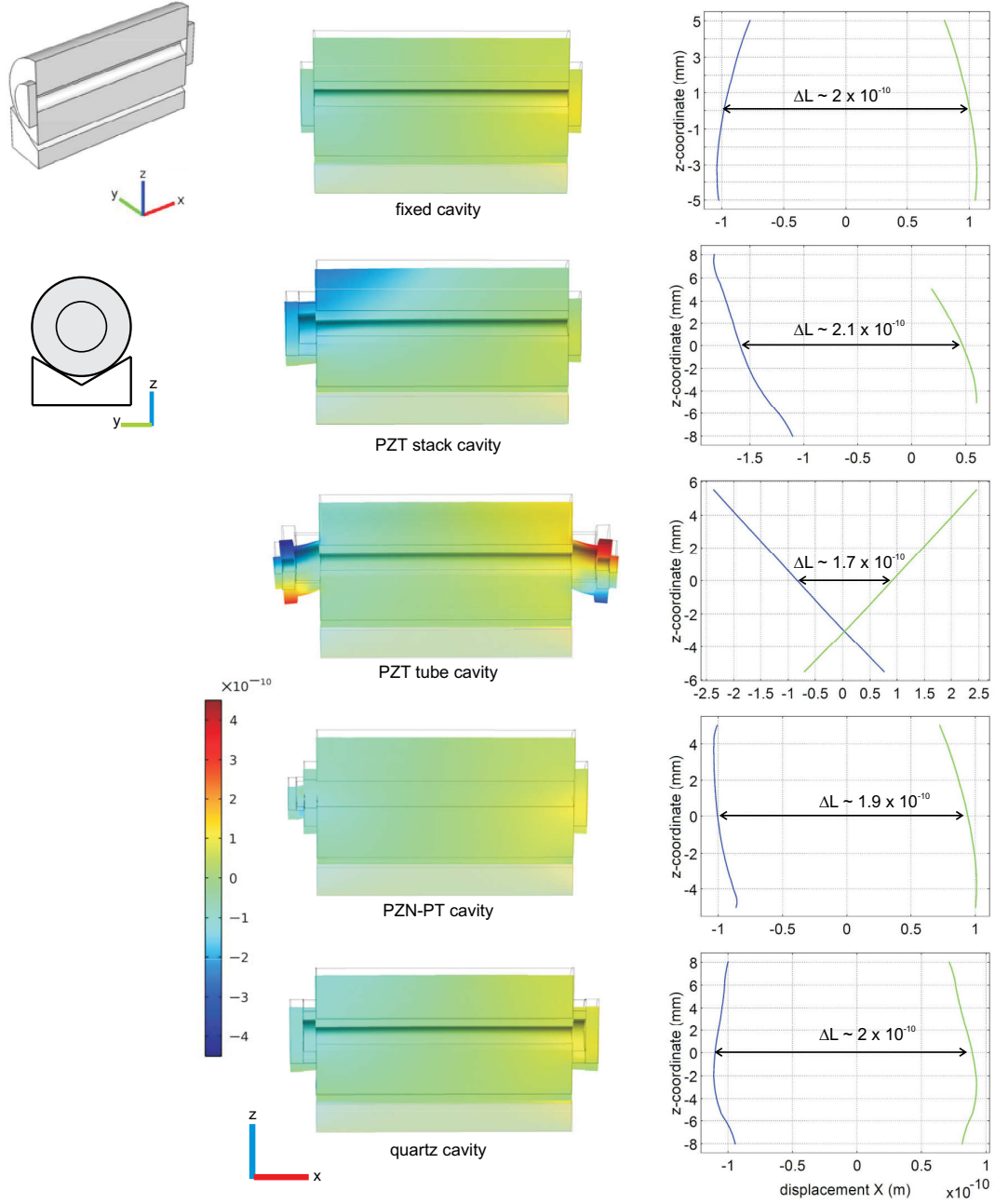


Figure 4.6.: Simulation of the cavity deformation due to gravity. In the simulations the cavities are supported by a V-mount as depicted by the two pictures on the upper left. The graphs in the center show the deformation of the cavity under the influence of a gravitation of 1g in z-direction. The colors indicate the displacement in x-direction, the mount is grayed out for clarity. The graphs on the right show the displacement of the cavity mirrors relative to their position without gravitational force. The beam with a radius of $\sim 250 \mu\text{m}$ is centered at about $z = 0$. The length change at this position is thus of interest for the vibration sensitivity.

4. Experimental Implementation

Assuming a non perfect symmetrical mounting with γ_{spacer} estimated to 0.1, the tilt sensitivity of the spacer can be calculated to $A_{\text{spacer}} = 2.76 \times 10^{-15} / \mu\text{rad}$ using $\alpha = 0 \mu\text{rad}$. In the case where only one piezo is mounted on one side the scale factor γ_{piezo} is 1; in the case of the symmetrically assembled double-sided version $\gamma_{\text{piezo}} = 0.1$ is estimated. Taking as example the cavity with PZT stack actuator, the sensitivity of the actuator is calculated to $A_{\text{piezo}} = 8.94 \times 10^{-15} / \mu\text{rad}$ (with $\gamma_{\text{piezo}} = 1$). The sensitivity of the whole cavity is thus $A_{\text{cavity}} = 1.17 \times 10^{-14} / \mu\text{rad}$. This corresponds to $3.3 \text{ Hz}/\mu\text{rad}$. For comparison, a cavity of the same length without piezo has a sensitivity of $830 \text{ mHz}/\mu\text{rad}$. The sensitivity of the other cavities is given in Table 4.7. It can be concluded that tilt fluctuations have to be below $9 \mu\text{rad}/\sqrt{\text{Hz}}$ to reach the required frequency stability.

		PZT stack	PZT tube	PZN-PT	quartz	fixed
A_{cavity}	(Hz/ μrad)	3.3	1.6	1.9	0.87	0.78

Table 4.7.: Estimated tilt sensitivities of the different cavities. The cavities with PZT tube actuator and quartz actuator have a lower sensitivity since they are approximately symmetrically assembled with two actuators. See main text for explanation.

Thermal noise

That thermal noise can affect the stability of a resonator, was first observed in gravitational wave detectors. Later it turned out that also compact rigid cavities can be limited by thermal noise. The theoretical description of this process was given by Numata *et al.* [60]; the displacement noise of cavity spacer $S_{x,S}$, mirror substrate $S_{x,M}$ and mirror coating $S_{x,C}$ at a frequency ω can be calculated using the following formulas:

$$S_{x,S}^2(\omega) = \frac{4k_B T}{\omega} \frac{L}{3\pi R^2 E} \phi_S, \quad (4.28)$$

$$S_{x,M}^2(\omega) = \frac{4k_B T}{\omega} \frac{1 - \sigma^2}{\sqrt{\pi} E w_0} \phi_M, \quad (4.29)$$

$$S_{x,C}^2(\omega) = \frac{4k_B T}{\omega} \frac{2d(1 + \sigma)(1 - 2\sigma)}{\pi E w_0^2} \phi_C. \quad (4.30)$$

L and R are the spacer length and radius, E is the Young modulus and σ the Poisson ratio. w_0 is the beam diameter at the mirror and d the coating thickness. The indices S , M and C denote the spacer, mirror substrate and coating. The piezo actuators are treated as spacer elements. Table 4.8 gives the calculated displacement noise contribution of each single cavity element. It can be seen that the PZT and PZN-PT actuators provide the highest noise contribution. Thus, the thermal noise limit of a cavity is increased when such an actuator is incorporated.

The displacement noise of the complete cavities is calculated by

$$S_x = \sqrt{S_{x,S}^2 + S_{x,\text{Piezo}}^2 + S_{x,M1}^2 + S_{x,M2}^2 + S_{x,C1}^2 + S_{x,C2}^2}. \quad (4.31)$$

4.2. Noise sources and environmental disturbances

	L (mm)	R (mm)	E (GPa)	Q	$S_x \cdot (1 \text{ Hz}/f)^{1/2}$ ($10^{-17} \text{ m}/\sqrt{\text{Hz}}$)
mirror (fused silica)			73	1 000 000	0.8 - 0.9
coating ($\text{Ta}_2\text{O}_5\text{--SiO}_2$)				2500	2.1 - 2.5
spacer (Zerodur)	100	25	90	3000	1.3
PZT stack	7	12.5	60	100	4.6
PZT tube	10	10	60	100	6.8
PZN-PT	3	6.5	63	100	5.6
quartz	5	12.5	76	200 000	0.08

Table 4.8.: The table shows the calculated displacement noise of the different cavity components as well as dimensions and material properties needed for calculation. The poisson ratio of the fused silica mirror substrates $\sigma = 0.17$ was used for calculation as well as a coating thickness of $d = 6 \mu\text{m}$. The exact mirror and coating thermal noise depends on the beam waist, which varies slightly due to the different lengths of the cavities (Table 4.4).

	L (mm)	$S_x \cdot (1 \text{ Hz}/f)^{1/2}$ ($10^{-17} \text{ m}/\sqrt{\text{Hz}}$)	$S_f \cdot (1 \text{ Hz}/f)^{1/2}$ ($\text{Hz}/\sqrt{\text{Hz}}$)	$\sigma(\tau)/\nu_0$ 10^{-16}
PZT stack	107	5.8	0.15	6.3
PZT tube	130	10.3	0.22	9.4
PZN-PT	110	6.8	0.17	7.3
quartz	110	3.7	0.10	4.0
fixed	100	3.8	0.11	4.5

Table 4.9.: Calculated thermal noise limit of the different cavities. L denotes the cavity length, S_x the displacement noise of the entire cavity, S_f the frequency noise, and σ the Allan deviation.

In the case of the PZT tube cavity and the quartz cavity, it is taken into account that these cavities are built with two piezo actuators. In the assembly of the PZN-PT and PZT tube cavity, adapter plates were used, whose thermal noise contribution was also calculated (but is negligible).

The calculated displacement noise is converted into frequency noise by

$$S_f = \frac{S_x}{L} \nu_0, \quad (4.32)$$

which is used to calculate the Allan variance

$$\sigma^2(\tau) = 2 \ln 2 \cdot S_f^2 f. \quad (4.33)$$

Since $S_f^2 \sim 1/f$, the Allan variance does not depend on f , which appears as a so called flicker floor in the Allan variance plot, typical for thermal noise. The calculated thermal noise limits of all applied cavities are shown in Table 4.9.

4. Experimental Implementation

4.2.3. Effects due to the piezo actuator - noise of piezo supply voltage

The application of a piezo actuator gives rise to a kind of noise not present in non-tunable cavity experiments, namely voltage noise. It is evident that noise in the voltage driving the piezo actuator may decrease the stability of the cavity and the corresponding laser frequency. This is expressed by the relation

$$\frac{\delta\nu}{\nu} = -\frac{\delta L}{L} = -\frac{d \cdot \delta U}{L}, \quad (4.34)$$

where d is the voltage to length conversion factor determined by the piezo-electric coefficient and U the piezo driving voltage. Frequency noise estimations can easily be done using the tuning coefficients listed in Table 4.1. A higher tuning coefficient requires a lower driving voltage to reach the same tuning range, but does also increase the sensitivity to voltage noise. In the case of the PZT stack cavity, for example, a voltage noise below $13 \text{ nV}/\sqrt{\text{Hz}} \times (1 \text{ Hz}/f)^{1/2}$ is required to reach thermal noise limited performance. To reach a frequency noise below the required $30 \text{ Hz}/\sqrt{\text{Hz}}$ down to Fourier frequencies of 3 mHz a voltage noise below $150 \text{ nV}/\sqrt{\text{Hz}} \times (1 \text{ Hz}/f)^{1/2}$ would be necessary. These are challenging specifications, especially in the low frequency range. Therefore a closer look on noise processes in electronic devices, especially in amplifiers will be given in the following.

Noise processes in electronic devices

Noise in electronic devices is caused by different noise processes. The most important of them are shortly described in the following. Note that for the description of voltage and current noise the spectral density notation is used.

Johnson noise Johnson noise is thermal noise in electronic devices arising from the thermal motion of charge carriers. The voltage noise v_n at a temperature T is given by

$$v_n = \sqrt{4kTR}, \quad (4.35)$$

where k is the Boltzman constant and R the resistance of the electronic device. To give an example, the Johnson noise of a $10 \text{ k}\Omega$ resistor at room temperature is $13 \text{ nV}/\sqrt{\text{Hz}}$. Johnson noise has a flat frequency spectrum and is thus a white noise process.

Shot noise Electric current is a flow of discrete electric charges which shows statistical fluctuations. The resulting current noise is given by

$$i_n = \sqrt{2eI}, \quad (4.36)$$

where e is the electron charge and I the average DC current. For example, the shot noise of a 1 mA current is $18 \text{ pA}/\sqrt{\text{Hz}}$. Thus the voltage drop over a 10 kHz resistor is $180 \text{ nV}/\sqrt{\text{Hz}}$. Shot noise does only occur in the presence of a current flow, it is independent of temperature and like Johnson noise it has a flat frequency spectrum.

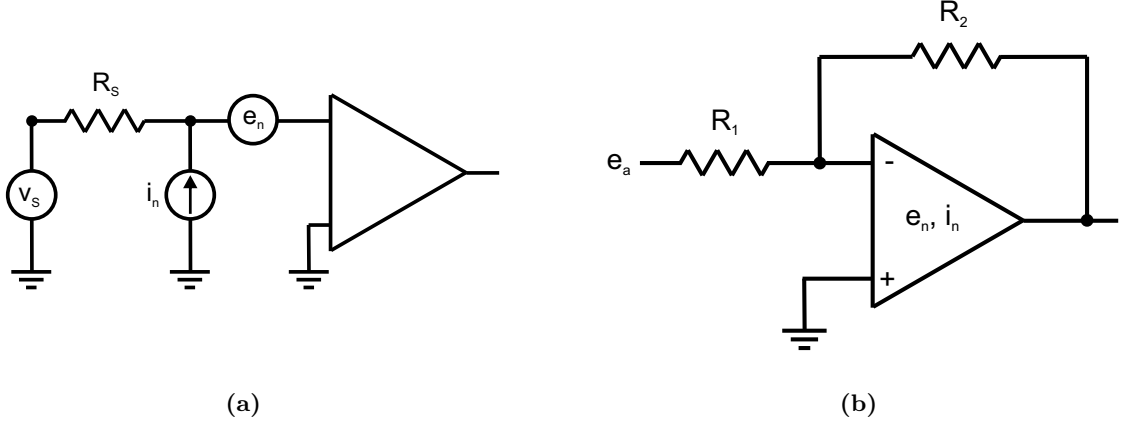


Figure 4.7.: Left: amplifier noise model. In this model, the amplifier is assumed noiseless. e_n represents a noise voltage source in series with the input voltage v_s from a source with resistance R_s . i_n represents an input noise current. Right: amplifier with feedback. The equivalent source noise e_A depends on the applied resistors as specified in (4.37). Based on [62].

Flicker noise Flicker noise has a $1/f$ spectrum and is therefore the dominating noise in the low frequency range. There are multiple effects which can cause electronic flicker noise like resistance fluctuations or base current noise in transistors. Flicker noise is associated with a DC current in electronic devices and unlike Johnson and shot noise it depends on the material choice and processing.

Noise in operational amplifiers

A voltage source consists mainly of a voltage reference and amplifiers. The behavior of voltage references in the LISA frequency range has been studied by Fleddermann *et al.* [61]. The best such references can reach a relative noise level of less than $10^{-6}/\sqrt{\text{Hz}}$ at 0.1 mHz. A detailed investigation of the noise properties of operational amplifiers in the low frequency range could not be found in the literature.

In a simple noise model, an amplifier can be characterized by its equivalent input voltage noise e_n and input current noise i_n (Figure 4.7a). They comprise all noise processes in the amplifier, which are mainly those described above. Thus, their noise figure is white in the high frequency range until at a specific corner frequency f_c 1/f-noise starts to rise.

The noise of an amplifier with feedback (Figure 4.7b) is the sum of the equivalent input voltage noise, the Johnson noise of the applied resistors, and the voltage noise generated by the equivalent input current noise across the resistors. The equivalent source noise can be calculated by [62]

$$e_A^2 = e_n^2 + 4kT \frac{R_1 R_2}{R_1 + R_2} + (i_n \frac{R_1 R_2}{R_1 + R_2})^2. \quad (4.37)$$

4. Experimental Implementation

Taking the example of an OP27G amplifier (Analog Devices), $e_n = 3.8 \text{ nV}/\sqrt{\text{Hz}}$ and $i_n = 1.7 \text{ pA}/\sqrt{\text{Hz}}$ are specified in the high frequency range, where voltage and current input noise are dominated by white noise. With $R_1 = 1 \text{ k}\Omega$ and $R_2 = 10 \text{ k}\Omega$ this results in an equivalent input noise of $5.7 \text{ nV}/\sqrt{\text{Hz}}$ or an output noise of $57 \text{ nV}/\sqrt{\text{Hz}}$. The actual output noise of an amplifier in feedback depends thus on its equivalent input noise, the choice of resistors and the amplification factor. In addition to this intrinsic noise the output voltage can vary due to fluctuations in the supply voltage or temperature fluctuations. For an OP27 amplifier the temperature coefficient is specified as $0.4 \mu\text{V}/\text{K}$ and the power supply rejection as 118 dB. A fluctuation of a 15 V supply voltage by 0.1 %, e.g., would result in voltage fluctuations of $20 \text{ nV}/\sqrt{\text{Hz}}$ at the amplifier output.

This example illustrates that a careful design of the electronic circuit driving the piezo actuator is necessary. When using a high voltage amplifier which is required to tune the cavity more than one FSR, this task gets even more challenging.

4.2.4. Summary

Table 4.10 summarizes some cavity properties and sensitivities to external effects. Note that some differences in sensitivity arise from the difference in cavity length or are affected by it. Thus, the table does not give a general comparison of the influence of the different piezo actuators when incorporated in a cavity, but a comparison of the particular cavities built here.

		PZT stack	PZT tube	PZN-PT	quartz	fixed
cavity length L_C	(mm)	107	130	110	110	100
FSR	(GHz)	1.4	1.15	1.30	1.36	1.50
tuning coefficient $\Delta\nu/U$	(MHz/V)	7.5	12	2.2	0.012	-
maximum tuning range $\Delta\nu_{max}$	(GHz)	9	14.4	2.64	0.014	-
sensitivity to intensity fluctuations	(Hz/W)	771	635	750	750	825
sensitivity to pressure fluctuations	(MHz/mbar)	84.6	84.6	84.6	84.6	84.6
cavity CTE α_{cavity}	($10^{-6}/\text{K}$)	0.35	-0.75	-	1.2	0.02
vibration sensitivity	(kHz/g)	553	369	487	513	564
tilt sensitivity	(Hz/ μrad)	3.3	1.6	1.9	0.87	0.78
thermal noise S_{TN} @ 1 Hz	(Hz/ $\sqrt{\text{Hz}}$)	0.15	0.22	0.17	0.10	0.11
thermal noise σ_{tn}/ν_0	$\times 10^{-16}$	6.3	9.4	7.3	4.0	4.5

Table 4.10.: Summary of the calculated cavity properties and sensitivities. The maximum tuning range $\Delta\nu_{max}$ is calculated under the condition that voltages from -200 V to $+1000 \text{ V}$ can be applied to the actuators.

4.3. Test setup

As indicated by the previous considerations on possible noise sources and disturbances, the LISA requirements on the frequency stability demand a carefully designed test environment for the tunable cavities. With respect to the low frequency LISA measurement band, especially temperature effects have to be regarded. But also other ambient effects like vibrations have to be considered and an appropriate optical system has to be designed.

A picture of the main part of the experimental setup can be seen in Figure 4.8. It shows the cavity with PZT actuator and the fixed cavity surrounded by two thermal shields in a vacuum chamber together with the incoupling optics and detectors for performing the PDH lock. In the following a detailed description of all the subsystems will be given.

The experimental setup had to be moved to another laboratory during the measurement phase. The laboratories differ, however, only slightly in their vibrational and thermal environment and the setup stayed almost unchanged. Most of the measurements were carried out in the new laboratory, so all following descriptions are related to this laboratory, if not otherwise noted.

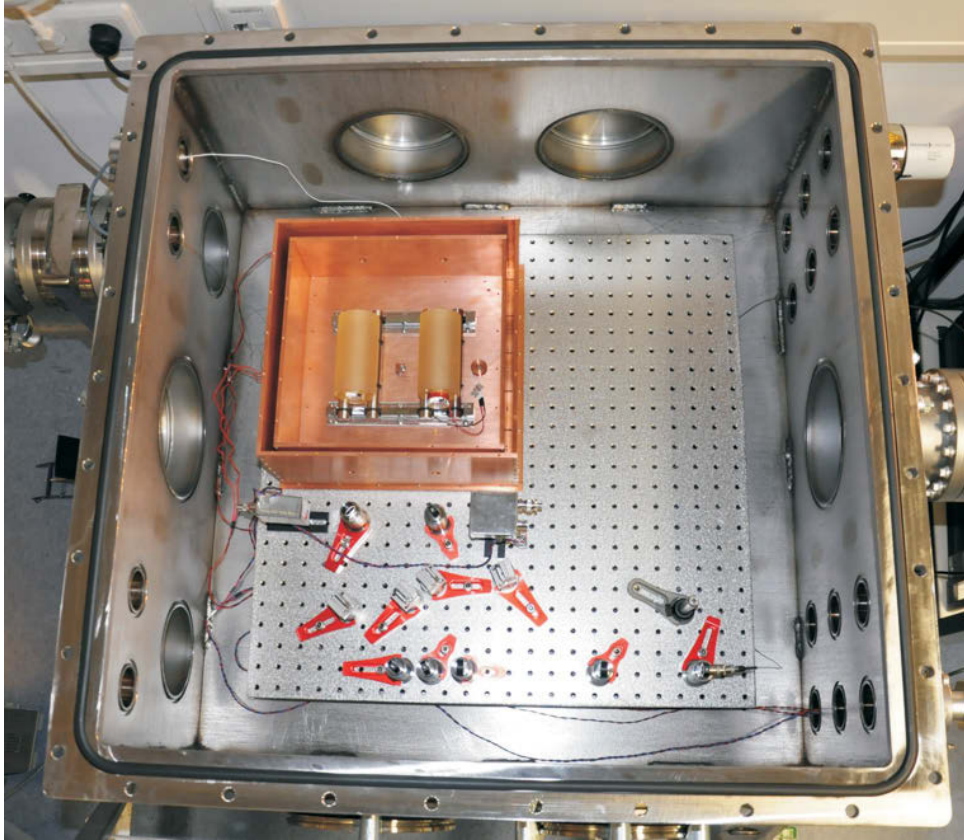


Figure 4.8.: Photograph of the cavities mounted inside the thermal shields in the vacuum chamber (without top cover). The optics for coupling in the cavities and the detectors for performing the PDH are installed in the vacuum chamber as well.

4. Experimental Implementation

4.3.1. Test environment

Vacuum system

Since the resonance frequencies of the cavities varies with pressure changes, the cavities are housed inside a vacuum chamber. Vacuum conditions are also useful to achieve a good thermal stability, since thermal transport due to convection depends on the particle density. Convection can be neglected if the mean free path of the particles is large compared to the dimension of the vacuum chamber. The mean free path Λ is calculated from the particle density n and the scattering cross section σ by

$$\Lambda = \frac{1}{n\sigma}. \quad (4.38)$$

The scattering cross section of nitrogen is $\sigma = 45 \times 10^{-16} \text{ cm}^2$ and the particle density can be derived from the ideal gas law by

$$n = \frac{N}{V} = \frac{p}{kT}, \quad (4.39)$$

where $k = 1.38 \times 10^{-23} \text{ J/K}$ is the Boltzmann constant and T the temperature.

The vacuum chamber was designed to not only house the cavities but also other tunable references for LISA or future experiments. For this purpose the chamber has a relatively large inner volume with dimensions of $762 \times 762 \times 335 \text{ mm}^3$ and in total 18 vacuum flanges to allow flexibility for the mounting of different vacuum feedthroughs, windows, valves and pumps. The chamber is covered by a 60 mm plexiglass plate, which allows to look inside the chamber during vacuum operation.

The chamber is evacuated with a XDS5 Scrollpump from Edwards and a Turbovac 361 from Oerlikon Leybold Vacuum with 3501/s pumping speed. With this pumping system a final pressure of $1 \times 10^{-6} \text{ mbar}$ can be achieved, which should be low enough to avoid frequency fluctuations due to pressure fluctuations. The mean free path at this pressure is $\sim 100 \text{ m}$ and thus clearly larger than the vacuum chamber dimensions.

Thermal environment

The cavities are situated inside two copper shields to suppress ambient temperature fluctuations. The inner and the outer shield are separated by four small Viton O-rings (inner diameter 5 mm, thickness 5 mm) and fixed in position with four 2 mm steel screws. The dimensions are chosen such that heat transfer is dominated by thermal radiation as described later. The outer shield is equipped with heating foil which gives the opportunity for temperature ramping or stabilization. The inner space available to the cavity setup is $250 \times 250 \times 105 \text{ mm}^3$.

Heat transfer processes The heat transfer between the two thermal shields is given by thermal radiation and thermal conduction through the Viton O-rings and the steel screws. Convection can be neglected due to the high vacuum conditions. The thermal radiation between two plates of size A with temperatures T_1 and T_2 can be calculated by [63]

$$\dot{Q}_r = \sigma A \epsilon_{12} (T_1^4 - T_2^4), \quad \text{with } \epsilon_{12} = \frac{\epsilon_1 \epsilon_2}{\epsilon_1 + \epsilon_2 - \epsilon_1 \epsilon_2}, \quad (4.40)$$

where $\sigma = 5.67 \times 10^{-8} \frac{\text{W}}{\text{m}^2\text{K}^4}$ is the Stefan-Boltzmann constant and ϵ_1 and ϵ_2 are the emissivities of the two plates.

Thermal conduction through a bar of length L and cross-section A_{CS} which is connected at one side to a temperature T_1 and at the other side to a temperature T_2 is given by

$$\dot{Q}_c = \lambda A_{\text{CS}} \frac{T_1 - T_2}{L}, \quad (4.41)$$

where λ is the thermal conductivity of the material. The thermal conduction through the O-rings and the screws can thus be written as

$$\dot{Q}_c = (\lambda_O A_O + \lambda_S A_S) \frac{T_1 - T_2}{L}, \quad (4.42)$$

where A_O and A_S are the cross sections of the O-rings and screws and λ_O and λ_S the respective thermal conductivities.

For small temperature differences between the two thermal shields ($T_1 = T_2 + \delta T$), equation (4.40) can be approximated to

$$\dot{Q}_r = \sigma A \epsilon_{12} (4T_2^3 \delta T) = \dot{q} \delta T. \quad (4.43)$$

Hence, the ratio between radiation and conduction can be calculated to

$$\frac{\dot{Q}_r}{\dot{Q}_c} = \frac{L}{\lambda_O A_O + \lambda_S A_S} \sigma A \epsilon_{12} 4T_2^3 \approx 5. \quad (4.44)$$

For the calculation $A = 0.3 \text{ m}^2$, $\lambda_O = 0.226 \frac{\text{W}}{\text{mK}}$, $\lambda_S = 15 \frac{\text{W}}{\text{mK}}$, $A_O = 157 \text{ mm}^2$, $A_S = 7 \text{ mm}^2$, $L = 5 \text{ mm}$, $\epsilon_1 = \epsilon_2 = 0.1$, and $T_2 = 300 \text{ K}$ were used. Thus, with the chosen dimension of O-rings and screws and for small temperature deviations, thermal radiation dominates over thermal conduction. In this way, the inner shield has a homogeneous temperature distribution and temperature gradients can be neglected.

The model of two radiating plates fits well for radiation processes between the two shields. For describing the radiation process between the big vacuum chamber (surface A_2) and the outer shield (surface $A_1 \ll A_2$) the approximation of a body in an enclosed room is better suited [63]:

$$\dot{Q}'_r = \sigma A_1 \epsilon'_{12} (T_1^4 - T_2^4), \quad \text{with } \frac{1}{\epsilon'_{12}} = \frac{1}{\epsilon_1} + \left(\frac{1}{\epsilon_2} - 1\right) \frac{A_1}{A_2} \approx \frac{1}{\epsilon_1} \text{ for } A_1 \ll A_2. \quad (4.45)$$

With this approximation the ratio between radiation and conduction (4.44) for heat transfer from the vacuum chamber to the outer shield can be calculated to ~ 30 .

Thermal low-pass filter The thermal shields can be considered as thermal low-pass filters. In analogy to an electrical filter, their time constants can be calculated with the thermal capacity and the thermal resistance. The resistance is the inverse of the thermal conduction per Kelvin or, in this case, of the thermal radiation per Kelvin. The thermal capacity C_{th} can be calculated

4. Experimental Implementation

with the specific heat c and the mass of the respective shield: $C_{\text{th}} = c \cdot m$. It follows

$$\tau_1 = \frac{C_{\text{th}}}{\dot{q}} = \frac{c_{\text{CU}} \cdot m_i}{\sigma \epsilon_{12} A 4 T^3} \approx 50\,000 \text{ s} \quad (4.46)$$

$$\tau_2 = \frac{C'_{\text{th}}}{\dot{q}'} = \frac{c_{\text{CU}} \cdot m_o}{\sigma \epsilon'_{12} A 4 T^3} \approx 34\,000 \text{ s}, \quad (4.47)$$

with $c_{\text{CU}} = 385 \text{ J/(kgK)}$ being the specific heat of copper, $m_i = 12 \text{ kg}$ the mass of the inner shield, and $m_o = 16.6 \text{ kg}$ the mass of the outer shield.

The transfer function of two RC low-pass filters in series has two corner frequencies, which are the cutoff frequencies of the individual RC filters. The output voltage rolls off at the lower frequency with 20 dB per decade and at the higher frequency with 40 dB per decade. If the two RC filters have the same cutoff frequencies, the two filters in series act approximately as a second order low-pass filter. Thus, the two thermal shields in series, which have roughly the same time constant, can also be considered as a second order low-pass filter. In addition, the heat transfer between the inner shield and the cavities acts as third low-pass filter.

Experimental validation The vacuum chamber and the two thermal shields are equipped with temperature sensors (PT 100) to measure the influence of a varying temperature. The laboratory temperature has a 24 h modulation due to a varying outdoor temperature which can be suppressed by the air conditioning system to approximately $\pm 0.2 \text{ K}$. The time record of the temperature measured with the three temperature sensors over 14 days is shown in Figure 4.9a. A 24 h modulation as well as a weekly period is visible.

To determine the filter properties of the thermal shields, the data measured outside the vacuum chamber were processed with a first-order low-pass filter using Matlab and compared with the temperature data measured at the outer shield (Figure 4.9b). The same was done with the outer shield and the inner shield (Figure 4.9c). The such determined time constants $\tau_1 = 53\,000 \text{ s} \approx 15 \text{ h}$ and $\tau_2 = 32\,000 \text{ s} \approx 9 \text{ h}$ do agree very well with the calculations ((4.46) and (4.47)). The time constant of the heat transfer from the inner shield to the cavities was identified with the same method to be $\tau_3 = 12\,000 \text{ s} \approx 3 \text{ h}$ (Figure 4.9d). The temperature of the cavity was not directly measured but determined with the measured frequency and the CTE of the cavity.

By successively applying low-pass filters with the identified time constants to the lab temperature measurement, the temperature stability at the shields and at the cavity was calculated. Figure 4.9e shows the spectral density of the calculated temperature noise as well as the measured temperature noise. It can be seen that over almost the whole spectral range, the temperature measurements are limited by the measurement sensitivity. Thus, only in the frequency range below $\sim 1 \times 10^{-4} \text{ Hz}$ the calculations match with the measurements.

The calculated temperature noise at the cavity is scaled with the highest CTE, which is $1.1 \times 10^{-6} \text{ 1/K}$ for the cavity with the quartz actuator, and converted to frequency noise using $\delta\nu = \alpha \delta T \nu$ (Figure 4.9f). It can be seen, that even with the cavity with the highest CTE, the passive temperature stability of the setup is sufficient to fulfill the requirements above a Fourier frequency of $5 \times 10^{-5} \text{ Hz}$.

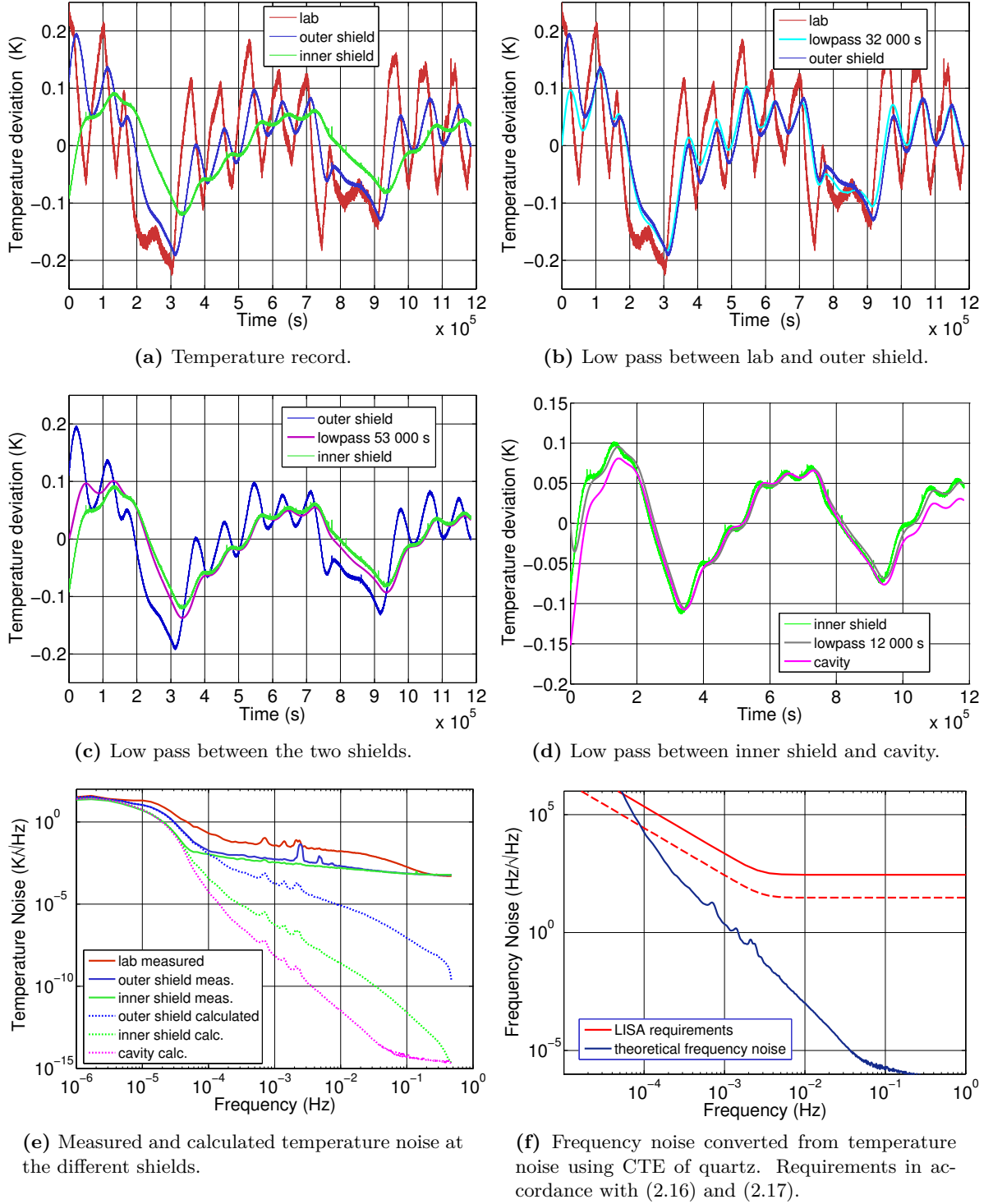


Figure 4.9.: Temperature stability on the thermal shields acting as thermal low passes.

4. Experimental Implementation

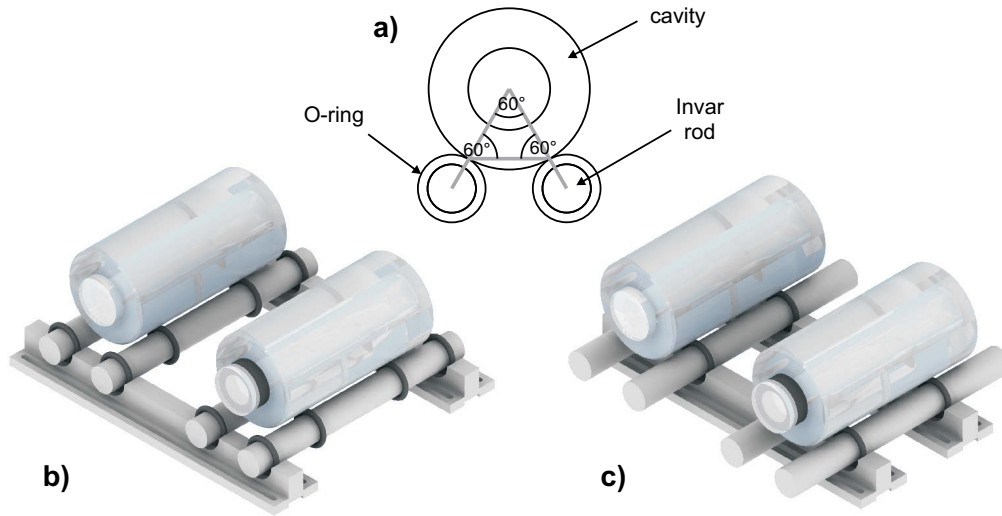


Figure 4.10.: Mounting of the cavities. (a) shows the alignment of the supporting points vertical to the optical axis. The alignment along the optical axis can be seen in (b) in the older version and in (c) in the newer version.

Mounting of the cavities and vibration isolation

To reduce the influence of vibrations, the cavities are supported in their Airy points [64]. The Airy points are characterized by the fact that a rod which is supported in its Airy points is bended by gravitational forces such that the end faces stay parallel. Thus, a length change of the cavity due to vibrations is suppressed. A cylindric cavity mounted in its Airy points should have the same vibration sensitivity as a cavity mounted on a V-shaped mount [65]. In the case of the 10 cm long Zerodur cylinder the Airy points are at a distance of 2.213 cm from the end faces. Respectively two Viton O-rings are placed in this distance in such a way that the supporting points form an equilateral triangle together with the resonator axis (Figure 4.10a). The O-rings are arranged around 140 cm long Invar rods, which are supported on O-rings as well; in the old laboratory at a distance of 120 cm (Figure 4.10b). In the new laboratory, the O-rings supporting the cavities were also taken for supporting the Invar rods (Figure 4.10c). The reason for this modification was, that the Invar rods were not supported in their Airy points or - here of greater interest - not in their Bessel points. The Bessel points differ only slightly from the Airy points and are characterized by the fact that the overall bending of a rod which is supported in its Bessel points gets minimal. It was expected that in the first configuration, vibrations cause a displacement of the cavity supporting points and consequently a displacement of the cavity axis. A displacement of the cavity axis with respect to the incoupling laser beam can lead to a frequency change, and was thus tried to avoid.

To suppress vibrations the vacuum chamber is mounted on four pneumatic vibration isolators (Newport, PL 2000) as they are used for optical tables. As can be seen in Figure 4.11, they show a suppressing effect above ~ 3 Hz, while for low frequencies a slight increase of the noise level is visible. The applied isolators suppress the seismic noise in the whole frequency range below the required $6 \times 10^{-5} \text{ g}/\sqrt{\text{Hz}}$ and are thus suitable for the test setup.

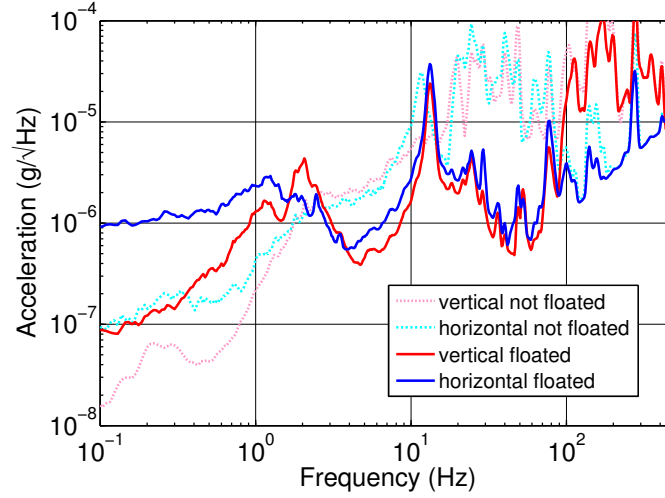


Figure 4.11.: Seismic noise measured with a CMG-40 seismometer from Güralp Systems on top of the vacuum chamber. Shown is the comparison of the horizontal and vertical vibrations with pneumatic isolators either floated or not floated.

4.3.2. Read-out, stabilization and measurement

Optical system

Two Nd:YAG non-planar ring oscillator (NPRO) lasers at 1064 nm were used as light sources. The employed models LW122 and LW124 from Lightwave Electronics Inc. have a small free running linewidth of 10 kHz at 1 ms. The laser frequency can be tuned slowly over several GHz by changing the Nd:YAG crystal temperature. Fast tuning of several MHz is possible with a piezo attached to the crystal. This piezo is also used for the frequency modulation for the PDH lock. As modulation frequencies 444 kHz (LW122) and 1.8 MHz (LW124) are chosen, since the lasers show low RAM at these frequencies. The modulation frequencies are provided by HP 33120A function generators from Hewlett Packard.

The laser light is overlapped and then guided into the vacuum chamber by a polarization maintaining, single mode fiber which is also used for mode cleaning (Figure 4.12). In the chamber, the thermal shields with the resonators and all the incoupling optics are located on a vacuum compatible optical bread board. The beam is mode matched with two lenses to the TEM₀₀ mode of the cavity, split, and coupled with two adjustable mirrors to the cavity mode. Using a PBS and a quarter wave plate in front of the cavity, the back reflected light is guided to a detector used for the PDH lock. The laser light is attenuated such that $\sim 20 \mu\text{W}$ impinge on the cavity. The light transmitted through the cavity in resonance is dumped.

All optical elements are mounted in highly stable mirror mounts on 1 inch steel pedestals to ensure high mechanical stability of the incoupling optics. Since the optics is placed inside the vacuum chamber, they are also shielded against air flows and thermal influences. Optical components such as lenses and polarizers have an anti-reflection coating and, if possible, are slightly tilted relative to the beam path to avoid parasitic resonators.

4. Experimental Implementation

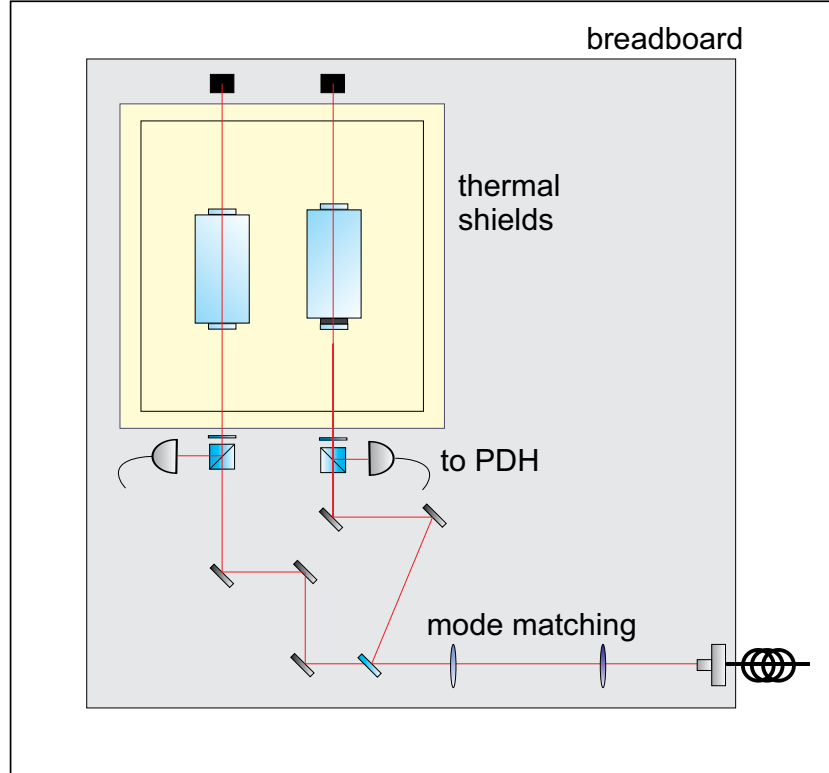


Figure 4.12.: Schematic of the optical setup inside the vacuum chamber. After the fiber coupler two lenses are used for mode matching. A 50:50 beam splitter directs the light to both resonators. A pair of mirrors is used in each case to couple to the cavity mode and a PBS and a quarter wave plate to direct the reflected light to the photo detector.

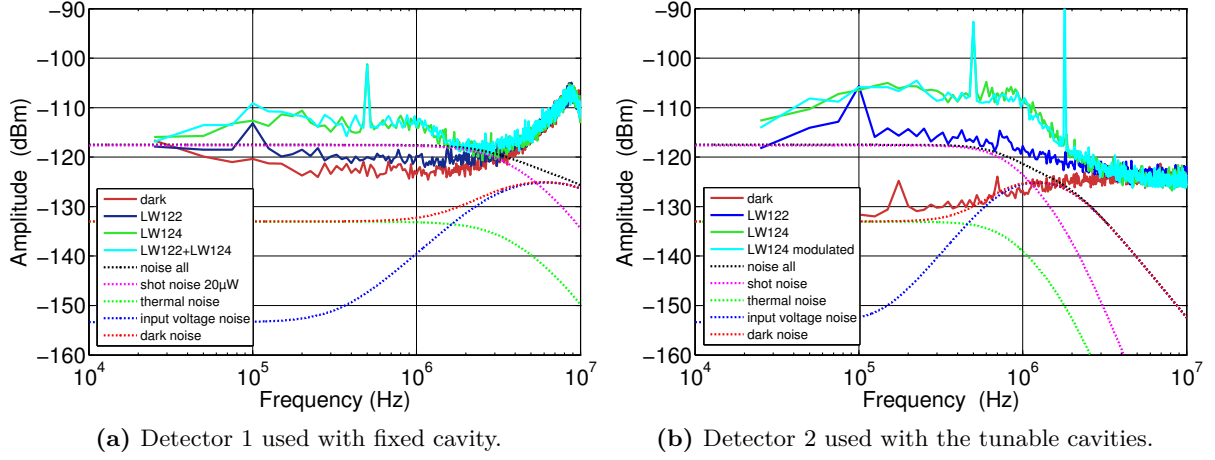


Figure 4.13.: Performance of the PDH detectors. The dashed lines depict calculated noise levels, the solid line measured noise. Calculations and measurements were performed with a laser intensity of 20 μ W. During the measurements with detector 2, laser LW124 was modulated.

Detection and signal processing

The light reflected from the cavity is detected by a self-built shot noise limited photo detector with a bandwidth of 10 MHz. The detector design was developed by S. Grede [66] for the detection system in an atom interferometer and adopted for this purpose. The detector works with an InGaAs Pin photodiode (Hamamatsu, G8376-05) and a transimpedance amplifier which is assembled in such a way that the 20 μ W impinging the detector are amplified to 1.5 V.

Figure 4.13 shows the theoretical detection noise limit and the measured detector noise of the two used photo detectors. Detector 2 shows shot noise limited performance. Detector 1, which is used for the the PDH lock of the fixed cavity has a resonance at 9 MHz and an about 10 dB increased dark noise in comparison to the theoretical noise. The shot noise is only slightly above the dark noise, which leads to a non-optimal signal to noise ratio. However, this detector was not further optimized, since the overall performance of the stabilized laser system was not limited by the detector performance. Furthermore it can be seen that the LW124 laser has a considerably higher technical noise than the LW122.

The so detected signal is amplified with ZFL500LN amplifiers from Mini-Circuits and a ZFM3 Mixer from Mini-Circuits is used to demodulate the signal with the modulation frequency. The resulting error signal is low pass filtered and fed to a self-built lock-box. There, the error signal is provided via a PI controller to the piezo attached at the laser crystal. An additional integrator transmits the error signal to the crystal temperature to adjust slow but bigger changes.

Beat measurement and frequency references

The actual measurement is done by performing a beat measurement between the laser stabilized to the tunable cavity and an even more stable laser. Therefore, a fraction of the laser light is overlapped with the stable laser and detected with a fast photodiode (New Focus, 1537, 6 GHz).

4. Experimental Implementation

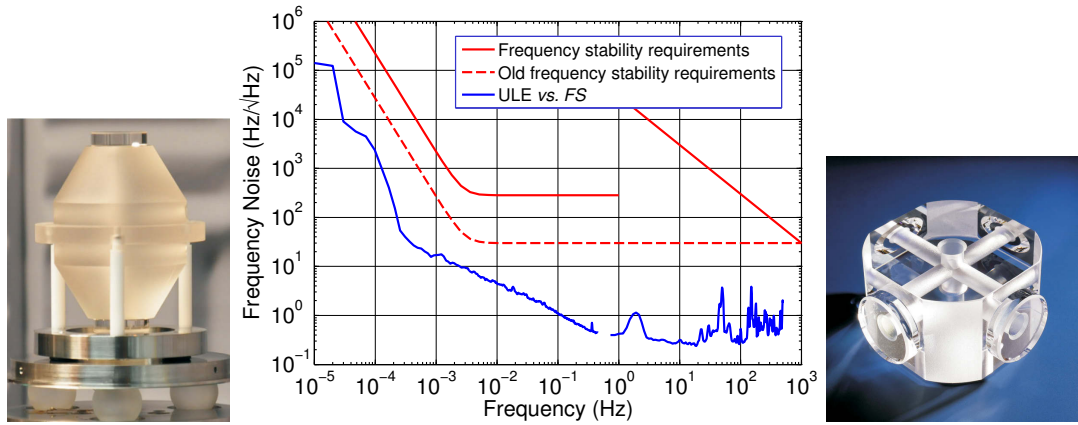


Figure 4.14.: Left: 7.75 cm long ULE glass cavity. Right: 5.5 cm long fused silica cavity, photograph courtesy E. Fessler. Center: Noise spectrum of a beat measurement between two laser stabilized to these cavities.

By selecting a convenient TEM_{00} mode of the cavity, the beat frequency can be chosen < 1 GHz. This frequency is amplified with Mini-Circuits ZFL1000LN amplifiers and mixed down with a ZFM3 from Mini-Circuits using a synthesizer (Rhode&Schwarz, 845.4002.52) as local oscillator. The so obtained frequency (< 200 MHz) is either counted with a SR620 from Stanford Research Systems or with a CNT-90 from Pendulum. Local oscillator and counter are phase locked to a 10 MHz reference provided by a GPS signal.

The reference laser for the beat measurement is stabilized to an ULE cavity (shown in Figure 4.14 on the left). This 7.75 cm long cavity is midplane mounted to suppress vibrations [67] and is temperature stabilized to the turning point of its CTE at room temperature [68]. As a second frequency reference a 5.5 cm long fused silica (FS) resonator is available (Figure 4.14 on the right). This resonator was used in a Lorentz invariance test [69] and has a very good passive thermal insulation. The frequency noise determined from a beat measured between two lasers stabilized to these cavities is shown in Figure 4.14 in the center. The noise is well below the LISA requirements concerning the frequency noise of a tunable pre-stabilization. Thus both references are suitable as frequency reference for a tunable cavity.

5. Characterization of the Piezo-Tunable Cavities

This chapter presents the measurements which were carried out for characterization of the piezo-tunable cavities. For these measurements, the tunable cavities were placed one after another in the test setup, described in the previous chapter. After examining some cavity properties such as FSR or Finesse, the frequency noise of the cavities with short circuited piezo actuators is presented and compared with the LISA requirements for a tunable pre-stabilization. Various influences affecting the frequency stability of the cavities are discussed. Then, the behavior of the cavities with applied voltage is examined including typical piezo characteristics such as hysteresis. Finally, the integration of a piezo-tunable cavity in an external feedback loop is demonstrated.

5.1. Cavity properties

To characterize the cavities some typical cavity properties such as FSR or Finesse have been measured (Table 5.1). The following provides a description on how the different properties were measured or how they were derived from measured values.

Free spectral range and cavity length The free spectral range of the cavities was measured by locking two lasers to two adjacent longitudinal cavity modes and measuring the beat frequency between the two lasers. With the measured FSR the length of the cavities can be calculated using $L = c / (2 \text{FSR})$.

cavity	FSR (GHz)	L_C (mm)	Finesse	Γ_ν (kHz)	coupling efficiency	cavity losses (ppm)
PZT stack	1.397	107.315	38 000	37	20%	147
PZT tube	1.146	130.845	191 000	6	80%	15
PZN-PT	1.358	110.367	34 000	40	18%	168
quartz	1.36	110	106 000	13	50%	42
fixed	1.5	100	47 000	32	25%	117

Table 5.1.: Properties of the different piezo-tunable cavities and the optically contacted fixed cavity. L_C is the cavity length and Γ_ν the linewidth of the cavity resonance. The gray values are not derived from measurement. The cavity length is in this case taken from manufacturer specifications and used to calculate the FSR.

5. Characterization of the Piezo-Tunable Cavities

Coupling efficiency To measure the coupling efficiency of the cavities, the DC signal from the detector in reflection was observed while ramping the unmodulated laser frequency slowly over the resonance. Off resonance the laser light is totally reflected generating a DC signal V_0 at the detector. In resonance a part of the light is transmitted through the cavity leading to a dip in the observed signal. The depth of the dip in relation to the off resonance signal V_0 gives the coupling efficiency $CE = (V_0 - V_{\text{res}})/V_0$. For a perfectly mode matched cavity the coupling efficiency is directly connected with the cavity reflectivity R_C (equation (3.16)) over $R_C = 1 - CE$. The reflectivity of a perfectly impedance matched cavity should be zero at resonance.

Cavity resonance linewidth and finesse To measure the linewidth of the cavity resonance, the laser frequency has to be ramped slowly over the cavity resonance. The width of the dip in the reflected signal corresponds to the cavity resonance linewidth. Since the cavity resonance has a relatively high drift, an offset phase lock was applied to realize the slow ramping. A first laser was locked to a cavity resonance and a second laser was phase locked to the first laser. The phase lock was implemented such that the second laser has an offset of one FSR. By slowly sweeping the offset frequency the laser can be tuned over the cavity resonance. The DC signal of the detector in reflection was recorded and the linewidth of the cavity resonance was estimated by comparing the width of the dip with the sweep amplitude.

The Finesse \mathcal{F} of the cavity can be determined from the cavity resonance linewidth using

$$\mathcal{F} = \text{FSR}/\Gamma_\nu. \quad (5.1)$$

For the cavity with PZT stack actuator and the cavity with quartz actuator no direct linewidth measurement was performed and the finesse was calculated from the cavity reflectivity. With equation (3.16) and the mirror transmission $T = 8.7 \times 10^{-6}$ (value taken from manufacturer measurements) the finesse of the cavity can be determined to

$$\mathcal{F} = \frac{\pi}{T}(1 - \sqrt{R_C}). \quad (5.2)$$

This also allows to calculate the cavity resonance linewidth from the cavity reflectivity

$$\Gamma_\nu = \frac{\text{FSR}}{\pi} \frac{T}{1 - \sqrt{R_C}}. \quad (5.3)$$

The such calculated cavity resonance linewidths differ from the directly measured linewidths by less than 4%. This proves that the setup has a very good mode matching and that the cavity reflectivity is thus only influenced by cavity properties.

Cavity losses The different coupling efficiencies and finesse of the investigated cavities can be explained by different degrees of pollution of the cavity mirrors. During the bonding process the mirrors could get slightly polluted which leads to increased cavity losses. Equation (3.15) gives the relation between cavity finesse \mathcal{F} and cavity losses A

$$\mathcal{F} = \frac{2\pi}{2T + A}. \quad (5.4)$$

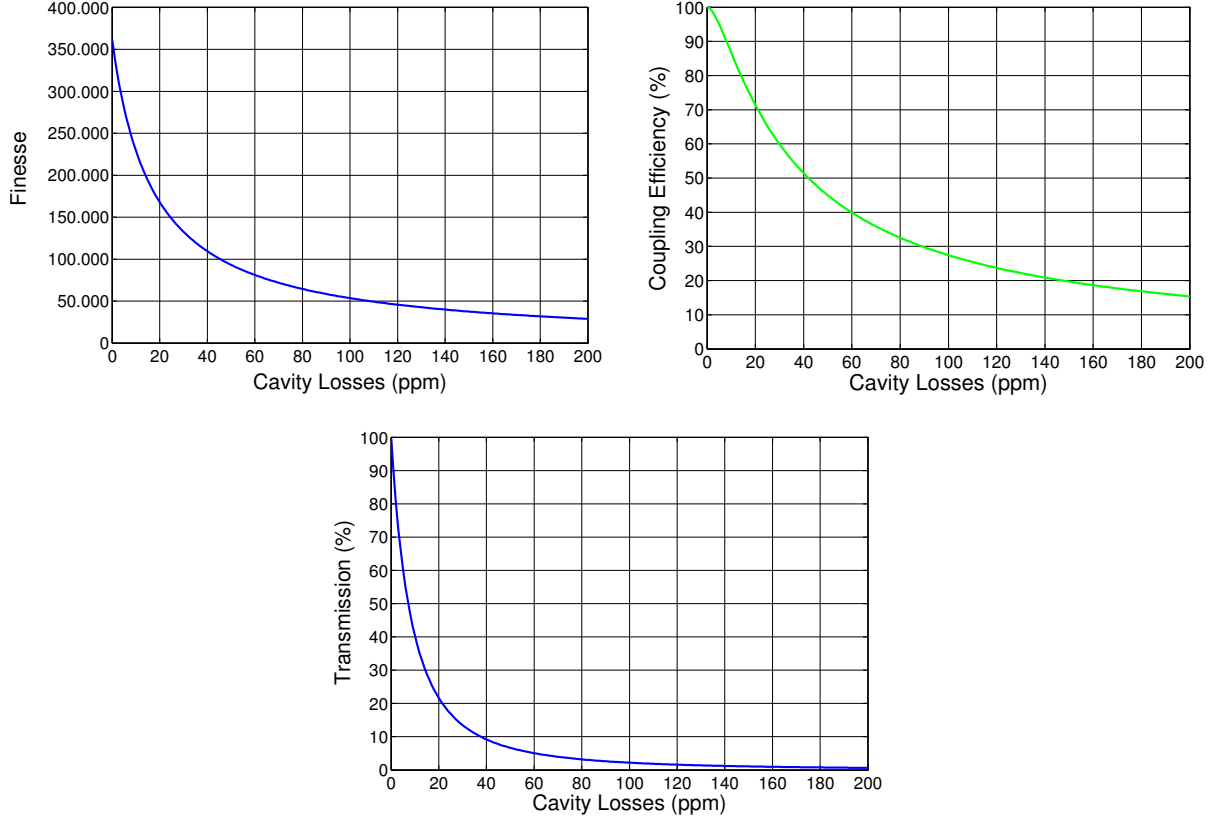


Figure 5.1.: Influence of cavity losses on finesse, coupling efficiency, and cavity transmission. The plots are calculated with a transmission of $T = 8.7 \times 10^{-6}$ for each mirror. The transmission is taken from manufacturer measurements.

The cavity losses $A = L_1 + L_2 + V$ are the sum of mirror losses $L_{1,2}$ and cavity round trip losses V . The cavity losses shown in Table 5.1 are calculated from the identified finesse. The cavity reflectivity R_C and transmission T_C in dependence of the cavity losses A are:

$$R_C = \left(\frac{A}{2T + A}\right)^2 \quad \text{and} \quad T_C = \left(\frac{2T}{2T + A}\right)^2. \quad (5.5)$$

The finesse, the coupling efficiency ($1 - R_C$), and the cavity transmission in dependence of the cavity losses are plotted in Figure 5.1.

Typical cavity losses are specified to be in the order of 1 ppm. The measured values are one to two orders of magnitude higher, which means that the mirrors got indeed polluted during the bonding process. The larger cavity resonance linewidths due to pollution of the cavity mirrors increase the sensitivity to detector shot noise (equation (4.4)) and lead to a greater influence of parasitic resonators and RAM. This may result in an increased frequency noise, which was however not observed in the measurements. As will be presented later, the frequency stability is limited by other effects. Thus, the degree of pollution is considered to be not critical.

5.2. Frequency noise with short circuited piezo actuator

To determine the intrinsic stability of the piezo-tunable cavities without any voltage related effects, the frequency noise of the different cavities was measured with short circuited piezo actuators before applying a voltage. As already presented in Chapter 2 the frequency noise has to be below $S_\nu = 280 \text{ Hz}/\sqrt{\text{Hz}} \cdot \sqrt{1 + (2.8 \text{ mHz}/f)^4}$ to fulfill the LISA requirements for a tunable pre-stabilization. In addition, the results will be compared with the more stringent requirements $S_\nu = 30 \text{ Hz}/\sqrt{\text{Hz}} \cdot \sqrt{1 + (3 \text{ mHz}/f)^4}$ which were valid at the beginning of this work.

5.2.1. Measurement and evaluation method

To analyze the frequency noise of the cavities, a time series of the beat frequency between a laser stabilized to a piezo-tunable cavity and a laser stabilized to the ULE reference (see Section 4.3.2) was recorded. From this time record the corresponding amplitude spectral density (ASD) and Allan deviation were calculated, which show the frequency noise spectrum and the frequency instability in the time domain, respectively (appendix A). The time record is taken with two different measurement methods: the low frequency range is sampled with the SR620 counter with a 1 Hz sampling rate and the high frequency range is sampled with the CNT-90 Pendulum counter with a 100 Hz sampling rate (see Section 4.3.2). The reason for this is, that the SR620 is well suited for taking long time records, but is not capable of making measurements with high sampling rates due to measurement dead times of up to 50 ms. During the low frequency measurements, the pneumatic vibration isolators were not floated to avoid slow tilt effects, whereas during the high frequency measurements they were floated to suppress vibrations.

The beat measurements show typical frequency drift rates of a few hundred Hertz up to 1 MHz per second (Figure 5.2), which are mostly caused by slow temperature variations due to oscillations of the air conditioning system (see Figure 4.9) and by creep of the spacer materials and of the adhesive. Large drifts show a great effect in the calculation of the ASD and especially of the Allan deviation and have thus to be removed before calculation. For this purpose, the function

$$f(x) = c_1 + c_2 \cdot t + c_3 \cdot \sin(2\pi \frac{t}{24 \text{ h}}) + c_4 \cdot \cos(2\pi \frac{t}{24 \text{ h}}) \quad (5.6)$$

was fitted to the times series and subtracted in each case. The linear term accounts for creep and the sine and cosine term for the temperature oscillations. Figure 5.2 shows a 20 000 s long time record of the beats of the cavities with PZT stack and PZN-PT actuator measured against the ULE reference before and after drift removal. The ASD and Allan deviation with and without removed drift can be seen in Figures 5.3a and 5.3b.

5.2.2. Results

The frequency noise spectral densities of all tested cavities are shown in Figure 5.4, while Figure 5.5 shows the corresponding relative Allan deviation. In each case, the presented Allan deviations and ASDs are calculated from the same beat record. The upper graphs show exemplarily the noise of the cavity with incorporated PZT stack actuator in comparison with the frequency noise of the ULE and FS reference cavities (Section 4.3.2) as well as the fixed cavity (Section 4.1.2). The lower graphs compare all piezo-tunable cavities built within this work.

5.2. Frequency noise with short circuited piezo actuator

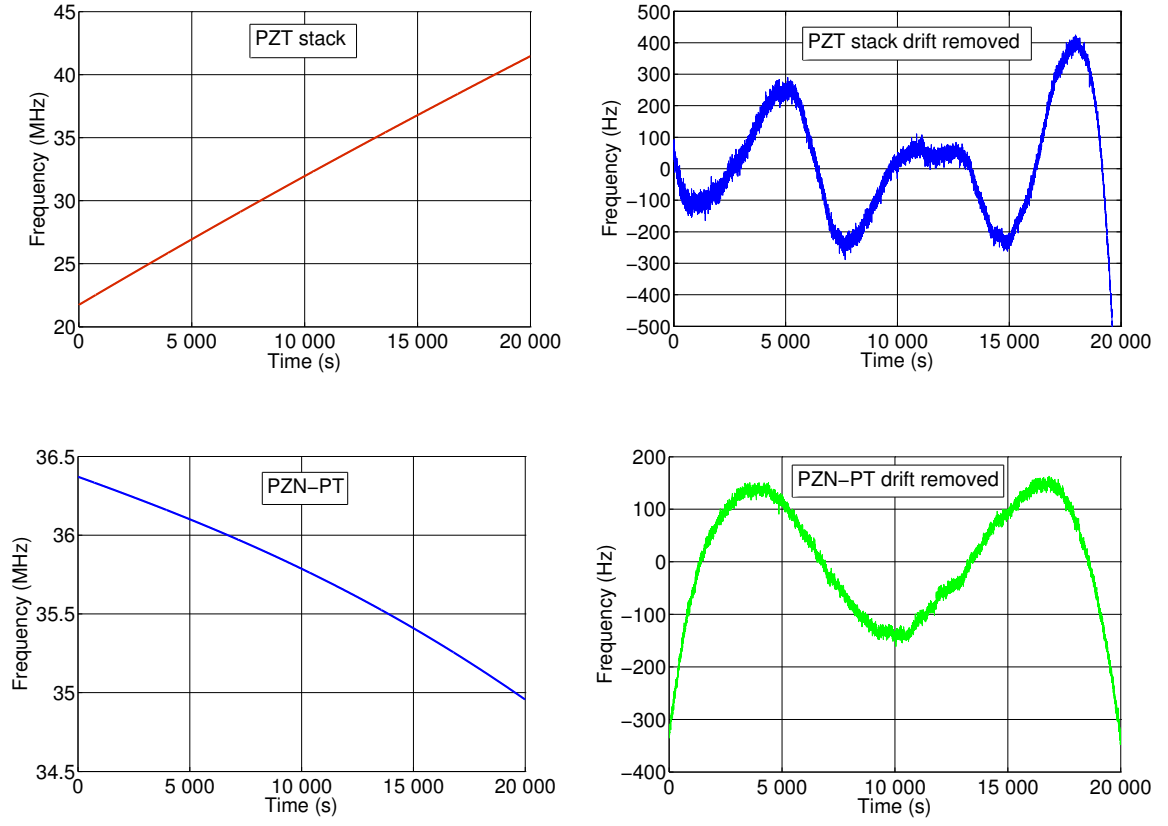


Figure 5.2.: Time record of the beat of the cavities with PZT stack and PZN-PT actuator measured against the ULE reference. Shown is the exact time record that was used for the calculation of the ASD and Allan deviation presented later. In the graphs on the right a drift is removed, which compensates material creep and oscillations of the air conditioning system (equation (5.6)).

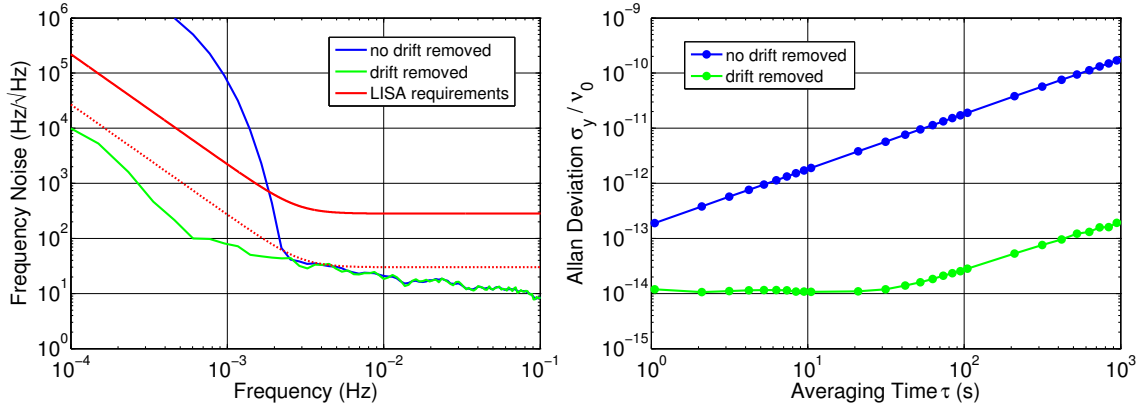
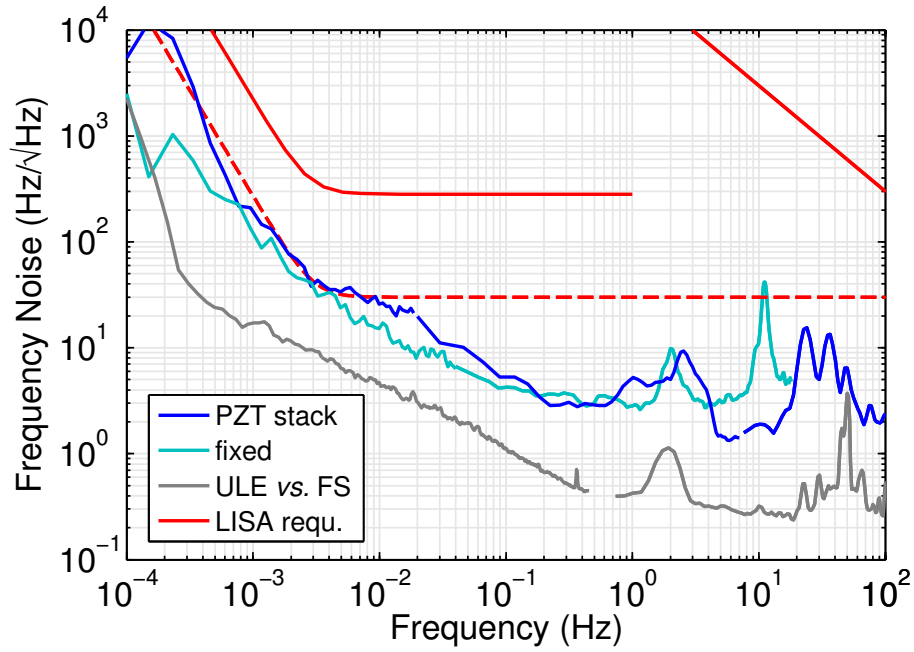
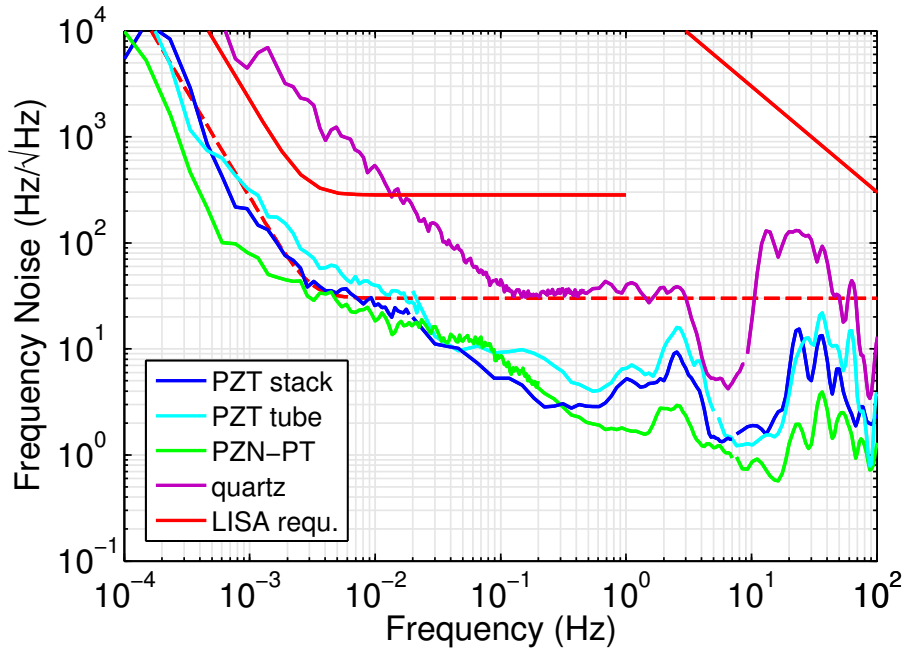


Figure 5.3.: ASD and Allan deviation of the cavity with PZN-PT actuator with and without removed drift.

5. Characterization of the Piezo-Tunable Cavities

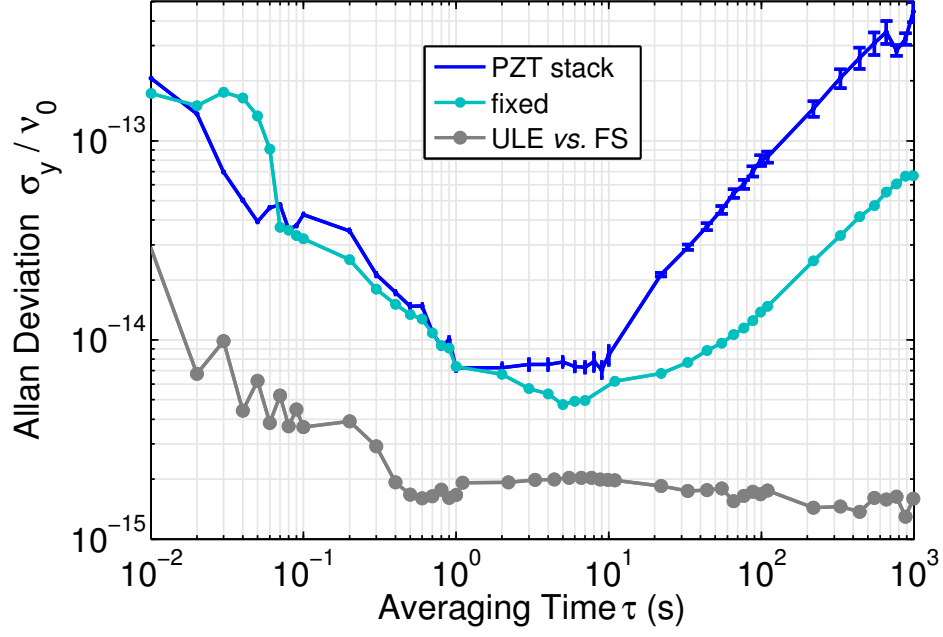


(a) ASD of the cavity with PZT stack actuator in comparison with the fixed cavity and the ULE cavity.

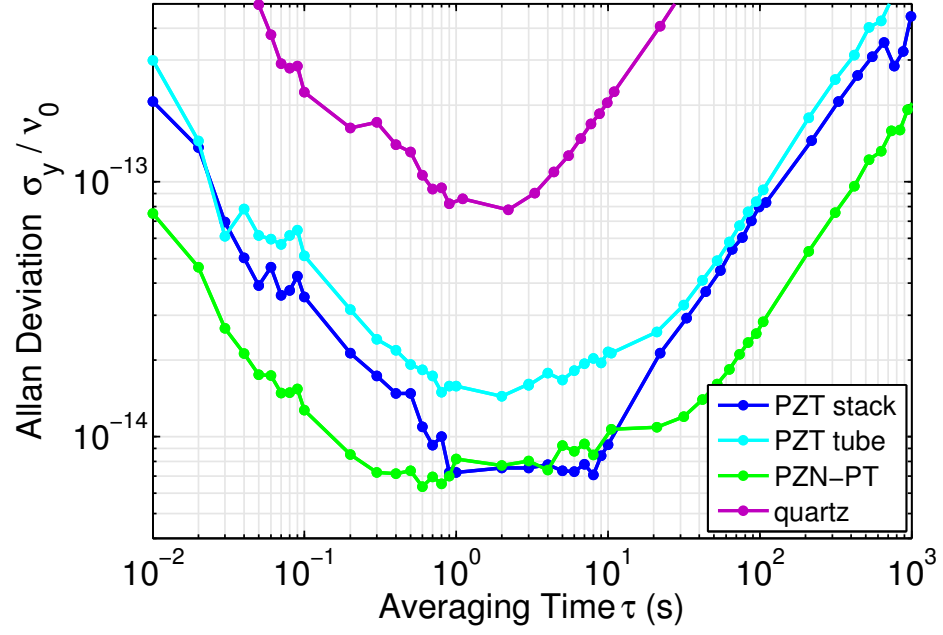


(b) Comparison of all piezo-tunable cavities.

Figure 5.4.: ASDs of the piezo-tunable cavities measured with short circuited piezo actuators against the ULE reference.



(a) Allan deviation of the cavity with PZT stack actuator. Typical error bars are shown for the Allan deviation of the cavity with PZT stack actuator.



(b) Comparison of all piezo-tunable cavities.

Figure 5.5.: Allan deviations of the piezo-tunable cavities measured with short circuited piezo actuators against the ULE reference.

5. Characterization of the Piezo-Tunable Cavities

All short circuited piezo-tunable cavities except for the cavity with quartz actuator show similar noise characteristics. At Fourier frequencies above 1 Hz the noise spectrum is dominated by seismic noise, while between ~ 4 mHz and 1 Hz the performance is limited by flicker noise and below ~ 4 mHz by random walk noise. The best performance is reached with the cavity with PZN-PT actuator, which shows a frequency noise below $30 \text{ Hz}/\sqrt{\text{Hz}}$ for Fourier frequencies above 3 mHz and a relative Allan deviation below 1×10^{-14} at integration times from 0.2 s to 10 s. The cavities with PZT stack and PZT tube actuator show a slightly increased noise level, mainly due to a higher sensitivity to seismic noise. This can be attributed to small differences in the gluing technique, which was improved over time (see next section). These three piezo-tunable cavities fulfill the LISA requirements on frequency noise for pre-stabilization (equation (2.17)) and the cavity with PZN-PT actuator even show a frequency noise which is completely below the more stringent requirement curve which was valid at the beginning of this work (equation (2.16)). The frequency noise of the cavity with the quartz actuator is much higher than that of the other piezo-tunable cavities, though most likely not due to its intrinsic properties. The frequency stability is limited by effects related to the adhesive as discussed in the next section.

A comparison of the performance of the fixed cavity with those of the piezo-tunable cavities shows that their flicker and random walk noise levels are approximately the same. The measurements with the fixed cavity were performed in the same setup where the piezo-tunable cavities were analyzed. Thus, it can be assumed that in the corresponding frequency range the frequency stability of the piezo-tunable cavities is not limited by the piezo actuator but by the experimental setup. It is most likely that the piezo-tunable cavities are in principle capable of achieving an even better performance.

5.2.3. Analysis of effects influencing the frequency stability

The frequency noise of the piezo-tunable cavities is about one order of magnitude above their fundamental noise limit, which is given by thermal noise (Table 4.9). The frequency noise thus has to be limited by other effects, arising from length changes of the cavity or from lock errors ($\delta\nu/\nu = -\delta L/L + \delta_{lock}$). It is quite interesting, that the fixed cavity and all piezo-tunable cavities (with the exception of the cavity with quartz actuator) have almost the same flicker and random walk noise. It seems like the limiting effect does not depend on the application of a piezo actuator. But also the differing linewidths of the cavities have apparently no influence. In the following, investigations on the sensitivity to various external disturbances are presented and compared with the corresponding noise levels, as well as with the theoretical values presented in Section 4.2.

Free spectral range measurements

To get a first impression of the limiting noise sources, two lasers were locked to two adjacent longitudinal modes of the cavity with PZT stack actuator and the beat frequency between these two lasers was recorded. Since the two lasers are locked to the same cavity, length changes of the cavity are common mode and thus suppressed in the beat signal. However, noise in the lock electronics is still present, since both lasers have individual lock electronics. The FSR

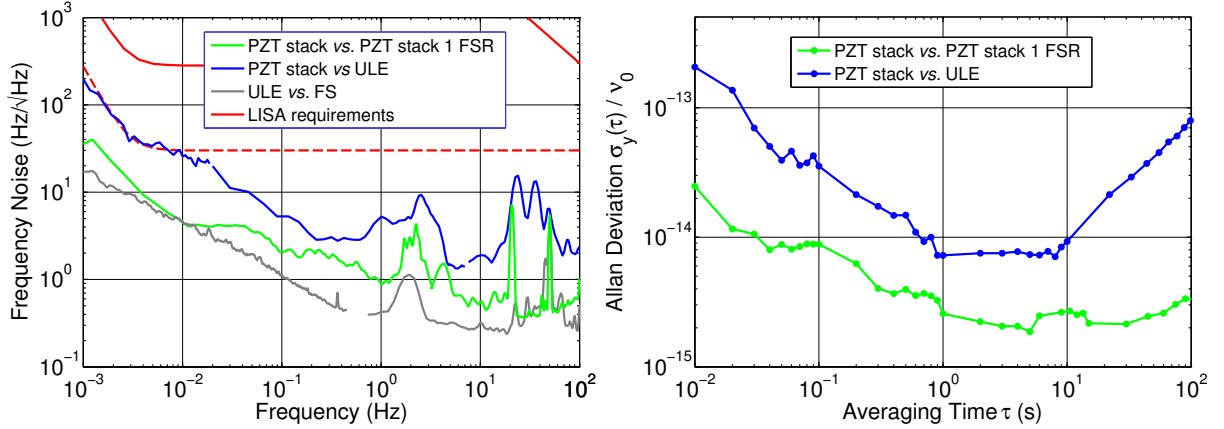


Figure 5.6.: ASD and Allan deviation of the beat between two laser which are locked to two modes of the cavity with PZT stack actuator separated by one FSR.

measurement can thus be used to estimate the limitation of the frequency stability by the lock electronics and to provide information about the lock errors δ_{lock} .

As can be seen in Figure 5.6, the noise level of the FSR measurement is about a factor 5 below the noise level of the cavity with PZT stack actuator measured against an independent reference. Thus, it can be concluded that the current frequency noise level of the cavity with PZT stack actuator is not limited by electronics. However, if the current limitations can be overcome and thermal noise limited performance could be achieved, the measured lock performance is not sufficient and has to be improved.

Intensity

To test the influence of a varying light intensity on the beat frequency, the intensity impinging on the cavity with PZT stack actuator was modified with a half wave plate and a PBS, while the intensity on the photo detector and the beat signal were recorded simultaneously. By turning the half wave plate, the intensity was changed from 20 μW to 8 μW . When changing the intensity by this amount, almost no effect on the beat frequency could be observed. The frequency change is nearly completely covered by frequency noise and can only be estimated to be below 25 Hz, which results in an intensity sensitivity below 2 Hz/ μW .

In the case of the cavity with PZN-PT actuator, an intensity change from 11 μW to 44 μW caused a fast change of the beat frequency of 360 Hz, followed by a slow frequency drift in the opposite direction (Figure 5.7a). The fast frequency change results in an intensity sensitivity of about 11 Hz/ μW . This value can be compared with the intensity sensitivity due to photothermal effects (Section 4.2.1). With equation (4.8) and the measured absorption coefficient of $A = 168 \times 10^{-6}$ a theoretical sensitivity of 0.13 Hz/ μW can be calculated. Since the measured sensitivity is almost two orders of magnitude above this value, it can be assumed that the intensity sensitivity depends not on photothermal but on other effects such as amplitude changes of the error signal. As presented in Section 4.2.1, when the error signal has an offset, amplitude changes shift the lock point and thus the measured beat frequency. Since constant

5. Characterization of the Piezo-Tunable Cavities

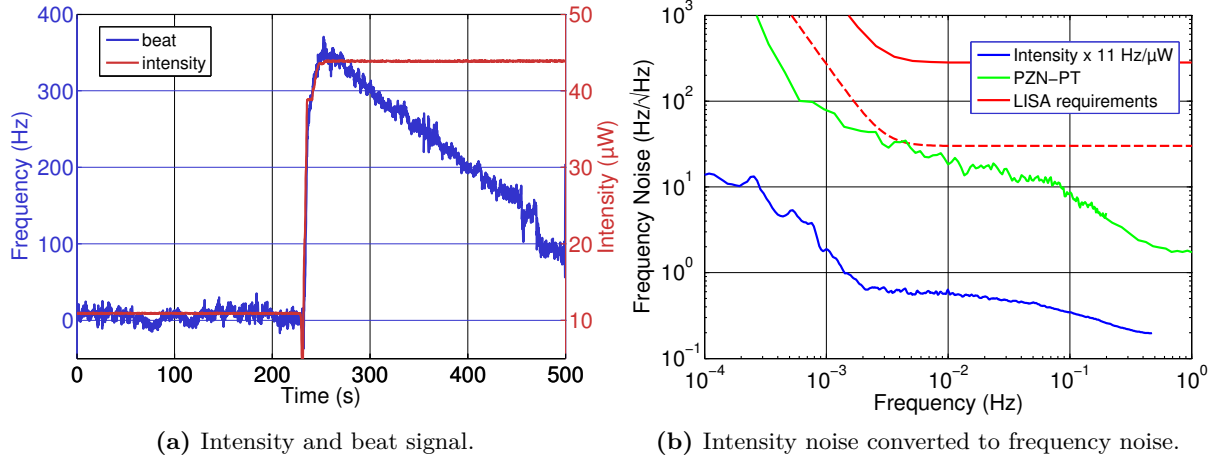


Figure 5.7.: Sensitivity to intensity changes. Left: beat signal during an intensity change of $33 \mu\text{W}$. Right: ASD of the intensity noise scaled with the sensitivity of $11 \text{ Hz}/\mu\text{W}$.

offsets are electronically compensated, a sensitivity to amplitude changes indicates the presence of varying offsets due to changing RAM or parasitic resonators. A closer examination of these two effects will be presented later.

To identify limitations of the frequency stability due to intensity fluctuations, a time record of the light intensity impinging on the photo detector was taken. The corresponding ASD was calculated, and scaled with the measured sensitivity (Figure 5.7b). The such converted noise is significantly lower than the measured frequency noise. However, it has to be considered that the sensitivity to intensity changes may be frequency dependent, and that the simple method which was applied to measure the sensitivity leads to incorrect results. Nevertheless, since the difference is more than one order of magnitude, this objection is most likely negligible and it is presumed that the actual frequency noise level is not limited by intensity noise.

Parasitic resonators

It could be observed, that the beat signal between two lasers stabilized to two adjacent TEM_{00} modes of the cavity with PZN-PT actuator features a modulation. The modulation has a more or less constant peak to peak amplitude of about 10 Hz but changing frequencies (Figure 5.8a). The frequency of the modulation signal could be influenced by heating the 8 m long optical fiber guiding the laser light to the vacuum chamber. This behavior is typical when a parasitic resonator is present in the setup. As described in Section 4.2.1, a parasitic resonator leads to an oscillation of the PDH error signal baseline (Figure 4.5a). When the optical fiber is in the optical path of the parasitic resonator, heating of the fiber continuously changes the length of the resonator and thus the offset between cavity resonance and maximal transmission of the parasitic resonator. As a result, the error signal is periodically shifted with the amplitude of the baseline oscillation, which is nearly constant. The frequency of the error signal offset oscillation depends on how fast the length of the parasitic resonator changes.

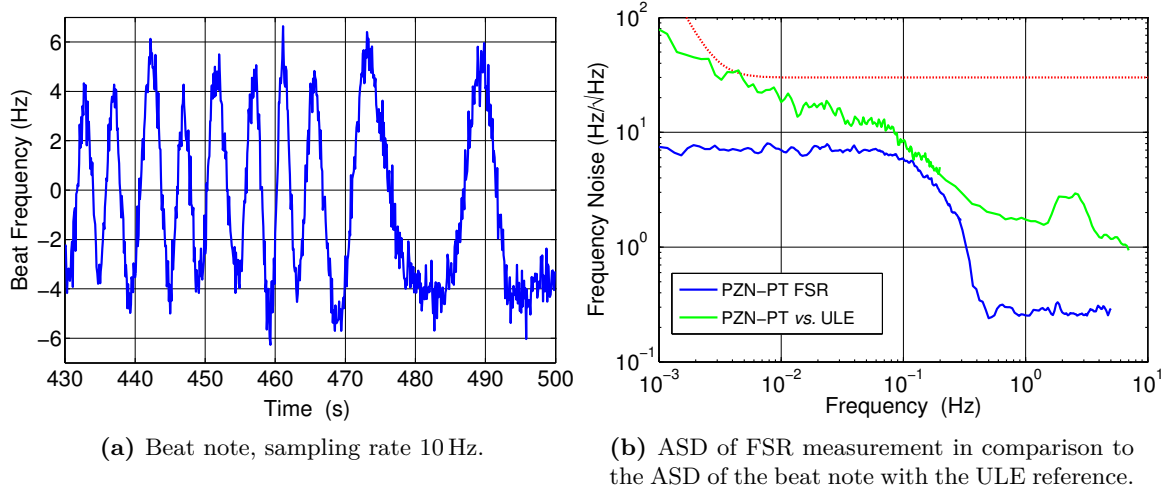


Figure 5.8.: Influence of parasitic resonators. Measurement with two lasers locked to two adjacent TEM₀₀ modes (FSR measurement) of the cavity with PZN-PT actuator. The beat note shows an oscillation with a relatively constant amplitude and a changing frequency, which is a typical signature in presence of a parasitic resonator. The ASD points out that parasitic resonators could be limiting in a small frequency band around 100 mHz.

The maximum length of the parasitic resonator was estimated to $L_E = L_F \cdot n_F + L_B \approx 13$ m, considering the optical path length in a fiber of length $L_F = 8$ m with a refraction index of $n_F = 1.4$ and an additional free beam path length of $L_B = 2$ m. Numerical calculations show that for the cavity with PZN-PT actuator and a laser modulation frequency of 1.8 MHz a parasitic resonator of that length and a reflectivity of $\sim 0.004\%$ would cause the observed modulation amplitude of 10 Hz. This is a relatively low reflectivity value, considering that the optical components in the setup have typical antireflection coatings with a reflectivity of 0.1%. It is more likely that elements with a higher reflectivity in combination with losses in the parasitic resonator lead to the observed magnitude of the effect. Losses occur, e.g., at the incoupling into the fiber, at polarizers and beam splitters, and at attenuation plates. Possible candidates building a parasitic resonator are the lenses in the fiber collimators, the optical isolators behind the lasers and the cavity itself, because those elements could not be tilted relative to the optical beam axis.

Figure 5.8b indicates that in a small frequency band around Fourier frequencies of 100 mHz parasitic resonators can be a limiting effect for the frequency stability of the cavity with PZN-PT actuator. However, as explained in section 4.2.1, the influence of a parasitic resonator depends on the modulation frequency of the laser. The presented measurements were performed with the LW124 laser with a modulation frequency of 1.8 MHz and the LW122 laser with a modulation frequency of 444 kHz stabilized to two adjacent longitudinal modes of the cavity. For the measurement against an external reference just one of the two lasers has to be applied. If the LW122 laser with its lower modulation frequency is chosen, the amplitude of the beat signal oscillation can be calculated to be only 2 Hz. Furthermore, the PZN-PT cavity has the largest

5. Characterization of the Piezo-Tunable Cavities

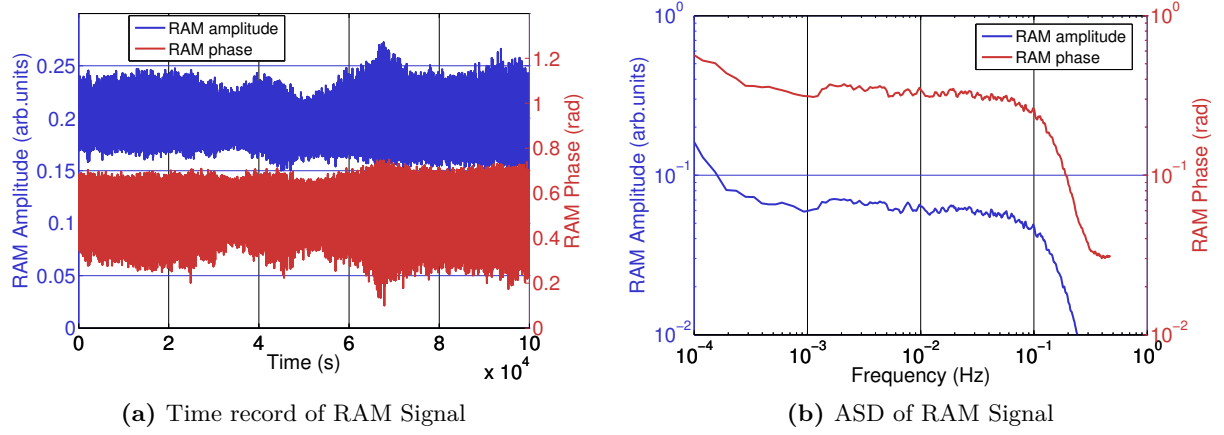


Figure 5.9.: Quadrature components of the RAM Signal.

linewidth (40 kHz) of all tested cavities and is thus most affected by parasitic resonators. In conclusion, parasitic resonators are most likely not a limiting factor for the current frequency noise level of the tested cavities.

Residual amplitude modulation

To estimate the influence of RAM, the amplitude of the first modulation sideband after the PDH photo detector was observed. The AC component of the signal while the laser frequency is in resonance was compared with the AC component while the laser is off resonance. Off resonance, a purely phase modulated laser features no AC component for lack of a frequency discriminator. In the presence of RAM, a signal arises at the modulation frequency, which was measured to $U_{\text{RAM}} = 250 \mu\text{V}$ for the cavity with PZN-PT actuator. For comparison, the DC signal is 1.6 V. On resonance, the phase modulated laser is discriminated by the cavity and signals at the modulation frequency and higher harmonics are present. The amplitude of the first sideband was measured to $U_e = 0.5 \text{ V}$. Thus, the RAM amplitude is about 0.05% of the error signal amplitude. It can now be estimated roughly, that with a RAM amplitude varying by p , the beat signal would vary by

$$\delta\nu = \frac{p U_{\text{RAM}}}{U_e} \frac{\Gamma_\nu}{8J_0(\beta)J_1(\beta)}, \quad (5.7)$$

where Γ_ν is the cavity resonance linewidth. If p is assumed to be 1%, this results in variations of $\delta\nu = 0.1 \text{ Hz}$, calculated with a cavity linewidth of $\Gamma_\nu = 40 \text{ kHz}$.

In addition, the frequency dependence of the RAM signal was observed by recording a time series, while the laser was locked to the cavity. The signal from the detector of the non resonant cavity (the cavity works thus just as mirror) was split and each part was demodulated with the modulation frequency, however with a phase difference of 90° . The resulting signals U_a and U_b were sampled with a sampling rate of 1 Hz. In this way the quadrature components of the RAM

5.2. Frequency noise with short circuited piezo actuator

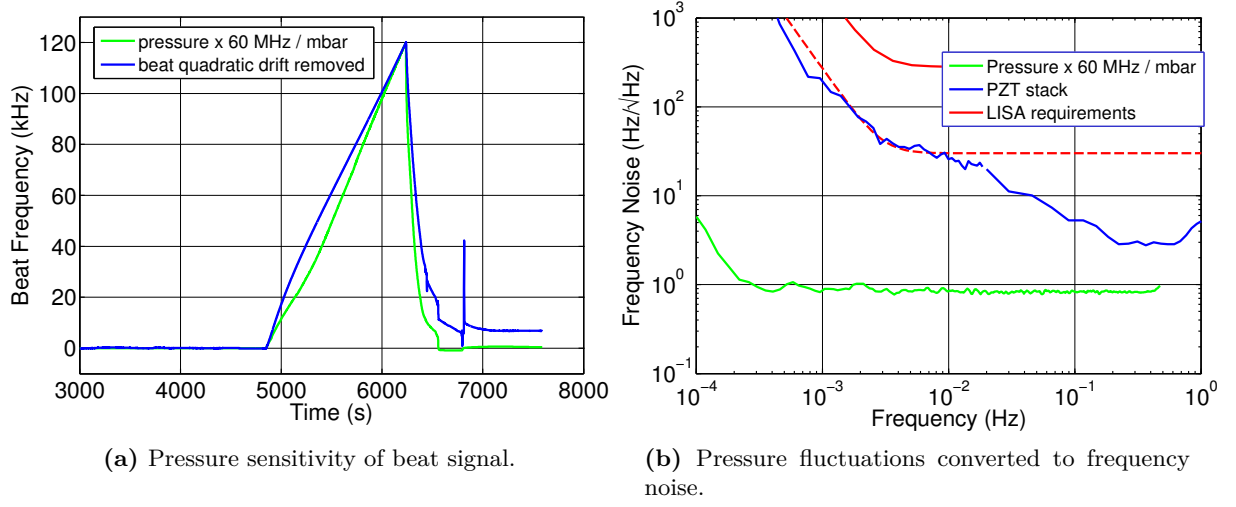


Figure 5.10.: Sensitivity to pressure changes of the cavity with PZT stack actuator and frequency noise due to pressure fluctuations. The pressure fluctuation measurement is limited by the measurement resolution over nearly the entire frequency range.

signal could be observed:

$$A_{\text{RAM}} = \sqrt{U_a^2 + U_b^2} \quad \text{and} \quad \phi_{\text{RAM}} = \arctan \frac{U_a}{U_b}. \quad (5.8)$$

The time record of the quadrature signals and the resulting ASDs are shown in Figure 5.9. The form of the ASD curves is similar to the form of the frequency noise curve shown in the parasitic resonator section (Figure 5.8). This is not surprising, since the parasitic resonator is of course also present in this measurement and seems to be the dominating effect here.

Pressure fluctuations

To measure the sensitivity to pressure fluctuations, the valve between the vacuum chamber and the turbo pump was closed. The subsequent pressure rise and the resulting beat change was measured simultaneously. To match the two time records the pressure was multiplied with a sensitivity factor of 60 MHz/mbar (Figure 5.10a). The experimentally determined sensitivity is in the same order of magnitude than the theoretical value of 84.6 MHz/mbar (Section 4.2.1).

A typical pressure noise spectrum measured with running turbo pump and scaled with the measured sensitivity is shown in Figure 5.10b. Above Fourier frequencies of 0.3 mHz the pressure spectrum is flat with a level of 1 Hz/√Hz. This white noise level is given by the measurement resolution, the actual pressure noise is even below this level. Consequently, the frequency stability is not limited by pressure fluctuations.

5. Characterization of the Piezo-Tunable Cavities

Temperature dependence and influence of adhesive

The sensitivity to temperature changes of the different cavities was observed by heating the outer thermal shield with the applied heating foil. The temperature of the inner thermal shield was compared with the beat frequency which was measured simultaneously. This gives a rough estimation of the cavity CTEs as listed in Table 5.2. The values are only considered as rough estimation, since the temperature was measured at the inner shield and not directly at the cavities, so that the real cavity temperature is not known exactly.

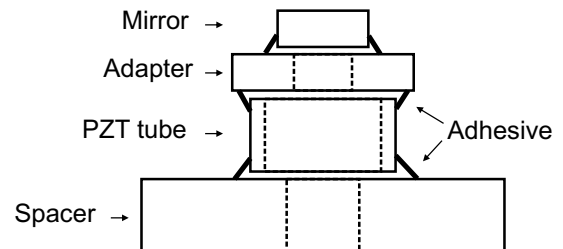
		PZT stack	PZT tube	PZN-PT
α_{cavity} measured	($10^{-6}/\text{K}$)	0.35	1.85	0.28
α_{cavity} calculated	($10^{-6}/\text{K}$)	0.35	-0.75	-

Table 5.2.: Thermal expansion of the cavities estimated from measurements in comparison with the calculated values (Table 4.5).

The value of the cavity with PZT stack actuator agrees perfectly with the calculated value. However, the value for the cavity with PZT tube actuator is considerably higher than the calculated value and has even the wrong sign. This discrepancy is assigned to the adhesive which was not considered in the cavity CTE calculations. The cavity with PZT tube actuator was glued at room temperature, later it was operated at 40 °C. Since the adhesive has the highest CTE in the assembly ($\alpha_K = 3 \times 10^{-5} \text{ 1/K}$), it is assumed that the expansion of the adhesive leads to small gaps between the cavity parts as indicated in Figure 5.11. With a gluing bridge length of 1.9 mm and considering all six gluing junctions, a cavity CTE of $1.88 \times 10^{-6} \text{ 1/K}$ is calculated, which agrees with the measured value.

For the cavity with PZT stack actuator the gluing was done more carefully such that the gluing bridges are shorter. When assembling the cavity with PZN-PT actuator, small dots were placed directly at the joint; gluing bridges were avoided. Furthermore, during gluing and curing, the cavity was heated with an infrared lamp to $\sim 50^\circ\text{C}$. In this way the contrary effect to the above described is anticipated. It is expected that the higher expansion of the adhesive pulls the cavity parts closer together, so that they are in direct contact and the adhesive plays a negligible role. This seems to work quite good since the cavity CTE measured for the cavity with PZN-PT actuator is rather low. However, since the CTE of PZN-PT is not known, no definite statement can be made. Under the assumption that the adhesive can be completely neglected a CTE of $9.2 \times 10^{-6} \text{ 1/K}$ can be estimated for the PZN-PT actuator. For the cavity with quartz actuator

Figure 5.11: Scheme of the cavity with PZT tube actuator with gluing bridges. Since the cavity was operated at a higher temperatures than it was exposed during curing, it is expected that the higher CTE of the adhesive leads to small gaps between the single cavity parts.



5.2. Frequency noise with short circuited piezo actuator

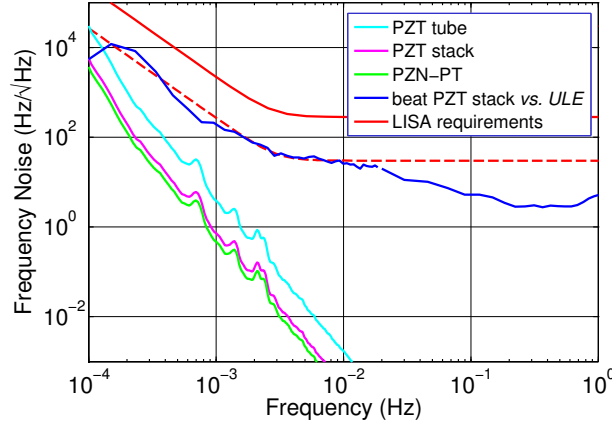


Figure 5.12.: Temperature noise converted to frequency noise using the measured CTEs for the cavities with PZT stack, PZT tube, and PZN-PT actuator. For comparison, the frequency noise derived from a beat measurement between the cavity with PZT stack actuator and the ULE reference is shown as well. Note that the bumps in the temperature spectra arise from measurement errors and contain no real signal.

no CTE measurement was done.

With the estimated CTEs the temperature stability at the cavities calculated in Section 4.3.1 (Figure 4.9f), can be converted to frequency noise. As can be seen in Figure 5.12, above Fourier frequencies of about 2×10^{-4} Hz all three cavities are not limited by length fluctuations of the cavity due to temperature fluctuations. The passive temperature shielding of the cavities is thus sufficient in this frequency range.

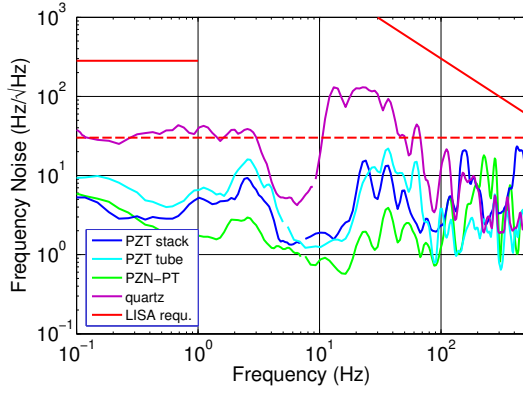
Another adhesive related effect that could be observed is that the Eccobond 285 epoxy did not provide sufficient stability after the specified curing time of 24 h within the measurement sensitivity of a few femtometer. When a cavity was placed in vacuum shortly after the specified curing time, 10 to 12 weeks were necessary to reach the noise levels presented above. Heating of the assembly under vacuum conditions did not significantly accelerate the curing process. Therefore, the cavity with PZN-PT actuator, which was assembled latest, was cured at normal pressure and elevated temperatures (50°C) to reduce the curing time to less than one week.

The quartz piezo cavity was disassembled after only a few weeks of measurement, since it could not be tuned as expected (see next section). As a consequence, measurements were only done when the adhesive was not yet fully cured. This is the reason why the frequency noise of the cavity with quartz actuator is so much higher than the frequency noise of the other cavities.

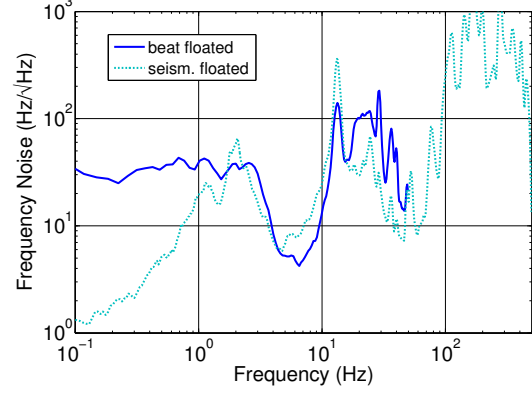
Vibrations

The frequency noise spectra of the piezo-tunable cavities (Figure 5.13a) show clearly that all cavities are affected by vibrations in the frequency range above ~ 1 Hz. Furthermore, it is obvious, that the vibration sensitivity of the different cavities differs significantly. This does not agree with the simulations, which indicate only small differences (Section 4.2.2, Table 5.3).

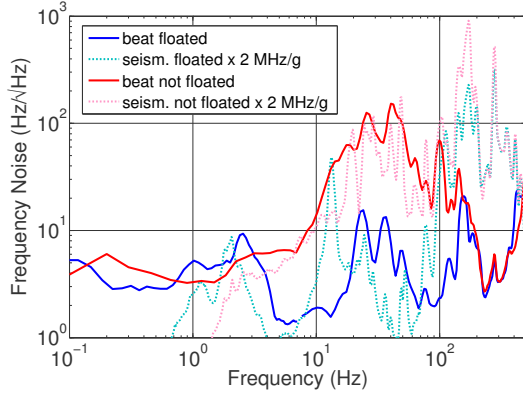
5. Characterization of the Piezo-Tunable Cavities



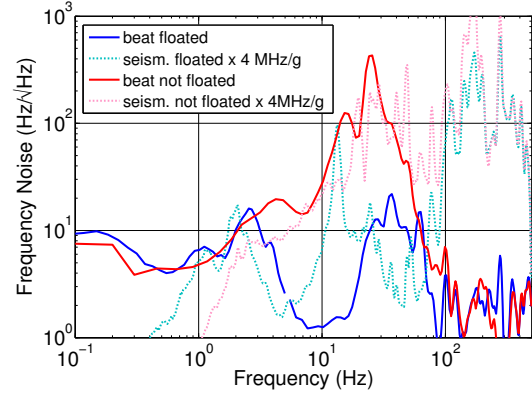
(a) Short term stability of all piezo-tunable cavities. Pneumatic isolators floated.



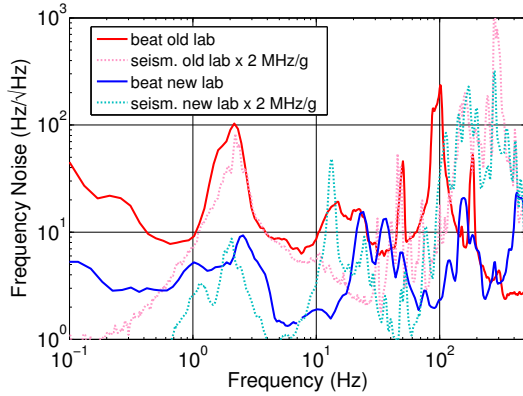
(b) Cavity with quartz actuator and vibration spectrum.



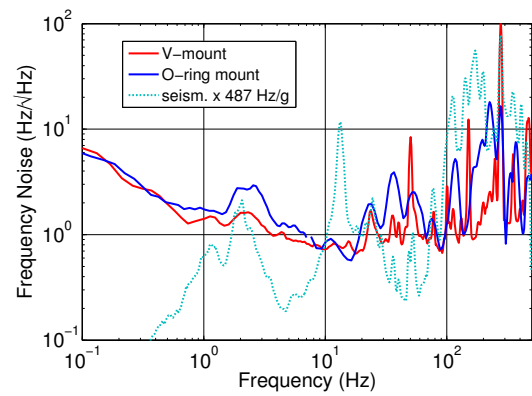
(c) Cavity with PZT stack actuator. Comparison isolators floated / not floated.



(d) Cavity with PZT tube actuator. Comparison isolators floated / not floated.



(e) Cavity with PZT stack actuator. Comparison old and new lab.



(f) Cavity with PZN-PT actuator. Comparison O-ring mount and V-mount.

Figure 5.13.: Sensitivity to vibrations. See main text for further description.

5.2. Frequency noise with short circuited piezo actuator

		PZT stack	PZT tube	PZN-PT	quartz
v_{cavity} measurements	(kHz/g)	2000	4000	500	15000
v_{cavity} simulations	(kHz/g)	553	369	487	513

Table 5.3.: Vibration sensitivity estimated from measurements in comparison with the values derived from simulations (Table 5.3).

All measurements were made while the cavities were mounted in their Airy points as depicted in Figure 4.10b. Vibration measurements with a seismometer were taken simultaneously with beat measurements of the cavity with quartz actuator. Figure 5.13b shows a direct comparison of the two spectra at which the seismic noise was scaled with a sensitivity of 15 MHz/g. The two spectra match only to a certain degree. Apparently the seismic background measured directly at the cavity is slightly different from that measured on top of the vacuum chamber. Nevertheless, it can be estimated that the sensitivity is almost 30 times as large as the value derived from simulations (Table 5.3). This can be attributed to the differing mounting and to the adhesive which was not considered in the simulations. The cavity with quartz actuator has the highest sensitivity, probably since the adhesive was not fully cured when taking the measurements.

For the other cavities no simultaneous measurements of beat and vibrations were performed, so the frequency spectrum is compared with the same vibration spectrum, assuming that the seismic background has not changed. This leads, of course, only to rough estimations of the sensitivity. Note, for example, that the seismic peak at 13 Hz is not present in the other beat measurements. Figures 5.13c and 5.13d show the comparison for the cavities with PZT stack and PZT tube actuator. Here, measurements were also made, while the pneumatic isolators were not floated, which allows a better comparison. The sensitivities are estimated to 2 MHz/g for the cavity with PZT stack actuator and 4 MHz/g for the cavity with PZT tube actuator. For the cavity with PZT stack actuator measurements in the old laboratory having another seismic background were performed, too (Figure 5.13e). During these measurements the cavity was mounted as depicted in Figure 4.10a. The graph shows that the improvement of the short term stability in the new laboratory arises most likely only from the lower seismic background and not from the changed mounting. The different mounting techniques seem to have only minor influence.

For the cavity with PZN-PT actuator a further mounting technique could be compared. This cavity was the only cavity that was also mounted on a copper V-mount, which was designed for later experiments presented in the next chapter. As can be seen in Figure 5.13f, the vibration sensitivity with the V-mount is slightly lower than the sensitivity with the O-ring mount, indicating that the cavity was not mounted exactly in its Airy points, during the O-ring measurement. (As already mentioned in Section 4.2.2, the two mounting techniques theoretically should show no difference in sensitivity [65]). For comparison the figure shows also the seismic noise scaled with the theoretical sensitivity of 487 Hz/g derived from simulations. For the PZN-PT cavity the measured sensitivity fits quite well with the calculated sensitivity. This leads to the conclusion that the vibration sensitivity of the piezo-tunable cavities is influenced by the adhesive and by the applied gluing technique. The sensitivity of the cavity with PZN-PT actuator, which was

5. Characterization of the Piezo-Tunable Cavities

assembled with the most advanced gluing technique (as described above), seems to be the only one not affected by the adhesive.

If necessary, the vibration sensitivity could be further reduced by applying special vibration insensitive designs [22–24], though they would need to be adapted for a piezo-tunable cavity. Since the focus of this work was on the frequency stability in the low frequency range, where seismic is not limiting, this was not further pursued.

Tilt

The tilt sensitivity of the cavity with PZT stack actuator was measured by constantly releasing the pressure in two adjacent pneumatic isolators which results in a slow tilting of the vacuum chamber of up to 10 mrad. Accordingly, the optical axis of the cavity is tilted against the horizontal. The tilt angle of the chamber was measured with an two-axis bubble-level tilt sensor (Applied Geomechanics, 755) and recorded simultaneously with the frequency of the stabilized laser. By searching the adequate scaling factor to match tilt and beat (Figure 5.14a) the tilt sensitivity was determined to $7.15 \text{ Hz}/\mu\text{rad}$. This value is about a factor 2.5 higher than the calculated sensitivity of $3.3 \text{ Hz}/\mu\text{rad}$ (Section 4.2.2). Possible reasons for this discrepancy are the influence of the adhesive, which was neglected in the calculation of the theoretical value, or beam pointing effects, (Section 4.2.1) which are induced due to bending of the breadboard in the vacuum chamber during tilting. Another possible reason is that the mounting of the cavity especially the soft O-rings cause a bigger tilt of the cavity than it is measured with the tilt sensor on top of the vacuum chamber.

The above described measurements were also done while the vacuum chamber was tilted in the direction perpendicular to the previous. Since in this case, the optical axis of cavity should not tilt against the horizontal, a change of the cavity resonance frequency is not expected. However, a sensitivity of $0.9 \text{ Hz}/\mu\text{rad}$ was measured (Figure 5.14b), which can be explained by an imperfect decoupling of the two axes in the measurement setup and also with pointing effects.

With the tilt sensor on top of the vacuum chamber the tilt values were sampled over a time span of several hours. The spectral density of this time series was taken and scaled with the measured tilt sensitivities. The time record and the resulting noise level are shown in Figure 5.14c and 5.14d. Frequency noise from slowly tilting of the vacuum chamber is not yet limiting, but in the frequency range from 3 mHz to 10 mHz, it is only a factor 3 below the current noise level. To reduce the sensitivity a modified mounting of the cavities could be helpful. The presented measurements were made when the cavity was mounted in the configuration as shown in Figure 4.10c. Measurements with other mounting version have not been made.

Since the calculations state that the cavity with PZT stack actuator has the highest tilt sensitivity, it can be assumed that the other cavities are likewise not limited by tilt effects.

Discussion

In the high frequency range above $\sim 1 \text{ Hz}$, the frequency stability of all cavities is dominated by seismic noise. The overall limiting effect in the low frequency range could not be identified, even though several effects influencing the frequency stability were analyzed. Figure 5.15 shows a summary of the investigated influences on the cavity with PZT stack actuator. Tilt and

5.2. Frequency noise with short circuited piezo actuator

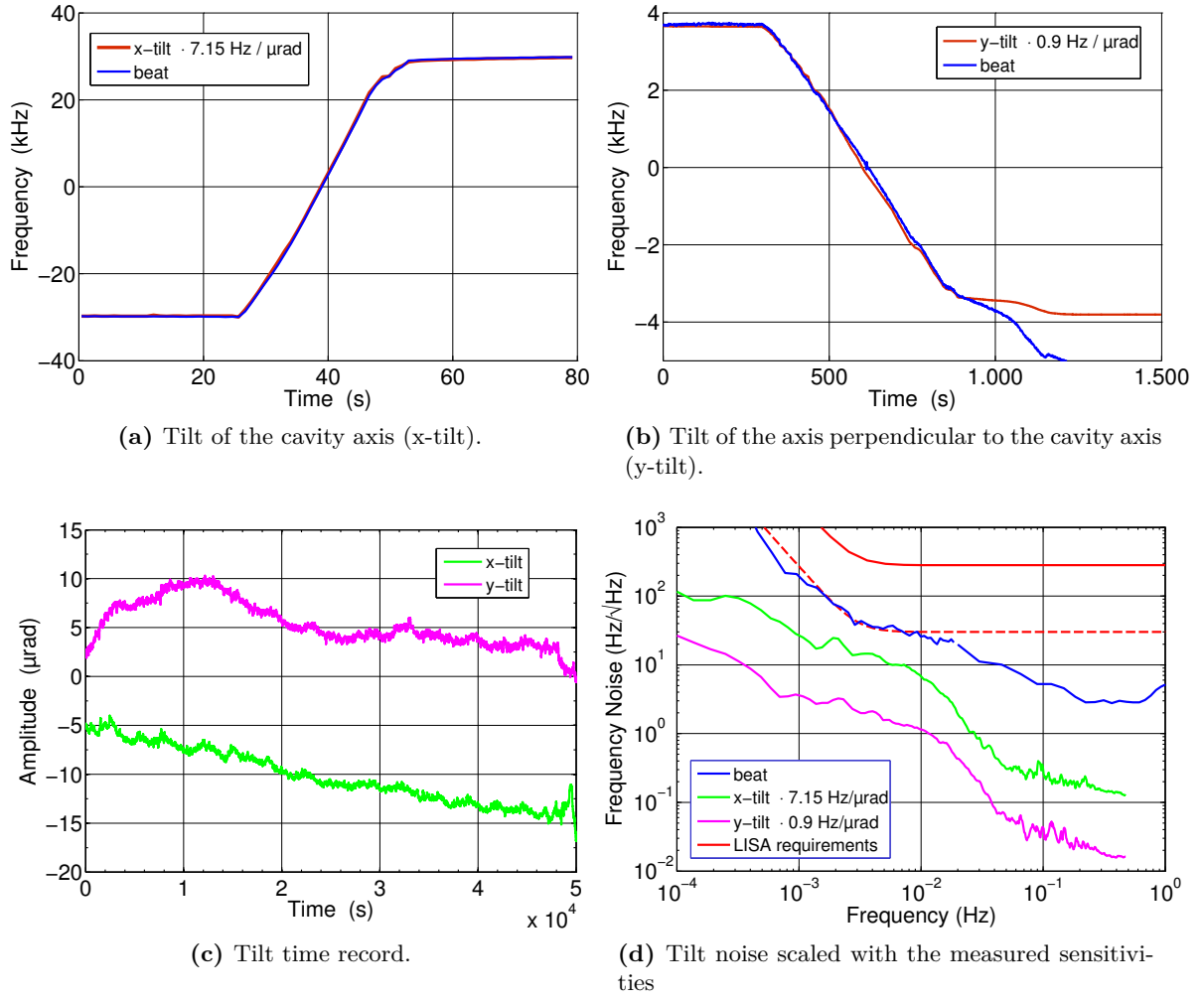


Figure 5.14.: Tilt sensitivity and tilt fluctuations.

5. Characterization of the Piezo-Tunable Cavities

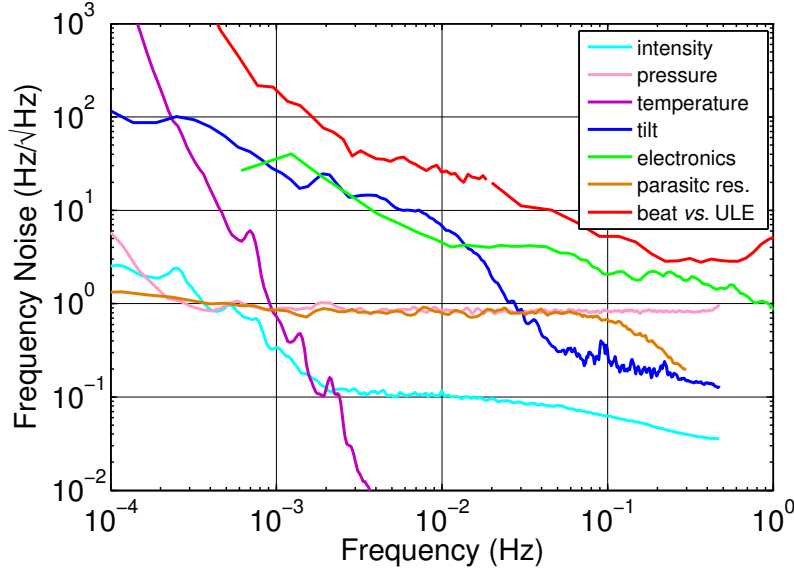


Figure 5.15.: Summary of influences on the frequency stability in the low frequency range for the example of the cavity with the PZT stack actuator.

electronics have the highest contribution but are not yet limiting. Since all cavities including the fixed cavity have the same noise level the limiting effect is most likely not caused by the piezo actuator. But the limiting effect seems also not to depend on the cavity resonance linewidth, which differs by a factor of up to 4 for the different cavities (Table 5.1).

One candidate, whose influence has not been investigated so far is beam pointing. As described in the Section 4.2.1 beam pointing can affect the frequency stability in different ways. The effect is indeed independent of the application of an actuator, but, if it couples in the beat frequency via lock point shifts, it should be dependent on the linewidth of the cavity resonance.

To sum up, the effect limiting the long term frequency stability could not be identified and thus no conclusive statement on the intrinsic stability of piezo-tunable cavities can be made. Nevertheless, the presented stability for the short circuited cavities is the best ever achieved with piezo-tunable cavities and all piezo-tunable cavities (except for the cavity with quartz actuator, which is limited by adhesive related effects) fulfill the LISA requirements on frequency noise for a tunable pre-stabilization.

5.3. Applying a voltage

In all previous investigations, the piezo-tunable cavities were examined while the incorporated actuators were short circuited to analyze the intrinsic stability of the cavities. Since the purpose of building a cavity with incorporated piezo actuator is of course to gain tunability, the piezo-tunable cavities need to be operated with applied voltage. Thus, the frequency stability of the piezo-tunable cavities with applied voltage and the tuning behavior including piezo effects such as hysteresis and creep are analyzed in the following.

5.3.1. Tuning range

To determine the tuning coefficients of the different piezo-tunable cavities, the frequency change resulting from a voltage change was measured. The coefficients are listed in Table 5.4 together with the maximum tuning range $\Delta\nu_{max}$. For the calculation of the maximum tuning range it is considered that -200 V to 1000 V can be applied to each actuator. The tuning coefficient of the cavity with quartz actuator could not be measured because the piezo effect was covered by another effect, as described in Section 5.3.3.

		PZT stack	PZT tube	PZN-PT
$\Delta\nu/U$	(MHz/V)	7.5	12	2.2
$\Delta\nu/U$ calculated	(MHz/V)	13.2	9.1	4.9
$\Delta L/U$	(nm/V)	2.8	5.5	0.86
$\Delta\nu_{max}$	(GHz)	9	14.4	2.6
$\Delta\nu_{max}/\text{FSR}$		6.5	12.6	1.9

Table 5.4.: Tuning coefficients and tuning range.

The values differ up to more than a factor 2 from manufacturer specifications or calculated values. The measured tuning coefficient of the cavity with PZT tube actuator is slightly higher than the calculated value. This could arise from imprecise manufacturer specifications concerning the dimensions of the tube. The values for the cavities with PZT stack actuator and PZN-PT actuator are about half the size as expected from manufacturer specifications. A possible reason for this could be a partly depoling of the piezo materials due to aging or improper handling. Nevertheless all three piezo-tunable cavities exhibit the tuning range of $\pm 30\text{ MHz}$ required for LISA as well as a tuning range of more than one FSR, which allows full flexibility in the choice of the laser frequency.

5.3.2. Voltage noise

As mentioned in the previous chapter a low noise voltage reference and low noise amplifiers are required for building piezo control electronics. The voltage noise of the applied REF02D voltage reference (Analog Devices) turned out to be sufficiently low to not increase the above presented frequency noise of a short circuited piezo-tunable cavity. More attention, however, had to be paid to the voltage noise of the amplifiers.

5. Characterization of the Piezo-Tunable Cavities

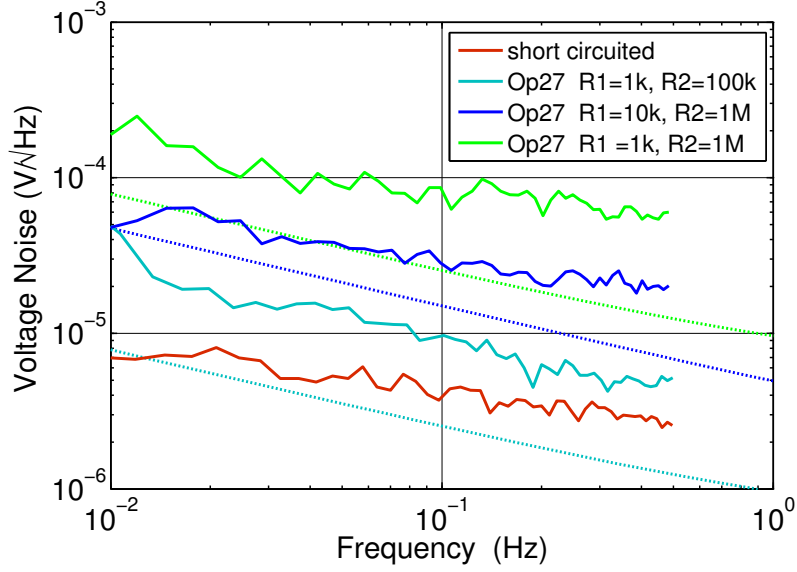


Figure 5.16.: Voltage noise of the OP27G operational amplifier while operated as inverting amplifier with different resistors. R_1 is the input resistor and R_2 the feedback resistor as depicted in Figure 4.7. The solid lines describe measured frequency noise converted into voltage noise, the dotted lines describes the voltage noise calculated with equation (4.37) and the appropriate amplification factor. The input of the amplifier was short circuited during the measurements.

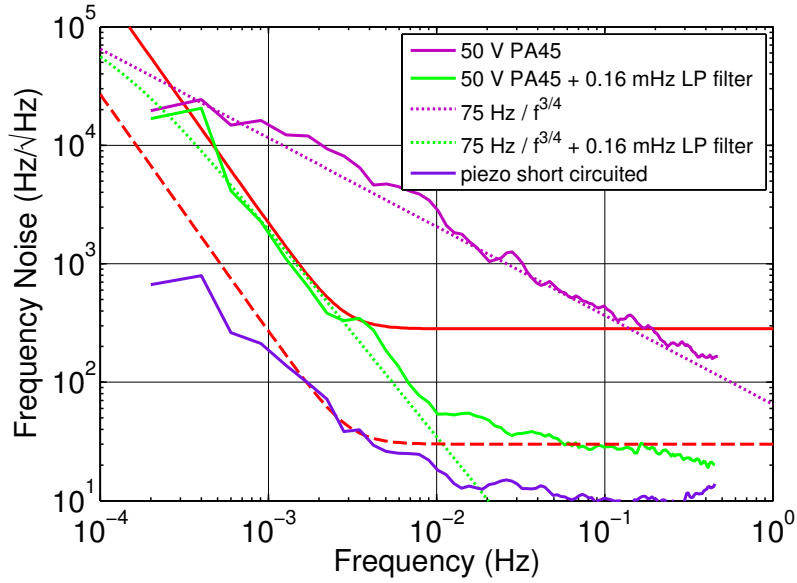


Figure 5.17.: Frequency noise of the cavity with PZT stack actuator while driven with the PA45 amplifier. The amplifier was operated with an amplification of 10.

In the low voltage range an inexpensive OP27G (Analog Devices) operational amplifier was employed. The voltage noise at the output of this amplifier was measured while different resistors were applied for amplification (Figure 5.16). The voltage noise is derived from frequency noise measurements with the cavity with PZT stack actuator using the corresponding tuning coefficient. The theoretical noise was calculated with formula (4.37) and the manufacturer specifications: $e_n = 3.2 \text{ nV}/\sqrt{\text{Hz}} \cdot \sqrt{1 + 2.7 \text{ Hz}/f}$ and $i_n = 0.4 \text{ pA}/\sqrt{\text{Hz}} \cdot \sqrt{1 + 140 \text{ Hz}/f}$. In the low frequency range, voltage noise arising from current noise dominates due to its higher $1/f$ noise corner frequency. The measured values differ slightly from the calculated values but are in the right order of magnitude. In the actual setup the OP27 is operated with a maximum amplification of 10. In this configuration its voltage noise does not increase the frequency noise measured with short circuited actuator.

To tune the cavities over more than one FSR, one need to apply a HV amplifier. A PA45 (Apex) operational amplifier was used to drive a piezo with up to $150 \text{ V}_{\text{pp}}$. This amplifier was selected due to its low noise performance. Nevertheless, the application of the PA45 amplifier operated with an amplification of 10 caused a considerably increase in frequency noise (Figure 5.17). To suppress the frequency noise below the LISA requirements a 0.16 mHz low-pass filter (metallized polypropylene capacitor $10 \mu\text{F}$, 10 metal film resistors $10 \text{ M}\Omega$ in series) was applied. The frequency noise may be suppressed further using a low-pass filter with a lower corner frequency. This would require even greater capacities and resistances, which is in principle possible, but not easy to implement.

Frequency separating filter The application of a low-pass filter after the HV amplifier disables fast tuning of the cavity resonance frequency. To overcome this restriction, an AC coupled low voltage bypass path was added to the filter, leading the control signal from an OP27 operational amplifier directly to the piezo actuator without further amplification (Figure 5.18). This enables both, slow tuning over a wide tuning range and fast tuning of the cavity with a tuning range of several 10 MHz without increase in frequency noise. The frequency separating filter thus allows small but fast variations around a high offset voltage. Other possibilities to achieve this is to use a floating high power voltage supply and introduce fast voltage changes by varying the ground [70], or, when the cavity is equipped with two piezo actuators, to use one actuator for the high tuning range and the other for the fast variations [18].

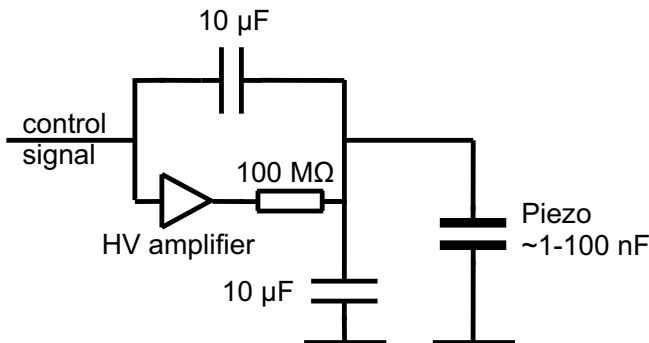


Figure 5.18: Frequency separating filter. The control signal processed by an OP27 operational amplifier is split. One part is fed over a capacitor directly to the piezo actuator forming a fast, low voltage path. The other part is amplified with a high voltage amplifier and subsequently low-pass filtered with a corner frequency of 0.16 mHz and then fed to the actuator, forming a slow high-voltage path.

5. Characterization of the Piezo-Tunable Cavities

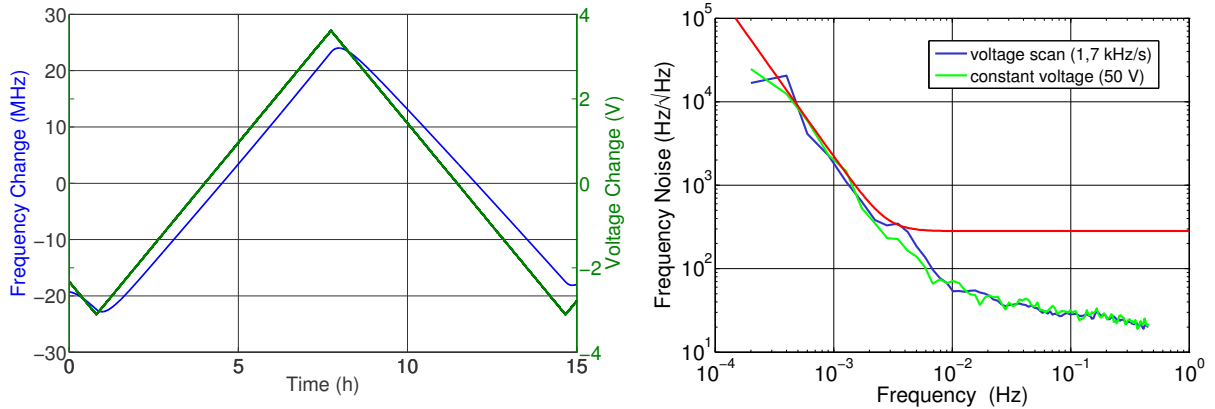


Figure 5.19.: Slow frequency scan of the laser locked to the cavity with PZT stack actuator by applying a voltage ramp of 0.2 mV/s to the actuator. While this slowly changing voltage is applied to the cavity, the frequency noise of the cavity still fulfills the LISA requirements on frequency noise for a tunable pre-stabilization. During the scan, as well as for the measurement with constant voltage, the 0.16 mHz low-pass filter was applied.

5.3.3. Influence of a varying piezo driving voltage

To test the effect of a slowly varying driving voltage, a voltage ramp was applied to the cavity with PZT stack actuator. While using the low-pass filter described above, the voltage was slowly increased from 36 V to 43 V which resulted in a frequency change of 50 MHz (Figure 5.19). With a 0.2 mV/s voltage ramp (corresponding to 1.7 kHz/s) no degradation of the frequency stability measured with a constant high voltage was observed. Since the frequency changes expected in LISA are even slower, this measurement demonstrates that the frequency noise of a piezo-tunable cavity fulfills the LISA requirements even when a changing driving voltage is applied to the actuator.

Later, the influence of a fast changing driving voltage was also investigated (Section 6.3.3). It could be demonstrated that a piezo-tunable cavity which is driven by a fast sinusoidal signal shows no degradation of the frequency stability. These measurements were carried out with the prestressed cavity, which is described in detail in the next chapter.

Nonlinearities

Under the influence of a changing driving voltage, the piezo-tunable cavities show hysteresis and creep in a magnitude which is in accordance with manufacturer specifications. Both hysteresis and creep might be disturbing when using a piezo-tunable cavity, since they prevent an accurate adjustment of the resonance frequency in dependence of the piezo driving voltage. However, these effects play a negligible role in applications where the tunable cavity is integrated in an external feedback loop, as planned for LISA. Thus, no thorough investigation of hysteresis and creep was done in this work and just a brief description of the observed effects will be given in the following.

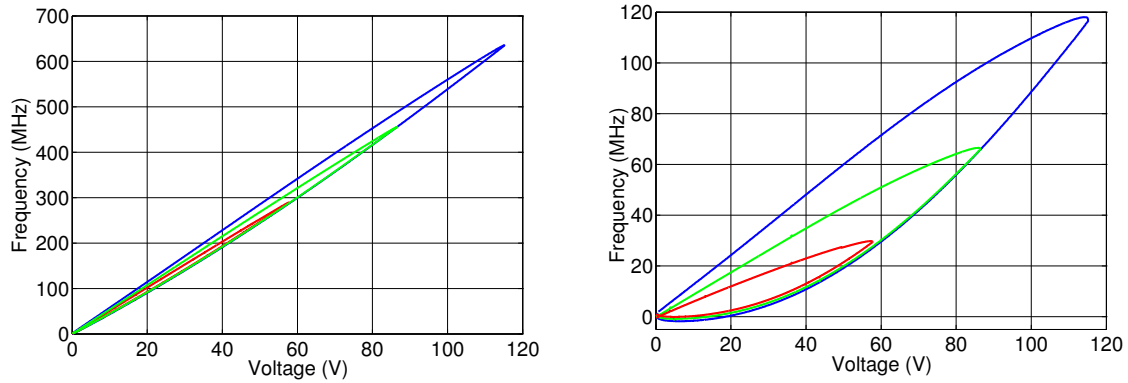


Figure 5.20.: Hysteresis of the cavity with PZT stack actuator for different maximum voltages. In the graph on the right a straight line with a slope of 4.5 MHz/V was subtracted for better presentation.

Hysteresis To test the influence of hysteresis, a slow voltage ramp was applied to the piezo actuator. For this purpose a HP 33120A function generator from Hewlett Packard was used, which was amplified with an operational amplifier (Apex, PA45). The applied voltage and the beat frequency were measured simultaneously. Figure 5.20 shows the beat frequency plotted versus the voltage for different maximum voltages applied to the cavity with PZT stack actuator. The curve has the typical hysteresis form for low electric fields (Figure 3.10). Table 5.5 shows the ratio between maximum opening and total frequency change for each curve. As described in the literature [50] the amount of hysteresis increases with increasing voltages.

U_{max} (in V)	120	90	60	30
PZT stack	6.5%	5.1%	3.8%	3.2%
PZT tube			1.8%	
PZN-PT			2.2%	

Table 5.5.: Maximum opening in the hysteresis curve in dependence of the applied voltage. Shown is the ratio between maximum opening and total frequency change.

The hysteresis behavior of the PZT stack, the PZT tube and PZN-PT actuators was compared by recording the voltage/displacement curve applying the same voltage ramp to the actuators. With a maximum applied voltage of 60 V the maximum opening in the voltage/displacement curve is 3.8% for the PZT stack actuator, 1.9% for the PZT tube actuator and 2.2% for the PZN-PT actuator. Since the PZT tube actuator has at the same time the highest displacement at this voltage it would be suited best for applications where hysteresis is a critical issue. The cavity with quartz actuator should show no hysteresis, since hysteresis is an effect arising from the domain structure of ferroelectrics. This could, however, not be observed in measurements, since the piezo effect of the cavity with quartz actuator was superimposed by another effect as described in the next section.

5. Characterization of the Piezo-Tunable Cavities

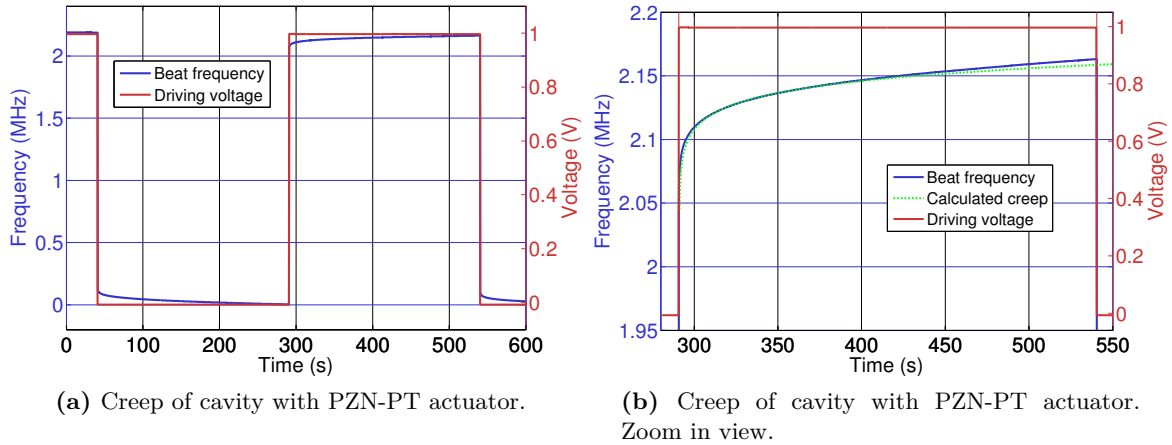


Figure 5.21.: Creep of the cavity with PZN-PT actuator.

Creep Figures 5.21a and 5.21b show the creep measured with the cavity with PZN-PT actuator after a voltage step of 1 V corresponding to 2.2 MHz. The measured creep agrees with the theoretical creep, if $\gamma = 0.0075$ is used for calculation (equation (3.45)). For the cavity with PZT stack actuator the creep was measured after a voltage step of 200 mV which corresponds to a frequency step of 1.1 MHz. Here, $\gamma = 0.0055$ could be estimated, which is slightly below the manufacturer specifications of 0.01 to 0.02.

Tuning behavior of the cavity with quartz actuator

When a voltage was applied to the cavity with quartz actuator the beat frequency showed an unexpected behavior. A slow frequency change could be observed which is much higher than the expected piezo effect. A voltage change of 40 V should result in a frequency change of 500 kHz. Actually, a frequency change of 20 MHz could be observed (Figure 5.22a). The slow change has a charging characteristic with a time constant of about 1000 s.

If a positive voltage step is applied to the quartz piezo, the cavity length increases instantaneously (as expected by the piezo effect, but only 180 kHz instead of 500 kHz), followed by a slow but higher decrease in cavity length. In the case of a negative voltage step, the cavity length decreases instantaneously, likewise followed by a further slow decrease in cavity length (Figure 5.22b). Figure 5.22c shows the behavior of the cavity when alternately applying a positive and a negative voltage. After the voltage change, an increase of cavity length can be observed, until after a certain time the decrease in cavity length starts again. If the voltage is changed before this inversion occurs, the beat frequency behaves like depicted in Figure 5.22d. A frequency jump in the direction expected by the piezo effect, but about a factor 4 smaller, can be observed, followed by a slow frequency change in the opposite direction.

Regarding the simpler cases where only a positive or a negative voltage is applied, it can be stated that the observed effect always decreases the cavity length, whether a positive or a negative voltage is applied. This tuning behavior can be qualitatively explained by electrostatic forces. It is assumed that there is a small gap between quartz piezo and mirror and between

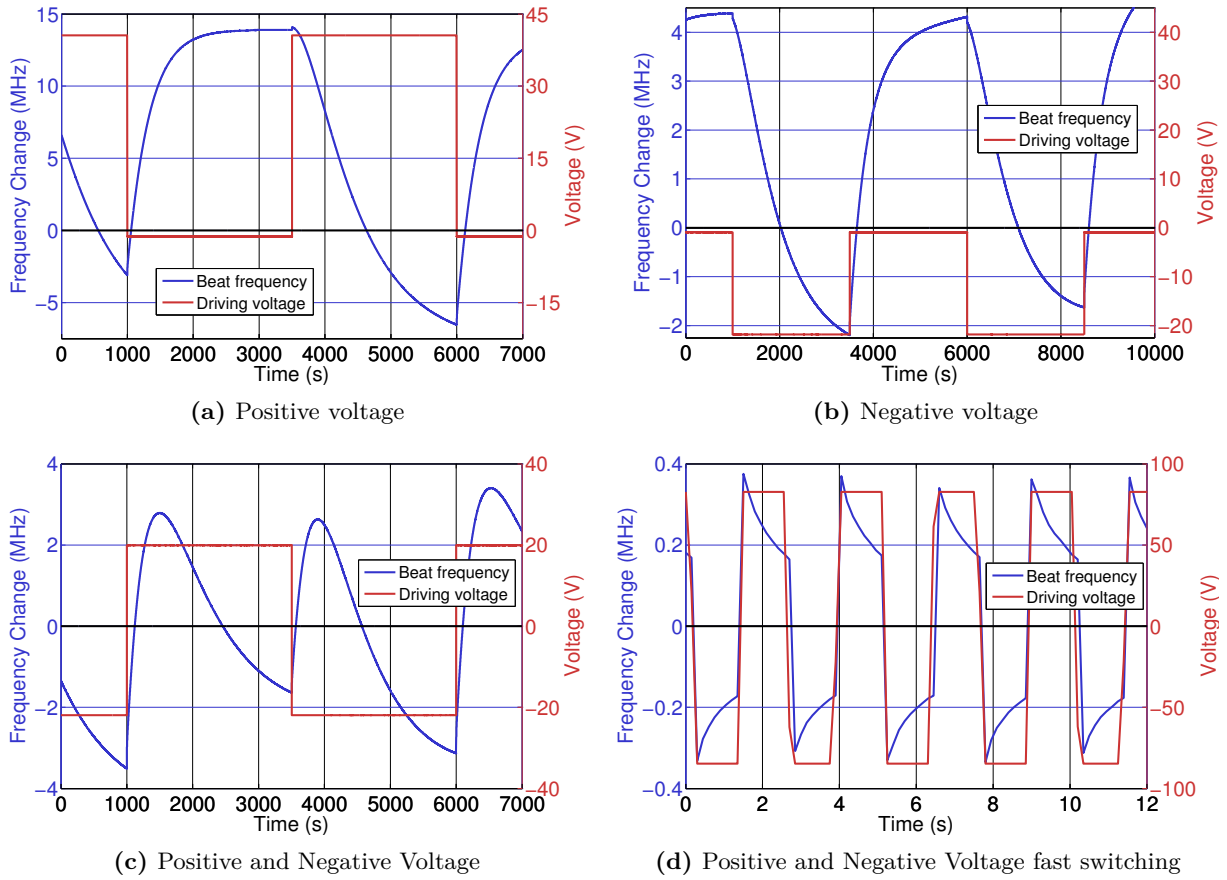


Figure 5.22.: Tuning behavior of the cavity with quartz actuator. A positive frequency change corresponds to an increase in cavity length.

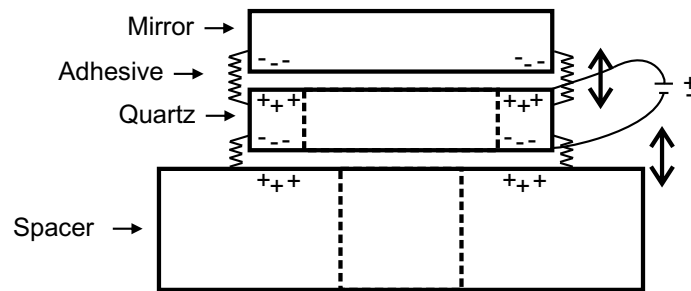


Figure 5.23.: Scheme of possible electrostatic effects of the cavity with quartz piezo. It is assumed that there are small gaps between actuator and mirror and actuator and spacer leading to a slow charging of mirror and spacer due to diffusion.

5. Characterization of the Piezo-Tunable Cavities

quartz piezo and spacer due to the applied gluing technique (Figure 5.23). The charged electrodes on the quartz piezo end faces produce an electric field which causes carriers in the mirror substrate to diffuse to the mirror surface and carriers in the spacer to diffuse to the spacer surface. The result is an attractive force between actuator and mirror and between actuator and spacer. When the gluing points between the surfaces are considered as springs, this force leads to a decrease of the cavity length according to Hooke's law.

It was tried to derive a quantitative description of this effect (appendix B), but the calculation could not be reconciled with the measurements. Since the estimations fail to describe the right order of magnitude of the observed effect, further investigations would be necessary to prove or disprove the assumption of an electro-static effect. However, since the observed effect is a rather unwanted effect, which is due to its slow tuning characteristics not suitable for tuning a cavity in a defined way, the effect was not further investigated.

The other cavities are presumably not affected by this effect, since the PZN-PT actuator has direct contact with the mirror and spacer surfaces, and since the electrodes of the PZT stack and PZT tube actuators are arranged differently: in the case of the PZT stack actuator due to its multilayer structure and in the case of the PZT tube actuator due to the usage of the transversal piezo effect.

5.4. Stabilization of the piezo-tunable cavity - use as transfer cavity

For the implementation of a piezo-tunable cavity in LISA, the pre-stabilization has to be combined with the arm-locking technique. It is planned to use the arm-locking error signal to adjust the reference frequency of the pre-stabilization cavity as it is shown in Figure 5.24a. To test the integration of a piezo-tunable cavity in such an external feedback loop, the length stability of the highly stable fused silica cavity (see Section 4.3.2) was actively transferred to the cavity with PZT stack actuator. This approach is quite similar to the widely used transfer cavity concept, where the stability of one laser is transferred to another using a piezo-tunable cavity [71, 72]. In such experiments stabilities up to 10^{-11} have been transferred [73], by locking the cavity to a reference laser and then stabilizing a target laser to this cavity. However, to our knowledge the concept has not yet been realized with highly stable references in the 10^{-15} range.

5.4.1. Implementation

The stability transfer was realized with a laser that was coupled to both the piezo-tunable cavity and the fused silica cavity (Figure 5.24b). First, the laser frequency was locked to the resonance of the tunable cavity using the PDH technique. Then, by applying the appropriate voltage to the incorporated piezo actuator, the cavity and thus the laser stabilized to this cavity was tuned to a resonance of the fused silica cavity. A PDH error signal from the fused silica cavity could be observed by sweeping the voltage applied to the piezo-tunable cavity. This error signal was finally used for stabilization of the length and thus of the resonance frequency of the tunable cavity. Both PDH locks are realized using the same modulation sidebands. For performing the piezo lock, the frequency separating filter described in the previous section was

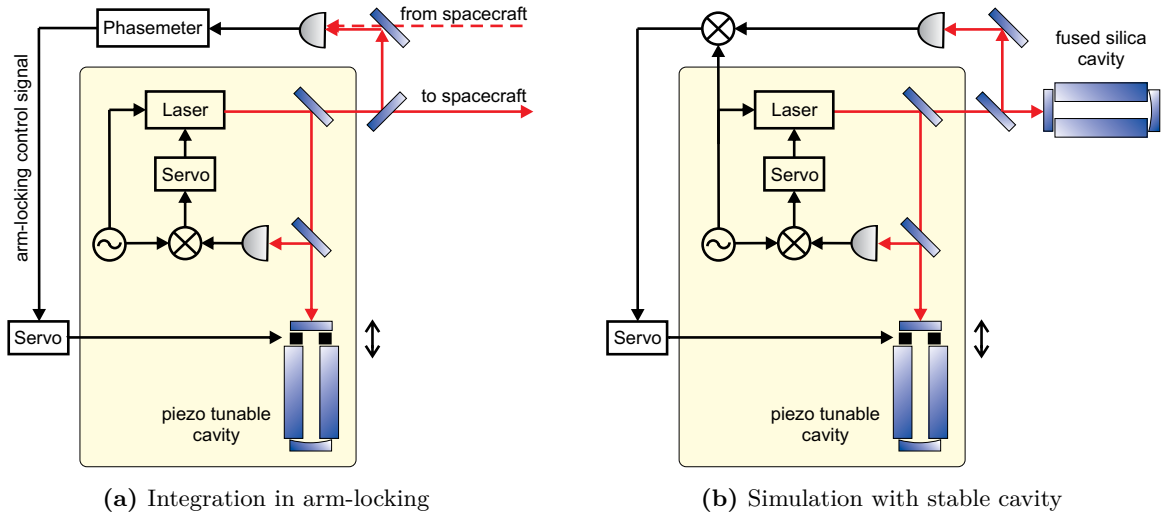


Figure 5.24.: Scheme of the stability transfer lock. The yellow box contains all elements that are needed for stabilizing the laser to the piezo-tunable cavity with a PDH lock.

5. Characterization of the Piezo-Tunable Cavities

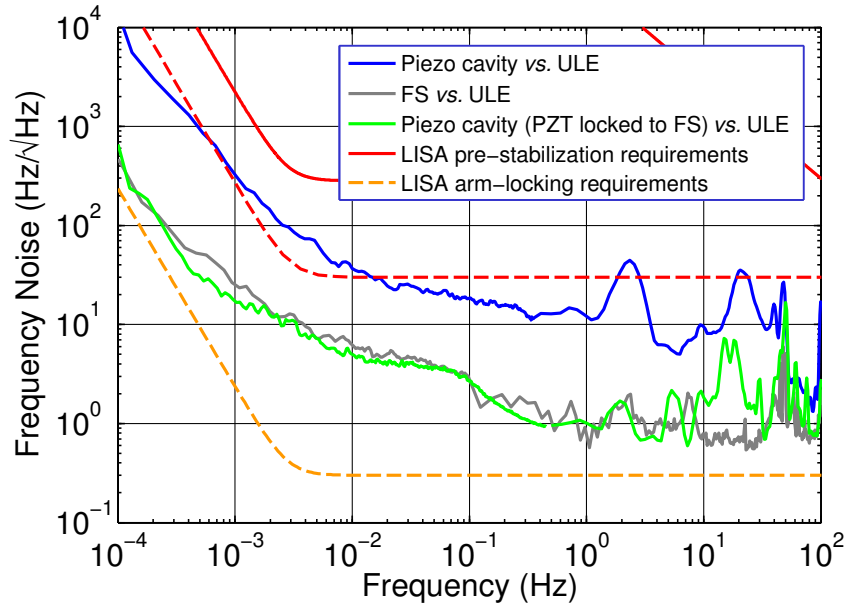


Figure 5.25.: Frequency noise of the externally stabilized piezo-tunable cavity. For comparison the frequency noise of the unstabilized tunable cavity and the fused silica (FS) reference are shown as well.

used. In this way the resonance frequency of the piezo-tunable cavity could be stabilized to the fused silica reference cavity with a lock bandwidth of 5 kHz, presumably limited by mechanical resonances of the piezo-tunable cavity. This lock bandwidth is sufficient, since the demands on the lock performance are quite low due to the good ‘free-running’ stability of the piezo-tunable cavity. Furthermore, it is above the 1 kHz tuning bandwidth required for LISA. Therefore, no further effort was made to increase the lock bandwidth. If required, this could be achieved by optimizing the lock performance and by shifting the mechanical resonance of the system to higher frequencies by using, e.g., smaller mirrors and actuators. It has already been shown that a lock bandwidth above 100 kHz is possible with piezo actuators [74].

5.4.2. Results

To determine the frequency noise of the stabilized piezo-tunable cavity, a beat measurement with a laser stabilized to the ULE cavity was performed. Figure 5.25 shows the frequency noise of the stabilized and non stabilized tunable cavity as well as the noise of the fused silica cavity. It is apparent that the frequency noise of the tunable cavity is reduced by about one order of magnitude by stabilization, so that the stability of the fused silica cavity is nearly completely transferred to the piezo-tunable cavity. The remaining differences in seismic noise result most likely from different measurement conditions.

As denoted in Figure 5.25 the frequency noise of the FS cavity is higher than the frequency noise requirements of the arm-locking signal. An even more stable reference would be needed to fully investigate the performance of piezo-tunable cavities for LISA arm-locking. The performed

experiment is thus not considered as complete demonstration that a piezo-tunable cavity can be integrated in the arm-locking feed back loop, but as strong evidence.

5.5. Conclusion

The performed measurements have shown that piezo-tunable cavities can be realized with frequency instabilities in the 10^{-15} range. The achieved instability of 7×10^{-15} at 1 s integration times is almost two orders of magnitude above the best results obtained with piezo-tunable cavities so far. Conti et al. measured an instability of 3.5×10^{-13} at 1 s [17], and Li et al. a laser linewidth in the kHz range [18]. The latter can be compared with the results obtained in this work using the relation $\Delta\nu = \pi S_\nu^2$ between laser linewidth $\Delta\nu$ and white frequency noise S_ν . The white frequency noise of the analyzed cavities is estimated to be $1 \text{ Hz}/\sqrt{\text{Hz}}$ which corresponds to a laser linewidth of $\sim 3 \text{ Hz}$.

The piezo-tunable cavities can be tuned over more than one free spectral range. The high voltage required for this tuning range can be filtered so that the frequency noise measured with the cavity with short circuited piezo actuator is only slightly increased. By applying a frequency separating filter, it is possible to apply fast frequency variations at the same time. Furthermore it has been shown that a piezo-tunable cavity can be integrated into an external feed back loop with a lock bandwidth of 5 kHz. It has thus been demonstrated that piezo-tunable cavities fulfill all the requirements for a tunable pre-stabilization for LISA.

Within the measurement precision, no limitation on the frequency stability arising from the intrinsic stability of the piezo actuators could be observed. Only the application of high voltages for a wide tuning range decrease the frequency stability. For this reason, all tested piezo materials seems to be well suited for a use in a piezo-tunable cavity.

6. Cavity with Prestressed Piezo Actuator

The piezo-tunable cavities presented in the previous chapters were built by just gluing one or two piezo actuators between mirrors and spacer of an optical cavity. Under laboratory conditions, they fulfill all the requirements given for a tunable pre-stabilization for LISA. The piezo-tunable cavity presented in this chapter addresses one important issue with respect to a space application. If a piezo-tunable cavity is to be used in a space mission, the high forces and vibrations that arise during the launch of such a mission have to be considered in the cavity design. A space version of a non-tunable cavity has already been developed [75], putting a focus on rigid mounting of the cavity and the optics. For a space version of a piezo-tunable cavity, it has additionally to be considered that the widely used actuator material PZT is a brittle ceramic, which cannot withstand high tensile or shear forces. For this reason, normally only prestressed actuators are used in space applications. Commercially available prestressed actuators use metal springs to load the actuator. This leads to inferior mechanical properties due to the larger size of these devices, as well as inferior thermal properties, due to the higher expansion coefficients of metals. Therefore, it is difficult to build highly stable cavities with commercially available prestressed actuators and a novel piezo-tunable cavity design was developed in this work. In this design, the piezo actuator is clamped between the cavity spacer parts themselves and is thus prestressed (Figures 6.1 and 6.2).

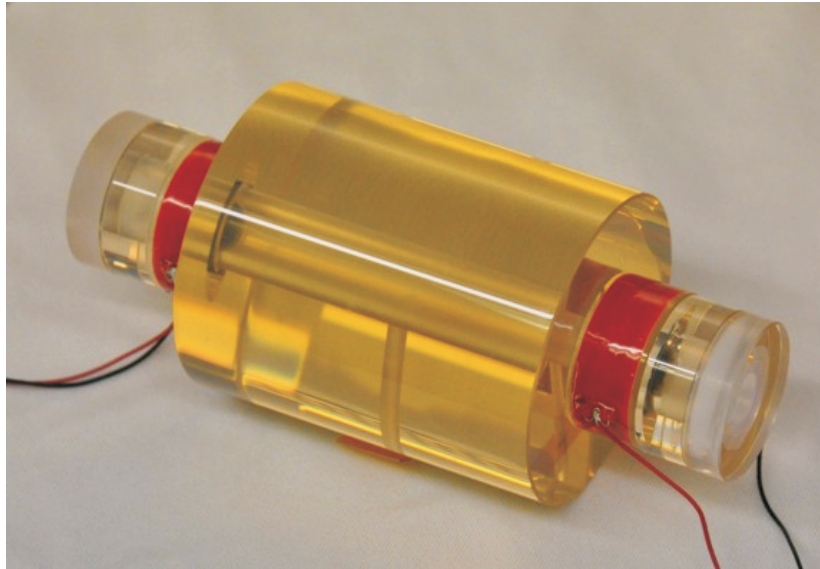


Figure 6.1.: Photograph of the cavity with prestressed piezo actuator.

6. Cavity with Prestressed Piezo Actuator

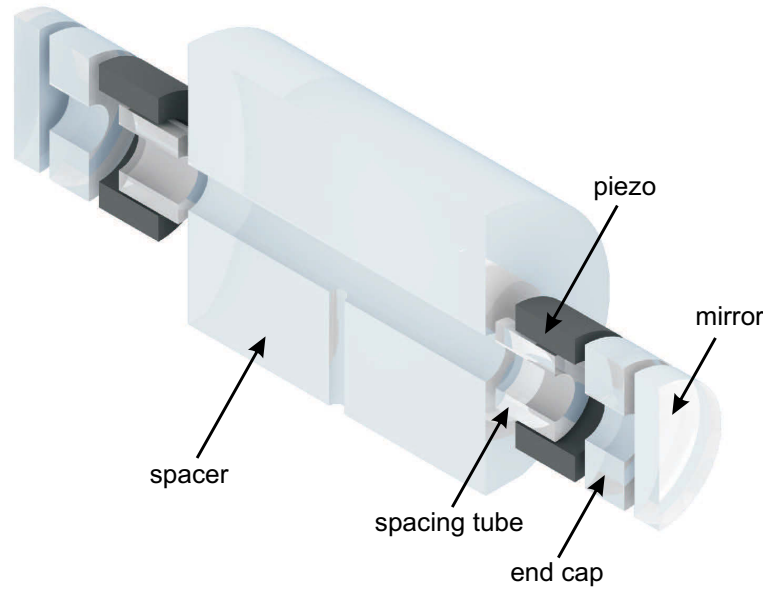


Figure 6.2.: Model of the cavity with prestressed piezo actuator (exploded view). The PZT stack actuators have an outer diameter of 25 mm and a length of 12 mm. The spacing tubes are $0.55\text{ }\mu\text{m}$ shorter than the actuators. They have an outer diameter of 15 mm and a wall thickness of 3.5 mm. The actuator surface has two small slots to enable evacuation of the hollow space between actuator and spacing tube.

The experiments presented in the following aim to investigate, if this kind of prestressing compromises the stability of a piezo-tunable cavity and if the LISA requirements on stability and tunability can be fulfilled with such a cavity. Tests of the space qualification were not part of this work.

6.1. Design

The cavity with prestressed actuator consists of a spacer, two spacing tubes, and two end caps made from Zerodur, as well as fused silica mirrors and PZT stack actuators (Figure 6.2). The relevant feature of the design is that the spacing tube lying inside the piezo actuator is $0.55\text{ }\mu\text{m}$ shorter than the piezo itself. When the spacing tube is tightly bonded to the spacer and the end cap while the piezo actuator is contracted by a continuously applied negative voltage, the actuator cannot expand to its old length after removal of this negative voltage and is thus prestressed. At the same time the spacing tube is slightly stretched and consequently subjected to tensile stress. Applying a positive voltage to the actuator to tune the cavity length, means further stretching the spacing tube and creating even higher tensile stress. Here, the double-sided design is helpful, since it allows a tuning range twice as high with the same stress. The spacer parts are joined together with hydroxide catalysis bonding, which has the advantage of a high bonding strength and a minor bond thickness $< 100\text{ nm}$. The mirrors are optically contacted

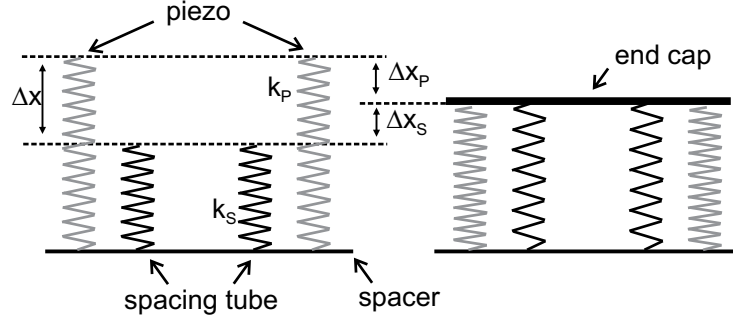


Figure 6.3.: Schematic of the prestressed piezo before (left) and after (right) attaching the end cap to the spacing tube. The outer springs (k_p) represent the piezo actuator and the inner two springs (k_s) represent the spacing tube.

to the spacer, which allows to detach them if needed. In the following some calculations of the created stress and simulations of the resulting deformation will be presented. More details on the assembly process as well as on the applied bonding technique will be given in Section 6.2.

6.1.1. Calculations

The applied PZT actuators have a stiffness of $k_p = 780 \text{ N}/\mu\text{m}$ (manufacturer data). The dimensions of the spacing tubes were chosen such that the resulting stiffness roughly equals the stiffness of the piezo actuator. With a length of $L_s = 12 \text{ mm}$, an outer diameter of 15 mm, and an inner diameter of 8 mm the stiffness can be calculated to

$$k_s = E_s \frac{A_s}{L_s} = 90 \text{ GPa} \frac{126 \text{ mm}^2}{12 \text{ mm}} = 948 \text{ N}/\mu\text{m}. \quad (6.1)$$

Since the piezo actuator is $\Delta x = 0.55 \mu\text{m}$ longer than the spacing tube, the attachment of the end cap leads to a compression of the actuator, as well as to an extension of the spacing tube (Figure 6.3). The actuator is compressed by Δx_p and the spacing tube is stretched by Δx_s until the elastic forces of both parts are equal

$$k_p \Delta x_p = k_s \Delta x_s. \quad (6.2)$$

With the relation $\Delta x_p + \Delta x_s = \Delta x$ the compression of the piezo actuator can be calculated to

$$\Delta x_p = \Delta x \frac{k_s}{k_p + k_s} = 0.3 \mu\text{m} \quad (6.3)$$

and the elongation of the spacing tube to

$$\Delta x_s = \Delta x \frac{k_p}{k_p + k_s} = 0.25 \mu\text{m}. \quad (6.4)$$

6. Cavity with Prestressed Piezo Actuator

Due to this strain, the piezo actuator is subjected to a prestress of $p_p = \Delta x_p k_p / A_p = 0.81$ MPa. For comparison, commercially available piezo actuators are typically prestressed with ~ 15 MPa. It was not aimed for a higher prestress, since this would subject higher tensile stress to the spacing tube. With the given dimensions, the tensile stress $p_s = \Delta x_s k_s / A_s = E_s \Delta x_s / L_s = 1.8$ MPa is well below the tensile strength of Zerodur, which is shown in recent measurement to be above 40 MPa [76]. The tensile stress increases, however, if the piezo is expanded to tune the cavity length. The maximum displacement of the piezo actuators at 1000 V is specified by the manufacturer to be $\Delta L_0 = 7.5 \mu\text{m}$. In accordance to equation (3.53), this maximum displacement is reduced by prestressing to

$$\Delta L = \Delta L_0 \frac{k_p}{k_p + k_s} = 3.4 \mu\text{m}. \quad (6.5)$$

By applying ~ 80 V at the two actuators, the cavity is tuned about a half wavelength ($0.532 \mu\text{m}$) which corresponds to a frequency change of one FSR (1.5 GHz). At this displacement the spacing tubes are subjected to a tensile stress of 3.9 MPa. The full tuning range of the two piezo actuators allows for a frequency tuning range of 19 GHz, which corresponds to more than 12 FSRs. At this maximum displacement the spacing tubes would be stressed with 27.3 MPa, which is still below the tensile strength. However, it has to be tested if the bond can withstand such high tensile forces (see Section 6.2). Furthermore, it should be tested if the relatively low level of prestressing protects the actuator sufficiently against vibrations. If it turns out that higher prestress is required, the stiffness of the spacing tube has to be increased by changing its dimensions. This results, however, also in a lower tuning range. The presented prestressing is considered as a good compromise between tuning range and prestress to perform first investigations on feasibility and stability of the presented cavity design.

6.1.2. Simulations

The previous calculations were done with the approximation of rigid end caps that do not bend under stress. To get an impression of the real deformation of the system, the cavity with prestressed piezo actuators was analyzed with a finite element method using the program COMSOL Multiphysics. Figure 6.4a shows a deformation plot of the cavity without applied voltage, the displacement and distortion result from the prestressing. Figure 6.4b gives a closer look on the deformation of the mirror surface. The displacement along the line marked in Figure 6.4a is plotted for different thickness of the end cap. As can be expected, the deformation decreases with increasing end cap thickness.

The deformation or the mirror flatness can be compared with the required flatness for optically contacting and hydroxide catalysis bonding, which is $\lambda/10 = 63$ nm. To be able to optically contact the mirrors to the spacer assembly, the deformation has to be below this value. Without applied voltage, this flatness is achieved with all presented end cap thicknesses. However, when the piezo actuators are expanded to tune the cavity length, the deformation increases further. Tuning of one FSR doubles the deformation and the required flatness is no longer given for all end cap thicknesses.

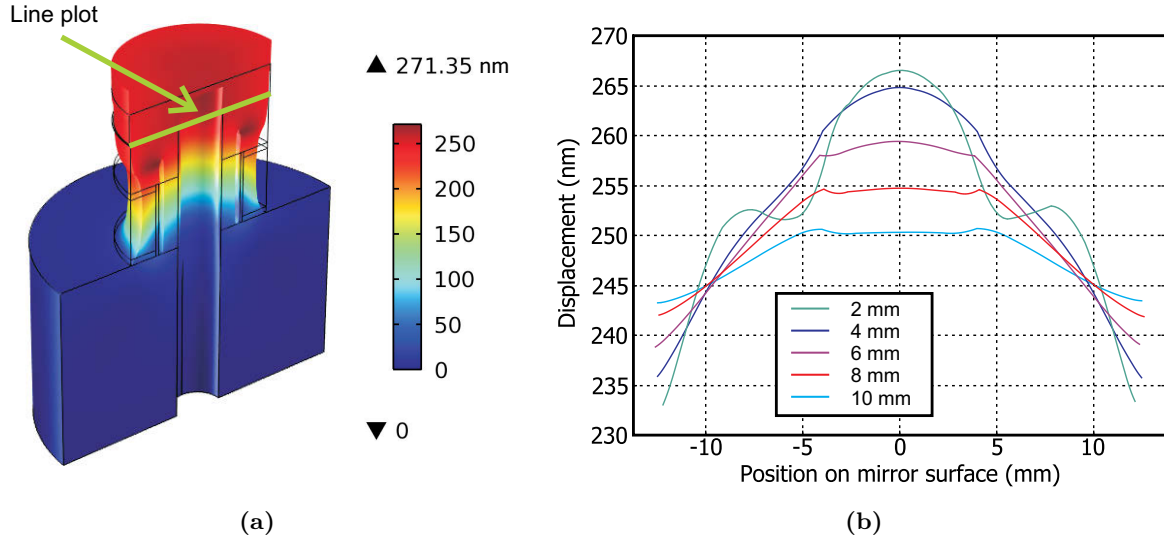


Figure 6.4.: Deformation of the cavity with prestressed piezo actuator simulated with COMSOL. Left: 3-D plot of the deformation and displacement of the cavity due to the prestressing. Right: Deformation of the mirror surface with different end cap thicknesses from 2 mm to 10 mm. The plot shows the displacement in direction of the cavity axis along the line marked in the left figure.

The deformation of the mirror could also be of interest with respect to modifications in the cavity mode geometry. These modifications could change the matching of the Gaussian laser beam to the cavity modes and thus change the incoupling efficiency. This would lead to intensity changes in the cavity and thus to frequency changes of a laser stabilized to this cavity as described in Section 4.2.1.

Regarding these two aspects, a high thickness of the end caps would be preferable. The disadvantage of thicker end caps is a higher cavity length with a reduced mechanical stability and an increased sensitivity to vibrations. As a compromise between small deformations of the end cap and good mechanical stability of the cavity, a thickness of 8 mm was chosen for the end caps.

6.2. Assembly

The spacer parts of the cavity were manufactured by Precision Light Wave, LCC. The PZT stack actuators (Physical Instruments, Pica Thru) had to be modified to achieve the required length difference of $0.55\text{ }\mu\text{m}$. The standard ceramic end faces of the actuators cannot be machined to the demanded precision, so 1 mm thick fused silica rings were glued to them (Norland, NOA61). In contrast to PZT, fused silica and Zerodur can be polished to a very low roughness and flatness.

The cavity spacer with the prestressed piezo actuators was assembled using hydroxide-catalysis bonding [77, 78]. Hydroxide-catalysis bonding can be used to join highly even surfaces (flatness $\leq \lambda/10$) by creating silicate like networks between them. The method was developed for silicate based materials, but has also been successfully applied for materials like silicon carbide and sapphire. The bonding process is initialized by bringing a bonding solution such as NaOH between two polished and clean surfaces. The hydroxide ions in the solution catalyze hydration and dehydration of silicate oxide. This leads to a polymerization process which forms rigid bonds between the surfaces (see for example [79]). This bonding technique has the advantage of a high bonding strength and a minor bond thickness $< 100\text{ nm}$. The minor bond thickness is especially important for this assembly, because the precisely machined length difference of $0.55\text{ }\mu\text{m}$ between spacing tube and piezo actuator would be corrupted by typical adhesive layer thicknesses of at least several micrometers. The bonding strength is expected to be high, since the bonded parts build a quasi-monolithic object. Various tests of the bonding strength have been performed obtaining very different results [80]. The measured breaking stress ranges from a few MPa to more than 40 MPa [81] depending on, for example, the applied bonding solution, the curing time, the cleanness of the surfaces, and the applied test method.

In the following the assembly process of the cavity with prestressed actuators will be described in detail. Here already, it shall be mentioned that the assembly process could only be implemented as planned for one piezo actuator. For the other actuator problems arose during bonding and the desired prestressing could only be achieved by the additional use of adhesive. Details on this can be found in appendix C.

The assembly of the cavities was done in a clean room since any pollution of the polished surfaces would prevent proper bonding. The single steps of the bonding procedure are illustrated in Figure 6.5. After bonding the spacing tube and the actuator to the spacer, a negative voltage of -200 V was applied to the piezo actuator leading to a shortening of the actuator of $1.4\text{ }\mu\text{m}$ (measured with an atomic force microscope). The actuator is thus $0.85\text{ }\mu\text{m}$ shorter than the spacing tube and the end cap can be bonded to the spacing tube without having contact to the piezo actuator. The bond was cured for two weeks while the negative voltage was continuously applied to the actuator. After removal of the negative voltage the piezo actuator presses against the end cap and thus slightly stretches the spacing tube (Section 6.1.1). In this state the cavity mirror was optically contacted to the end cap.

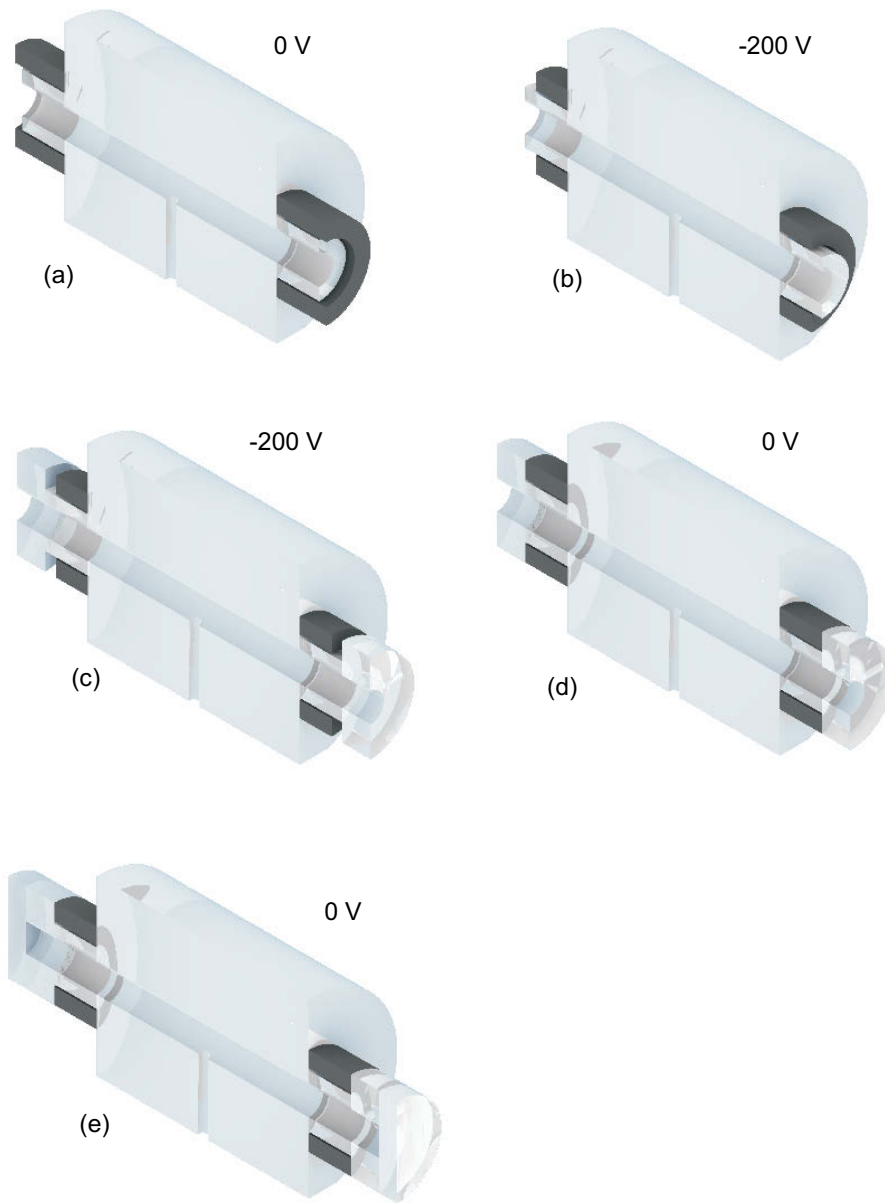


Figure 6.5.: Bonding procedure of the cavity with prestressed actuators. At first, the spacing tubes and actuators were bonded to the spacer (a). Then, the piezo actuators were contracted by applying a negative voltage (b). With this negative voltage the spacing tubes are slightly longer ($0.85\ \mu\text{m}$) than the piezo actuators and the end caps could be bonded to the spacing tubes (c). After removal of the negative voltage the actuators cannot expand to their original length and are thus prestressed while the spacing tube is stretched (d). At last, the mirrors were optically contacted to the end caps (e).

6.3. Measurements

The cavity with prestressed actuators was installed in the same setup as the other tested cavities with the only modification that a copper V-mount was used to support the cavity. As for the other piezo-tunable cavities, cavity properties, frequency noise and tuning behavior was analyzed. In addition, a modified locking scheme modulating the cavity instead of the laser was tested.

6.3.1. Cavity properties

For the cavity with prestressed piezo actuators, some cavity properties like FSR and linewidth were measured with the same methods as described in Section 5.1. The results are listed in Table 6.1. The cavity has relatively low losses, probably due to the assembly in clean room conditions, and thus benefits from a low cavity linewidth and a high finesse.

FSR (GHz)	L_C (mm)	Finesse	Γ_ν (kHz)	coupling efficiency	losses (ppm)
1.493	100.469	183 000	8.2	70%	17

Table 6.1.: Properties of the cavity with prestressed piezo actuators.

The mechanical resonance frequencies of the cavity with prestressed piezo actuators were measured, by applying a frequency sweep with an amplitude of 100 mV to one actuator and measuring the frequency response of the other actuator using a network analyzer. The resonance frequencies are of interest when a piezo-tunable cavity is integrated in a stabilization loop, since the control bandwidth is limited by the lowest resonance. The lowest resonance frequency of the piezo-tunable cavities presented in the previous chapters can be estimated using formula (3.54). The attachment of a load (mirror) shifts the resonance frequency of the piezo actuator to lower frequencies. The resonance frequency of the cavity with the prestressed actuators could not be estimated by calculations due to the more complex configuration and was thus determined experimentally. The mere piezo resonance is specified with 110 kHz. As can be seen in Figure 6.6, the first resonance for the cavity assembly appears at 27 kHz, though it has to be considered that eventually not all vibrational modes can be excited and measured by the applied method.

6.3.2. Frequency noise

As for the other piezo-tunable cavities, the noise performance of the cavity with prestressed actuators was first analyzed with short circuited piezo actuators. Figure 6.7 shows the respective ASD and Allan deviation in comparison to the performance of the cavity with the PZN-PT actuator. This cavity was singled out for comparison, since measurements were performed with this cavity while it was supported by the V-mount. As shown in Figure 5.13f, there are slight differences in the frequency noise due to the modified mounting. The cavity with prestressed piezo actuators has almost the same white and flicker noise as the cavity with PZN-PT actuator, even though it consists of another spacer and another set of mirrors, and it has a different thermal

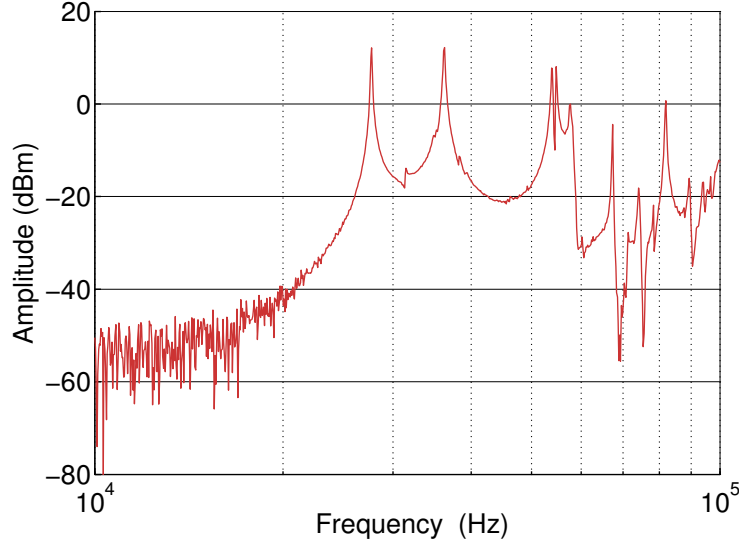


Figure 6.6.: Mechanical resonances of the cavity with prestressed actuators.

noise level ($\sigma_{\text{tn}}/\nu_0 = 1 \times 10^{-15}$). This is a further evidence that rather the experimental setup than the piezo-tunable cavities limits the frequency stability. There are, however, differences in the random walk noise of the cavity with prestressed actuators which is increased by a factor of about five. This could be caused by relaxations of the cavity materials, which have a relatively high internal stress due to the prestressed configuration.

6.3.3. Tuning of the cavity with prestressed piezo actuator

The tuning coefficients of the cavity with prestressed actuators was measured by applying a voltage to the piezo actuators. The actuator at the successfully hydroxide bonded side of the cavity has a tuning coefficient of 7.9 MHz/V, for the other actuator a tuning coefficient of 9 MHz/V was measured. This corresponds to a displacement of 2.8 nm/V and 3.2 nm/V, which is slightly below the calculated value of 3.4 nm/V (equation (6.5)). The different values for the two actuators could arise from the use of adhesive at the one side. The adhesive may act as an additional spring in the actuator-spacing tube spring system (Figure 6.3) and, thus, change the values for piezo actuator and spacing tube stiffness that have to be inserted in equation (6.5). It is also possible that the actuators had already a different tuning range in the non prestressed state due to manufacturing variations or that a slight depoling of the piezo ceramics occurred during the bonding procedure. In any case, the cavity with prestressed piezo actuator on the whole has a tuning coefficient of 16.9 MHz/V. Thus, for tuning the cavity by one FSR a voltage of 88.8 V is required.

By applying a voltage of 100 V to both actuators, it was demonstrated that the cavity can be tuned over more than one FSR while, in accordance with the calculations, material and bond can bear the arising stress without failure.

6. Cavity with Prestressed Piezo Actuator

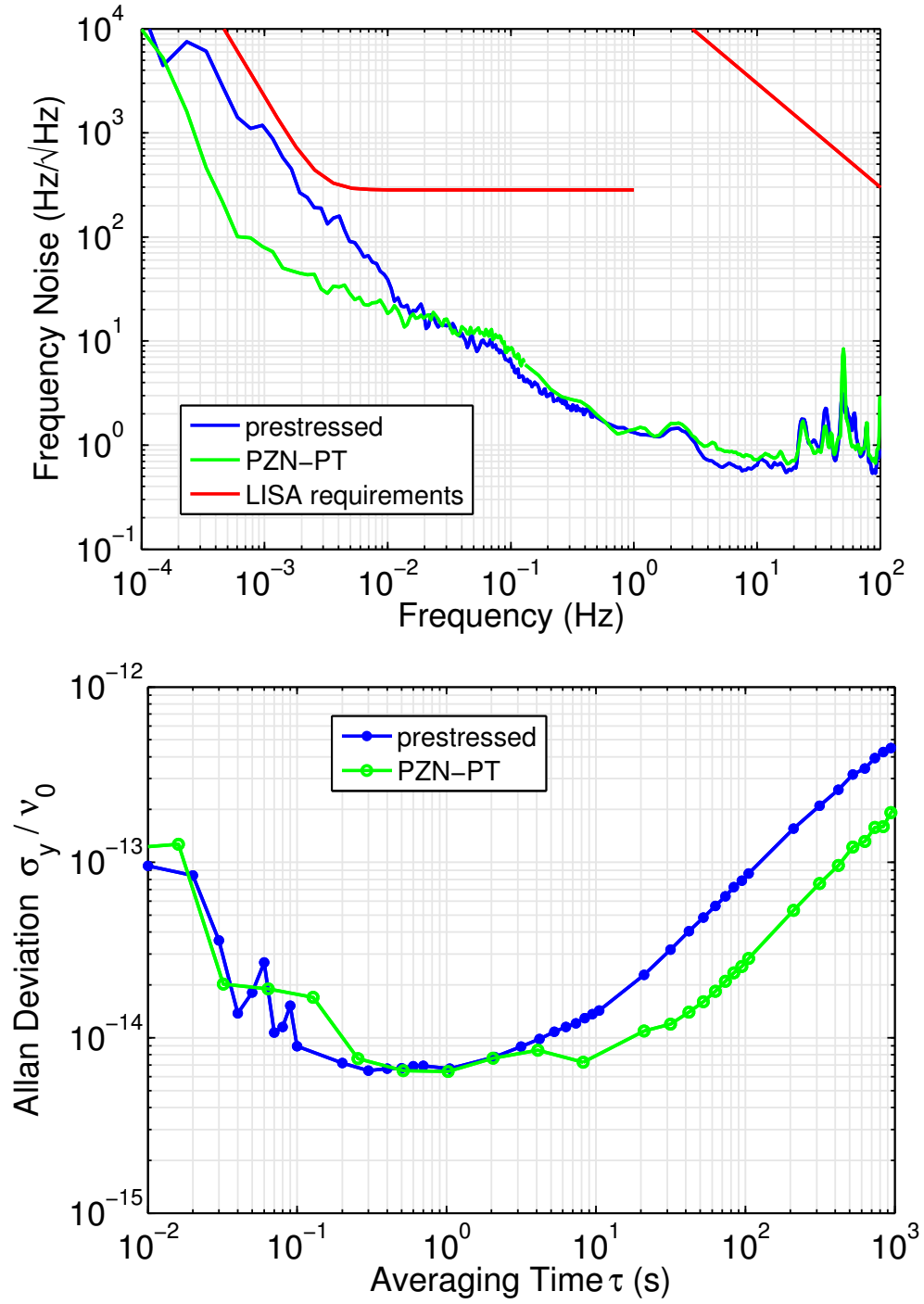


Figure 6.7.: ASD and relative Allan deviation of the cavity with prestressed actuators in comparison to the cavity with PZN-PT actuator measured with short circuited piezo actuators. Both cavities were mounted on V-mounts during these measurements, which explains the difference in the ASD of the cavity with PZN-PT actuator in comparison to that shown in figure 5.4.

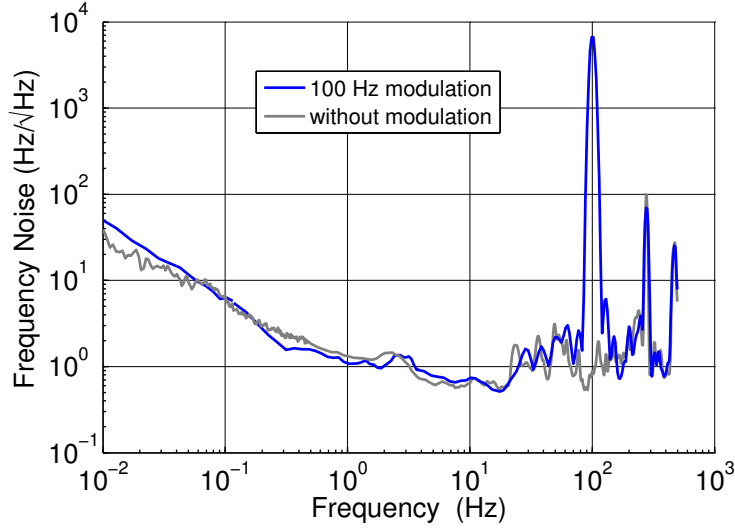


Figure 6.8.: ASD of the cavity with prestressed piezo actuators while modulated with 100 Hz. Except for the peak at 100 Hz the spectrum shows no alteration.

Hysteresis

Hysteresis measurements with the cavity with prestressed piezo actuators reveal a maximum opening in the voltage frequency curve of 4.3% when a maximum voltage of 43 V is applied, and a maximum opening of 6% when a maximum voltage of 79 V is applied. These values are slightly higher than the values measured for the cavity with non prestressed PZT stack actuator (Table 5.5). This does not accord with investigations that showed a decrease of hysteresis with increasing stress [82]. However, the applied stress of 0.8 MPa is rather small and it is assumed that the increased degree of hysteresis arises from standard manufacturing variations.

Influence of a varying piezo driving voltage

For an application in LISA only slow changes of the piezo driving voltage are required. As shown in Section 5.3.3, slow changes do not degrade the frequency stability of a piezo-tunable cavity. For other applications it could be interesting to know whether also a fast changing piezo driving voltage does not degrade the stability. For this purpose, the frequency noise of the cavity with prestressed piezo actuator was measured while different sinusoidal voltages between 1 Hz and 120 kHz were applied to the actuators. The signals with amplitudes of up to 4 mV, which cause frequency changes of the cavity resonance of up to 70 kHz, were generated with a HP 33120A. Such sinusoidal signals generate forces that increase quadratically with the frequency (equation (3.55)). Therefore, prestressed piezo actuators are recommended for dynamic operation and the presented measurements were performed with the cavity with prestressed actuators only.

As might be expected, the measured frequency noise does not differ from the noise of the unmodulated cavity, when the modulation frequency is higher than the lock bandwidth of the PDH lock (~ 30 kHz). When the modulation frequency is lower than the lock bandwidth, the noise spectrum has a peak at the modulation frequency, while the remaining spectrum shows no

6. Cavity with Prestressed Piezo Actuator

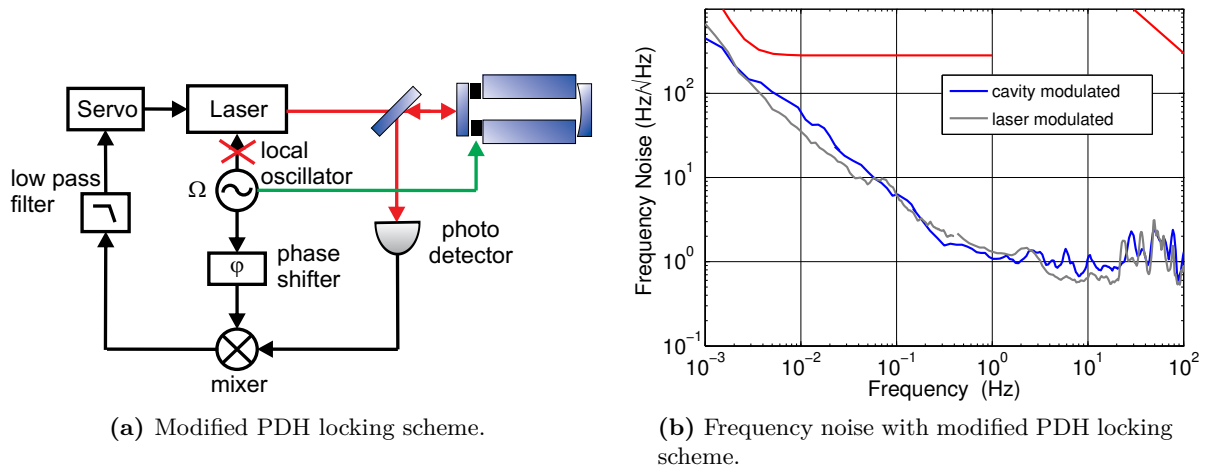


Figure 6.9.: Layout of the modified locking scheme and ASD of the cavity with prestressed piezo actuator stabilized accordingly. The scheme employs modulation of the cavity instead of modulation of the laser.

alteration as can be seen in Figure 6.8. Piezo-tunable cavities are thus also suited for application where a fast varying piezo supply voltage is required.

6.3.4. PDH locking with modulated cavity

A piezoelectrically tunable cavity can be used to implement a modified PDH locking scheme which employs an unmodulated laser and a modulated cavity (Figure 6.9a). To test this approach the cavity was modulated with 122.37 kHz, where the prestressed piezo actuator has a mechanical resonance. The laser was tuned to a cavity resonance and the emerging error signal was observed. The amplitude of the piezo modulation was adapted such that the error signal slope reached its maximum size, which was given with 3.8 mV.

The frequency noise of a laser stabilized this way is shown in Figure 6.9b. It is apparent that this kind of stabilization causes no increase in frequency noise compared to the usual stabilization scheme. The advantage of this modified locking scheme is the availability of a tunable stable laser without modulation sidebands, which otherwise would only be possible by using an external modulator. This could also be an interesting option for LISA, where the laser modulation for a cavity stabilization is otherwise done using an electro optical modulator. In a space mission it is favorable to use as few parts as possible to minimize the risk of failures. The modified locking scheme could also be helpful when the frequency stability of a laser stabilized to a cavity is limited by parasitic resonators or RAM. Both effects are not present with an unmodulated laser. The performed measurement is thus also an independent proof that the observed limitation of the setup is not due to parasitic resonators or RAM.

6.4. Conclusion

A novel type of piezo-tunable cavity, where the piezo actuators are prestressed between the cavity spacer elements was realized. The cavity can be tuned over more than one free spectral range and has a relative frequency instability below 1×10^{-14} at integration times from 0.1 s to 3 s. It shows no significant differences to the performance of the piezo-tunable cavities with non prestressed actuators. Thus, the prestressed actuators do not limit the frequency stability. Only the slightly increased frequency noise in the low frequency range (< 10 MHz) could arise from the internal stress due to the prestressing.

Under laboratory conditions, the cavity with prestressed actuators fulfills all the requirements that are given for a tunable pre-stabilization for LISA. Whether the applied prestressing is indeed suited for the high vibrations that arise during the launch of a space mission, has to be tested.

7. Summary and Outlook

Within this thesis, different types of piezo-tunable cavities have been built and thoroughly analyzed. The experimental investigations show that a frequency noise below $30 \text{ Hz}/\sqrt{\text{Hz}}$ for frequencies $> 4 \text{ mHz}$ and a relative frequency instability of 7×10^{-15} at integration times from 0.3 s to 8 s can be achieved with piezo-tunable cavities (Section 5.2.2). This is the best result obtained with cavities incorporating a piezo actuator so far and the performance is most likely even not yet limited by the use of a piezo actuator. Accordingly, no significant differences in frequency stability of the cavities with PZT stack, PZT tube or PZN-PT actuator could be observed within the measurement precision. A couple of theoretical investigations have been made to analyze the influence of a piezo actuator on the performance of a cavity. They reveal that the intrinsic stability of piezo-tunable cavities is only slightly inferior to that of rigid cavities (Section 4.2).

The cavities can be tuned over more than one free spectral range ($> 1.5 \text{ GHz}$), so that the laser can be stabilized to any frequency of interest (Section 5.3.1). For such a broad tuning range a high voltage power supply is required, which needs to be filtered to prevent a substantial increase of the frequency noise and to allow a noise performance still fulfilling the LISA requirements. Fast tuning of the cavities without increase in frequency noise is possible with a tuning range of several 10 MHz. To combine a high tuning range with a fast frequency modulation, a frequency separating filter was applied (Section 5.3.2). In addition, it was demonstrated that the piezo-tunable cavities can be stabilized to a more stable reference with a lock bandwidth of 5 kHz (Section 5.4). The transferred instability of 1×10^{-15} is 4 orders of magnitude lower than the instability transferred in previous such experiments. Furthermore, the piezo-tunable cavities were used to implement a modified PDH locking scheme where the cavity is modulated instead of the laser (Section 6.3.4). With this kind of stabilization, that is insensitive to disturbing effects arising from parasitic resonators or RAM, the same frequency stability could be achieved.

Application in LISA

Piezo-tunable cavities fulfill all the requirements given for a tunable pre-stabilization for LISA. Since a piezo-tunable cavity is most likely the simplest implementation of such a tunable reference, it seems especially suited for a space mission, where low complexity is preferred to avoid failures. If a piezo-tunable cavity is chosen to be implemented in LISA, the next steps would be to build a space qualified version of a piezo-tunable cavity and to perform the relevant vibration and stress tests. One step towards a space qualified version has already been made by building a piezo-tunable cavity where the piezo is prestressed by the cavity spacer components to handle high forces (Chapter 6). It shows a similar noise performance and tuning properties as the piezo-tunable cavities without prestressing and is thus likewise suited for LISA.

7. Summary and Outlook

Piezo-tunable cavities for other applications

A highly stable piezo-tunable cavity is not only useful for an application in LISA. There are several experiments that need a stable as well as tunable laser such as high resolution spectroscopy, laser cooling experiments, or coherent optical communication systems. Especially in the latter application, a high linearity of the tunable laser is important [35, 83]. Typical non-linearities of a piezo-tunable cavity such as hysteresis and creep can, thus, not be neglected like in the feed back configuration applied in LISA. In this case, extensive modeling of the non-linear behavior would be necessary and it should be investigated how well the existing models (e.g. [84, 85]) can be adapted to a piezo-tunable cavity and how severe the remaining uncertainties are.

Piezo-tunable cavities could also find application in intra cavity spectroscopy. In frequency references based on intra cavity spectroscopy of molecular or atomic gases, the applied cavity has to be tuned (and locked) to the optical transition of interest [86–88]. The presented cavity with prestressed actuator seems to be well suited for this purpose. In particular, it features a clean, hermetically sealable, chemically inert intra cavity volume. This is of advantage to maintain the purity of the spectroscopic gas especially for reactive species. At the same time the piezo actuator is protected from corrosive gases and the danger of electrical flash overs at unfavorable pressures is avoided. The cavity with prestressed piezo actuator is already equipped with a polished cut out at the vent hole, which allows to bond a capillary to the hole and fill the cavity with clean gas.

Conclusion

So far, it has been widely assumed, that highly stable tunable cavities cannot be realized by using piezo actuators to define the cavity length. It was expected that the noise of the piezo element would substantially degrade the performance. With this work, this could be proven wrong by realizing piezo-tunable cavities with a relative frequency instability below 1×10^{-14} , which is only one to two orders of magnitude above the instability of the best cavity stabilized lasers and still not limited by the piezo actuator.

A. Noise and Stability Estimations

Amplitude and power spectral density

To find a repeating pattern in a time dependent signal $y(t)$ the autocorrelation function

$$R(\tau) = \langle y(t)y(t+\tau) \rangle \quad (\text{A.1})$$

can be applied. The Fourier transform of the autocorrelation function

$$S_y^2(f) = \int_0^\infty R(\tau) \exp(-i2\pi f\tau) d\tau \quad (\text{A.2})$$

is called spectral density or power spectral density. It gives information about the signal noise in an infinitesimal frequency band.

There exist different methods for estimating the power spectrum of a time series. M.S. Bartlett proposed to split the dataset into n segments of equal lengths, then build the Fourier transform of each segment and average the result for all n segments. P.D. Welch expanded this model by allowing overlapping segments as well as that a window function is applied to the segments.

For the noise spectra presented in this thesis the LPSD method (Logarithmic frequency axis Power Spectral Density) [89] was used, which is a further extension of the Welch method adequate for long time series plotted on a logarithmic frequency axis. This method adjusts the frequency resolution for every Fourier frequency to obtain more averages at higher frequencies.

The noise spectra presented in this thesis are displayed as amplitude spectral densities (ASD) which are obtained by calculating the root square of the power spectral density. Furthermore a drift in the time series is removed prior to each calculation.

Allan deviation and variance

The Allan variance is used to describe the stability of an oscillator in the time domain. It is calculated using a two-point variance of samples averaged over a time span τ . To determine the Allan variance at an integration time τ , the dataset is split into samples of the same length τ and the average over each sample is taken according to

$$\bar{y}_k = \frac{1}{\tau} \int_{t_k}^{t_k+\tau} y(t) dt. \quad (\text{A.3})$$

A. Noise and Stability Estimations

Then the variance of respectively two adjacent samples is calculated and finally the average over all such obtained variance is built:

$$\sigma_A^2(\tau) = \frac{1}{2} \langle (\bar{y}_{k+1} - \bar{y}_k)^2 \rangle \quad (\text{A.4})$$

$$= \frac{1}{2(M-1)} \sum_{k=1}^{M-1} (\bar{y}_{k+1} - \bar{y}_k)^2. \quad (\text{A.5})$$

Throughout this thesis the frequency stability is presented as Allan deviation which is the square root of the Allan variance. For the calculation of the Allan variance a drift was removed from the time series. To obtain the relative frequency instability the calculated Allan deviation is always divided by the laser frequency (282 THz).

For the accurate calculation of the Allan deviation a measurement without dead-time is assumed. For the measurements with the SRS counter this is not given. The typical sampling rate of 1 s implicates a dead-time of 50 ms so that the real loop time is 1050 ms. Hence, small errors in the calculation of the Allan deviation can be expected.

Noise types

When the ASD and Allan deviation are plotted in a double logarithmic scale the typical noise types can be described by straight lines with a characteristic slope. The slopes can thus be used to determine, which type of noise is limiting in a certain frequency range or integration time. The slopes of the most common noise types are listed in Table A.1. To learn more about how the noise types can be converted from the frequency into the time domain see for example [90].

noise type	ASD	Allan deviation
white	0	-1/2
flicker	-1/2	0
random walk	-1	1/2

Table A.1.: Slopes of the different noise types in a double logarithmic plot of ASD and Allan deviation.

B. Electrostatic Effect of the Quartz Cavity

In Chapter 5 the tuning behavior of the quartz cavity (Figure 5.22) was qualitatively explained by electrostatic effects using the assumption that small gaps are between mirror and spacer and actuator and spacer (Figure 5.23). Here a quantitative description of the effect is tried to be given.

If the quartz piezo is driven with 20 V, the electrodes on the quartz end faces are charged with $Q_P = C_P U = 5 \text{ pF} \cdot 20 \text{ V} = 100 \text{ pC}$. The resulting electric field can be approximated by

$$E_P = \frac{Q_P}{2\epsilon_0 A_P} = 1.9 \times 10^4 \text{ V/m}, \quad (\text{B.1})$$

where $\epsilon_0 = 8.85 \times 10^{-12} \text{ As/Vm}$ is the electric constant and $A_P = 3 \text{ cm}^2$ the size of the electrodes. The electric field causes diffusion processes in the mirror glass material. Charge carriers move to the surface until the inner electric field, which builds up due to the charge separation, equals the external electric field

$$E_P = E_M = \frac{Q_M}{2\epsilon\epsilon_0 A_M}. \quad (\text{B.2})$$

A_M is the area on the mirror surface which is exposed to the electric field and is approximated by $A_M = A_P$. The maximum surface charge is thus

$$Q_M^0 = 2\epsilon\epsilon_0 A_M E_P = 370 \text{ pC}, \quad (\text{B.3})$$

using $\epsilon = 3.7$ for fused silica. This results in a maximum attractive force of $F = E_P Q_M^0 = 7.2 \times 10^{-6} \text{ N}$.

The force leads to a decrease of the cavity length, which can be calculated by considering the gluing points between the two surfaces as springs with a spring constant of

$$D = \frac{Y \cdot A}{L} = 50\,000 \text{ N/m}. \quad (\text{B.4})$$

$Y = 100 \text{ MPa}$ is the Young modulus of the adhesive. The length L of the gluing bridges was estimated to 2 mm and the cross section A to 1 mm^2 . With Newtons law $F = 3 D \Delta L$ (the factor three arises from the three gluing springs) and using the above calculated attractive force, the length change can be calculated to $\Delta L = 48 \text{ pm}$ which corresponds to $\Delta\nu = 120 \text{ kHz}$. Considering that the cavity is assembled with four gluing junctions and the effect arises at all junctions the complete frequency change would be $\Delta\nu = 480 \text{ kHz}$. This is more than one order of magnitude below the measured frequency change of about 7 MHz (Figures 5.22b and 5.22c).

In addition to the amplitude, also the time constant of the effect was tried to be calculated. The time constant of the diffusion process is connected with the specific resistance of fused silica.

B. Electrostatic Effect of the Quartz Cavity

The diffusion current is calculated by ohm's law $j = \sigma E = E/\rho$, where j is the current density, σ the specific conductance and ρ the specific resistance. It follows

$$\dot{Q} = I(t) = j(t)A = \frac{E(t)}{\rho}A = \frac{A}{\rho}(E_0 - \frac{Q(t)}{2\epsilon\epsilon_0 A}). \quad (\text{B.5})$$

This differential equation is solved by

$$Q(t) = Q_0(1 - e^{-\frac{t}{\tau}}), \quad (\text{B.6})$$

with $\tau = 2\epsilon\epsilon_0\rho$. The shown graphs have a time constant of about 1000 s, which corresponds to a specific resistance of $1 \times 10^{13} \Omega\text{m}$. Manufacturer specification give a value of $1 \times 10^{16} \Omega\text{m}$ at room temperature (see for example Heraeus Quartzglas, electrical properties). The discrepancy can only partly be explained by the fact that the measurement where not taken at room temperature but at 40 °C.

The quantitative estimations thus disagree with the assumption of electrostatic forces causing the observed effect. Therefore, further investigations would be necessary to prove or disprove the assumption. However, since the observed effect is a rather unwanted effect, which is due to its slow tuning characteristics not suitable for tuning a cavity in a defined way, the effect was not further investigated.

C. Assembly of the prestressed cavity

As mentioned in Chapter 6 the bonding of the prestressed cavity worked only at one side of the assembly as expected. At the other side, which was the side assembled first, the end cap bonded only partly to the spacing tube. The reasons for this and the measures taken to obtain nevertheless a useful device are described in the following.

It is assumed that the reason for the imperfect bonding is an impurity between piezo actuator and end cap as sketched in Figure C.1. The impurity prevented the end cap from bonding completely to the spacing tube. The parts could not be detached again without destroying the surface quality necessary for hydroxide catalysis bonding. Thus, the remaining gap was filled with adhesive (Polytec EP 601) to attach the entire end cap to the spacing tube. However, in this configuration, only a part of the piezo actuator was in contact with the end cap after removal of the negative voltage, that was applied to the piezo actuator during bonding. The piezo actuator was thus not uniformly prestressed. The small gap can be identified by the interference pattern that is visible between end cap and piezo actuator (Figure C.2). Later, the gap between end cap and piezo actuator was filled with adhesive, too. To obtain a prestress of about 0.8 MPa without any voltage applied (like originally planned), a voltage of -80 V was applied to the piezo actuator during curing of the adhesive. The pictures taken with a Fizeau interferometer (Zygo Corporation, VerifireTM), also reveal that the end cap got distorted during the failed bonding procedure. The consequence was that the end cap had not the required flatness for optically contacting. Therefore, the cavity mirror was glued to the end cap instead of optically contacting it.

Due to the described problems with the first bonded prestressed actuator, the bonding procedure of the other actuator and end cap was slightly modified. The spacing tube and piezo actuator were firstly bonded to the end cap and not to the spacer. This assembly was examined with the Fizeau interferometer. Only after it was checked that piezo surface and spacing tube surface are parallel to each other and that the piezo contract as expected when applying a negative voltage, the assembly was bonded to the spacer. This could be accomplished without any problems and the mirror could be optically contacted to the end cap as planned.

In conclusion, the actuators incorporated in the prestressed piezo cavity are both prestressed with about 0.8 MPa. For one actuator the prestressing was achieved as planned by hydroxide bonding of the spacer parts, for the other actuator adhesive had to be used. It remains to be examined if the use of adhesive affects the performance of the cavity.

C. Assembly of the prestressed cavity

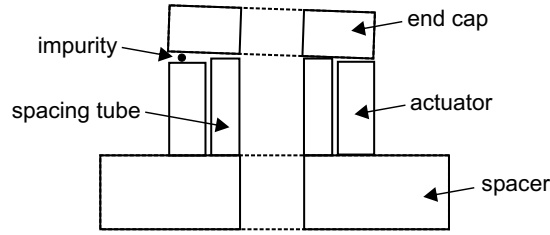


Figure C.1.: Sketch of the bond failure.

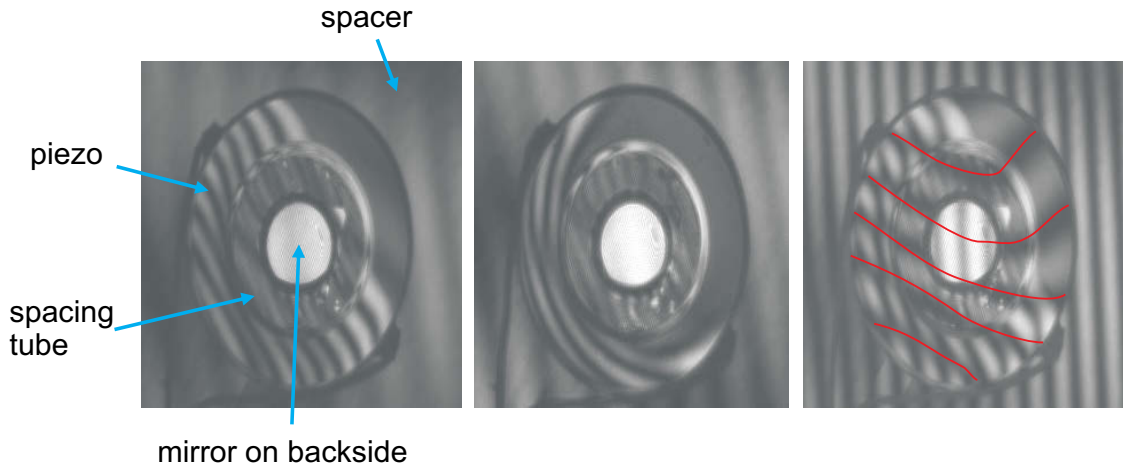
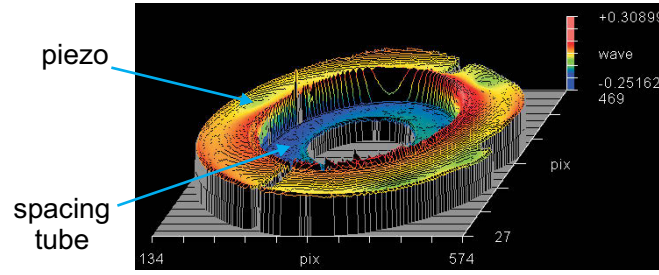
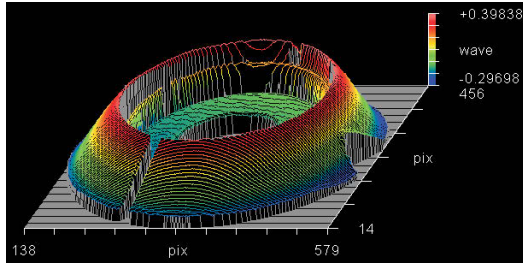


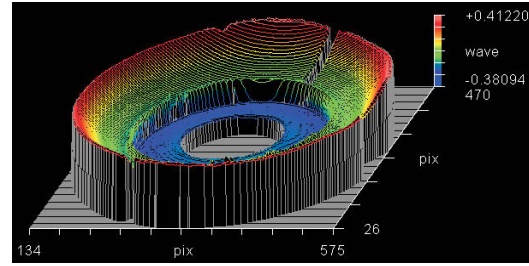
Figure C.2.: Top view on the end cap taken with a Fizeau interferometer. The piezo actuator and the spacing tube are visible, while the transparent end cap lying on top of them cannot be seen. For the picture on the left and in the center, the reference plate of the Fizeau interferometer was leveled with the spacer. Left: No voltage applied to the actuator. The tilting between the end cap and the piezo is visible due to the interference pattern. At the area where the piezo actuator is in contact with the end cap, no interference pattern is present, the remaining part shows roughly eight fringes. With this information the tilting of the end cap can be estimated and the maximum gap can be calculated to $h = 8 \cdot \lambda/2 = 2.53 \mu\text{m}$. Center: When a voltage of 200 V is applied to the actuator, the area where actuator and end cap are in contact increases and only three fringes are visible. The maximum gap is thus $3 \cdot \lambda/2 = 0.95 \mu\text{m}$. The difference of $1.58 \mu\text{m}$ fits pretty well with the piezo tuning range of $1.5 \mu\text{m}$ at 200 V. The distortion of the fringe pattern is in line with deformations observed in a non-prestressed actuator (Figure C.3). Right: This picture was taken while the Fizeau interferometer was leveled with the surface of the end cap. The non parallel interference fringes (highlighted in red) show that the end cap got distorted during the failed bonding procedure.



(a) 0 V



(b) 100 V



(c) -100 V

Figure C.3.: 3-D plot of the end cap assembly. The 3-D plot is provided by the software of the Zygo Verifire™. The assembly is such mounted that the surfaces of the actuator and the spacing tube can be examined, the end cap is not visible. Plot (a) was taken without any voltage applied to the actuator. The surfaces of spacing tube and actuator are parallel, which indicates a proper bond contact. By slowly increasing the voltage to -200 V and counting the interference fringes which pass through, it could be checked that the actuator contracts as much as expected. Furthermore, it could be observed that the piezo actuator does not expand and contract uniformly. The inner side of the ring moves a longer distance, so that the actuator surface is no longer plane. The length difference is about 440 nm at 100 V (b) and about 340 nm at -100 V (c). This behavior, which was already observed in Figure C.2, is not described in literature and no explanation could be found. However, since this effect was assumed to be not critical in the prestressed configuration, it was not deeper investigated.

Bibliography

- [1] A. Einstein. Die Grundlage der allgemeinen Relativitätstheorie. *Annalen der Physik*, 4(49):284, 1916.
- [2] R. A. Hulse and J. H. Taylor. Discovery of a pulsar in a binary system. *The Astrophysical Journal*, 195:L51, January 1975.
- [3] J. Weber. Detection and Generation of Gravitational Waves. *Physical Review*, 117(1):306–313, January 1960.
- [4] B. P. Abbott et al. LIGO: the Laser Interferometer Gravitational-Wave Observatory. *Reports on Progress in Physics*, 72(7):076901, July 2009.
- [5] H. Grote. The GEO 600 status. *Classical and Quantum Gravity*, 27(8):084003, April 2010.
- [6] F. Acernese et al. Virgo status. *Classical and Quantum Gravity*, 25(18):184001, September 2008.
- [7] P. Bender, A. Brillet, I. Ciufolini, A. M. Cruise, C. Cutler, K. Danzmann, F. Fidecaro, W. M. Folkner, J. Hough, P. McNamara, M. Peterseim, D. Robertson, M. Rodrigues, A. Rüdiger, M. Sandford, G. Schäfer, R. Schilling, B. Schutz, C. Speake, R. T. Stebbins, T. Sumner, P. Touboul, J. Y. Vinet, S. Vitale, H. Ward, and W. Winkler. LISA Pre-Phase A Report. *Max Planck Institut für Quantenoptik Report*, MPQ 233, 1998.
- [8] ESA. LISA Unveiling a hidden Universe. *ESA/SRE-3*, 2011.
- [9] R. W. P. Drever, J. L. Hall, F. V. Kowalski, J. Hough, G. M. Ford, A. J. Munley, and H. Ward. Laser phase and frequency stabilization using an optical resonator. *Applied Physics B Photophysics and Laser Chemistry*, 31(2):97–105, June 1983.
- [10] J. L. Hall, L.-S. Ma, M. Taubman, B. Tiemann, F.-L. Hong, O. Pfister, and J. Ye. Stabilization and frequency measurement of the I/sub 2/-stabilized Nd:YAG laser. *IEEE Transactions on Instrumentation and Measurement*, 48(2):583–586, April 1999.
- [11] R. Kohlhaas, T. Vanderbruggen, S. Bernon, A. Bertoldi, A. Landragin, and P. Bouyer. Robust laser frequency stabilization by serrodyne modulation. *Optics letters*, 37(6):1005–7, March 2012.
- [12] J. Ye and J. L. Hall. Optical phase locking in the microradian domain: potential applications to NASA spaceborne optical measurements. *Optics Letters*, 24(24):1838, December 1999.

Bibliography

- [13] F. Kéfélian, H. Jiang, P. Lemonde, and G. Santarelli. Ultralow-frequency-noise stabilization of a laser by locking to an optical fiber-delay line. *Optics letters*, 34(7):914–6, April 2009.
- [14] B. S. Sheard, G. Heinzel, and K. Danzmann. LISA long-arm interferometry: an alternative frequency pre-stabilization system. *Classical and Quantum Gravity*, 27(8):084011, April 2010.
- [15] J. I. Thorpe, K. Numata, and J. Livas. Laser frequency stabilization and control through offset sidebandlocking to optical cavities. *Optics express*, 16(20):15980–15990, 2008.
- [16] B. G. Lindsay, K. A. Smith, and F. B. Dunning. Control of long-term output frequency drift in commercial dye lasers. *Review of Scientific Instruments*, 62(6):1656, 1991.
- [17] L. Conti, M. De Rosa, and F. Marin. High-spectral-purity laser system for the AURIGA detector optical readout. *JOSA B*, 20(3):462, 2003.
- [18] Y. Li, T. Ido, T. Eichler, and H. Katori. Narrow-line diode laser system for laser cooling of strontium atoms on the intercombination transition. *Applied Physics B: Lasers and Optics*, 78(3-4):315–320, February 2004.
- [19] Y. Y. Jiang, A. D. Ludlow, N. D. Lemke, R. W. Fox, J. A. Sherman, L.-S. Ma, and C. W. Oates. Making optical atomic clocks more stable with 10-16-level laser stabilization. *Nature Photonics*, 5(3):158–161, January 2011.
- [20] T. Kessler, C. Hagemann, C. Grebing, T. Legero, U. Sterr, F. Riehle, M. J. Martin, L. Chen, and J. Ye. A sub-40-mHz-linewidth laser based on a silicon single-crystal optical cavity. *Nature Photonics*, 6(10):687–692, September 2012.
- [21] B. C. Young, F. C. Cruz, W. M. Itano, and J.C. Bergquist. Visible Lasers with Subhertz Linewidths. *Physical Review Letters*, 82(19):3799–3802, May 1999.
- [22] J. Millo, D. Magalhães, C. Mandache, Y. Le Coq, E. M. L. English, P. Westergaard, J. Lodewyck, S. Bize, P. Lemonde, and G. Santarelli. Ultrastable lasers based on vibration insensitive cavities. *Physical Review A*, 79(5):1–7, May 2009.
- [23] S. A Webster, M. Oxborrow, S. Pugla, J. Millo, and P. Gill. Thermal-noise-limited optical cavity. *Physical Review A*, 77(3):33847, March 2008.
- [24] A. D. Ludlow, X. Huang, M. Notcutt, T. Zanon-Willette, S. M. Foreman, M. M. Boyd, S. Blatt, and J. Ye. Compact, thermal-noise-limited optical cavity for diode laser stabilization at 1×10^{-15} . *Optics letters*, 32(6):641–3, March 2007.
- [25] B. Schutz. *A First Course in General Relativity*. Cambridge University Press, 2009.
- [26] É. É. Flanagan and S. A. Hughes. The basics of gravitational wave theory. *New Journal of Physics*, 7:204–204, September 2005.
- [27] LISA Mission Science Office. LISA : Probing the Universe with Gravitational Waves. *LISA-LIST-RP-436*, 2007.

- [28] B. S. Sheard, M. B. Gray, D. E. McClelland, and D. A. Shaddock. Laser frequency stabilization by locking to a LISA arm. *Physics Letters A*, 320(1):9–21, December 2003.
- [29] M. Herz. Active laser frequency stabilization and resolution enhancement of interferometers for the measurement of gravitational waves in space. *Optical Engineering*, 44(9):90505, September 2005.
- [30] K. McKenzie, R. E. Spero, and D. A. Shaddock. Performance of arm locking in LISA. *Physical Review D*, 80(10):1–28, November 2009.
- [31] M. Tinto and Sanjeev V. Dhurandhar. Time-Delay Interferometry. *Living Rev. Relativity*, 8:51, September 2005.
- [32] M. Tinto, F. B. Estabrook, and J. W. Armstrong. Time-delay interferometry for LISA. *Physical Review D*, 65(8):1–12, April 2002.
- [33] ESTEC. High power laser for LISA. *LISA-EST-SW-761*, 2009.
- [34] J. C. Livas, J. I. Thorpe, K. Numata, S. Mitryk, G. Mueller, and V. Wand. Frequency-tunable pre-stabilized lasers for LISA via sideband locking. *Classical and Quantum Gravity*, 26(9):094016, May 2009.
- [35] H. Jiang, F. Kéfélian, P. Lemonde, A. Clairon, and G. Santarelli. An agile laser with ultra-low frequency noise and high sweep linearity. *Optics Express*, 18(4):3284, February 2010.
- [36] G. Heinzel, V. Wand, A. García, O. Jennrich, C. Braxmaier, D. Robertson, K. Middleton, D. Hoyland, A. Rüdiger, R. Schilling, U. Johann, and K. Danzmann. The LTP interferometer and phasemeter. *Classical and Quantum Gravity*, 21(5):S581–S587, March 2004.
- [37] D. Weise. *Preparation and Highly Sensitive Detection of Ultracold Molecules*. PhD thesis, Universität Konstanz, 2004.
- [38] F. Riehle. *Frequency Standards: Basics and Applications*. Wiley-VCH, 2004.
- [39] A. Foltynowicz. *Fiber-laser-based Optical Heterodyne Molecular Spectrometry*. PhD thesis, UmeåUniversity, 2009.
- [40] H. Kogelnik and T. Li. Laser Beams and Resonators. *Applied Optics*, 5(10):1550, October 1966.
- [41] T. Day, E. K. Gustafson, and R. L. Byer. Sub-Hertz relative frequency stabilization of two diode laser pumped Nd:YAG lasers locked to a Fabry-Pérot interferometer. *J. Quant. Electr.*, 28:1106–1117, 1992.
- [42] R. V. Pound. Electronic frequency stabilization of microwave oscillators. *Review of Scientific Instruments*, 17(11):490–505, November 1946.

Bibliography

- [43] M. J. Lawrence, B. Willke, M. E. Husman, E. K. Gustafson, and R. L. Byer. Dynamic response of a Fabry- Perot interferometer. *Journal of the Optical Society of America B*, 16(4):523–532, April 1999.
- [44] E. D. Black. An introduction to Pound-Drever-Hall laser frequency stabilization. *American Journal of Physics*, 69(1):79, 2001.
- [45] D. Damjanovic. Hysteresis in Piezoelectric and Ferroelectric Materials. In *The Science of Hysteresis*, volume 3, pages 337–465. Academic Press, Oxford, 2006.
- [46] A. L. Kholkin, N. A. Pertsev, and A. V. Goltsev. Piezoelectricity and Crystal Symmetry. In *Piezoelectric and acoustic materials for transducers applications*, pages 17–39. Springer, 2008.
- [47] M. E. Lines and A. M. Glass. *Principles and Applications of Ferroelectrics and Related Materials*. The International series of monographs on physics. Oxford University Press, Oxford, February 2001.
- [48] G. Helke and K. Lubitz. Piezoelectric PZT Ceramics. In *Piezoelectricity*, chapter 4, pages 89–130. Springer Berlin Heidelberg, 2008.
- [49] S. Vieira. The behavior and calibration of some piezoelectric ceramics used in the STM. *IBM Journal of Research and Development*, 30(5):553–556, September 1986.
- [50] PI. Designing with Piezoelectric Transducers : Nanopositioning Fundamentals, 2005.
- [51] PI Ceramic. Piezoelectric Actuators - Components, Technologies, Operation, 2012.
- [52] M. Cerdonio, L. Conti, A. Heidmann, and M. Pinard. Thermoelastic effects at low temperatures and quantum limits in displacement measurements. *Physical Review D*, 63(8):1–9, March 2001.
- [53] H. Müller, S. Herrmann, T. Schuldt, M. Scholz, E. V. Kovalchuk, and A. Peters. Offset compensation by use of amplitude-modulated sidebands in optical frequency standards. *Optics letters*, 28(22):2186–8, November 2003.
- [54] S. Herrmann. *A Michelson-Morley Test of Lorentz Invariance Using a Rotating Optical Cavity*. PhD thesis, Humboldt-Universität zu Berlin, 2007.
- [55] S. T. Dawkins and A. N. Luiten. Single actuator alignment control for improved frequency stability of a cavity-based optical frequency reference. *Applied optics*, 47(9):1239, March 2008.
- [56] D. A. Shaddock, M. B. Gray, and D. E. McClelland. Frequency locking a laser to an optical cavity by use of spatial mode interference. *Optics letters*, 24(21):1499–501, November 1999.
- [57] C. Braxmaier. *Fundamentale Tests der Physik mit ultrastabilen optischen Oszillatoren*. PhD thesis, Universität Konstanz, August 2001.

- [58] W. Lewoczko-Adamczyk, M. Schiemangk, H. Müller, and A. Peters. Thermoacoustic optical path length stabilization in a single-mode optical fiber. *Applied Optics*, 48(4):704, January 2009.
- [59] J. L. Hall, M. S. Taubman, and J. Ye. Laser Stabilization. In Michael Bass, Jay M Enoch, Eric W Van Stryland, and William L Wolfe, editors, *Handbook of optics*, volume 2, chapter 22, pages 1–34. OSA, 2001.
- [60] K. Numata, A. Kemery, and J. Camp. Thermal-Noise Limit in the Frequency Stabilization of Lasers with Rigid Cavities. *Physical Review Letters*, 93(25):250602–1–4, December 2004.
- [61] R. Fleddermann, M. Tröbs, F. Steier, G. Heinzl, and K. Danzmann. Intrinsic Noise and Temperature Coefficients of Selected Voltage References. *IEEE Transactions on Instrumentation and Measurement*, 58(6):2002–2007, June 2009.
- [62] P. Horowitz and W. Hill. *The Art of Electronics*. Cambridge University Press, 1989.
- [63] H. D. Baehr and K. Stephan. *Wärme- und Stoffübertragung*. Springer Berlin Heidelberg, 2006.
- [64] F. M. Phelps. Airy Points of a Meter Bar. *American Journal of Physics*, 34(5):419, 1966.
- [65] L. Chen, J. L. Hall, J. Ye, T. Yang, E. Zang, and T. Li. Vibration-induced elastic deformation of Fabry-Perot cavities. *Physical Review A*, 74(5):1–13, November 2006.
- [66] S. Grede. Aufbau und Charakterisierung von Komponenten eines mobilen Atominterferometers (Diplomarbeit), Humboldt-Universität zu Berlin, 2009.
- [67] M. Notcutt, L.-S. Ma, J. Ye, and J. L. Hall. Simple and compact 1-Hz laser system via an improved mounting configuration of a reference cavity. *Optics letters*, vol(14):30pp1815–1817, July 2005.
- [68] K. Döringshoff, K. Möhle, M. Nagel, E. V. Kovalchuk, and A. Peters. High Performance Iodine Frequency Reference for Tests of the LISA Laser System. *Proceedings of EFTF*, 2010.
- [69] S. Herrmann, A. Senger, K. Möhle, M. Nagel, E. V. Kovalchuk, and A. Peters. Rotating optical cavity experiment testing Lorentz invariance at the 10⁻¹⁷ level. *Physical Review D*, 80(10):105011, November 2009.
- [70] P. C. D. Hobbs. *Building Electro-Optical Systems: Making It all Work*. John Wiley & Sons, Inc., 2000.
- [71] B. Burghardt, W. Jitschin, and G. Meisel. Precise rf tuning for cw dye lasers. *Applied Physics*, 20(2):141–146, October 1979.
- [72] P. Bohlouli-Zanjani, K. Afrousheh, and J. D. D. Martin. Optical transfer cavity stabilization using current-modulated injection-locked diode lasers. *Rev. Sci. Instrum.*, 77(9):93105, June 2006.

Bibliography

- [73] F. Rohde, M. Almendros, C. Schuck, J. Huwer, M. Hennrich, and J. Eschner. A diode laser stabilization scheme for $40\text{ Ca} + \text{single-ion spectroscopy}$. *Journal of Physics B: Atomic, Molecular and Optical Physics*, 43(11):115401, June 2010.
- [74] T. C. Briles, D. C. Yost, A. Cingöz, J. Ye, T. R. Schibli, and A. Cing. Simple piezoelectric-actuated mirror with 180 kHz servo bandwidth. *Optics express*, 18(10):9739–46, May 2010.
- [75] W. M. Folkner, G. DeVine, W. M. Klipstein, K. McKenzie, D. A. Shaddock, R. E. Spero, R. Thompson, D. Wuchenich, N. Yu, M. Stephens, J. Leitch, M. Davis, J. DeCino, C. Pace, and R. Pierce. Laser frequency stabilization for GRACE-II. In *EFTF 2010*, pages 1–8. Jet Propulsion Laboratory, National Aeronautics and Space Administration, 2010.
- [76] P. Hartmann, K. Nattermann, T. Döhring, R. Jedamzik, M. Kuhr, P. Thomas, G. Kling, and S. Lucarelli. ZERODUR Glass Ceramics for High Stress Applications. *Proceedings of SPIE*, 7425:74250M1–11, August 2009.
- [77] D.-H. Gwo. Ultra-precision and reliable bonding method, Patent US 6,284,085 B1, January 2001.
- [78] D.-H. Gwo. Hydroxide-catalyzed bonding, Patent US 6,548,176 B1, 2003.
- [79] E.J. Elliffe, J. Bogenstahl, A. Deshpande, J. Hough, C. Killow, S. Reid, D. Robertson, S. Rowan, H. Ward, and G. Cagnoli. Hydroxide-catalysis bonding for stable optical systems for space. *Classical and Quantum Gravity*, 22(10):S257–S267, May 2005.
- [80] K. Haughian and M. Van Veggel. Collated strength Data on Hydroxide Catalysis Bonding. Technical report, LIGO Laboratory / LIGO Scientific Collaboration, 2008.
- [81] N. L. Beveridge, A. A. van Veggel, M. Hendry, P. Murray, R. A. Montgomery, E. Jesse, J. Scott, R. B. Bezensek, L. Cunningham, J. Hough, R. Nawrodt, S. Reid, and S. Rowan. Low-temperature strength tests and SEM imaging of hydroxide catalysis bonds in silicon. *Classical and Quantum Gravity*, 28(8):085014, April 2011.
- [82] D. Zhou, M. Kamlah, and D. Munz. Effects of uniaxial prestress on the ferroelectric hysteretic response of soft PZT. *Journal of the European Ceramic Society*, 25(4):425–432, April 2005.
- [83] Z. W. Barber, W. R. Babbitt, B. Kaylor, R. R. Reibel, and P. A. Roos. Accuracy of active chirp linearization for broadband frequency modulated continuous wave ladar. *Applied optics*, 49(2):213–9, January 2010.
- [84] M. Goldfarb and N. Celanovic. Modeling piezoelectric stack actuators for control of micro-manipulation. *IEEE Control Systems Magazine*, 17(3):69–79, June 1997.
- [85] H. Janocha and K. Kuhnen. Real-time compensation of hysteresis and creep in piezoelectric actuators. *Sensors and Actuators A: Physical*, 79(2):83–89, February 2000.

- [86] L.-S. Ma, J. Ye, P. Dubé, and J. L. Hall. Ultrasensitive frequency-modulation spectroscopy enhanced by a high-finesse optical cavity: theory and application to overtone transitions of C₂H₂ and C₂HD. *Journal of the Optical Society of America B*, 16(12):2255, December 1999.
- [87] J. Ye, L.-S. Ma, and J. L. Hall. High-resolution frequency standard at 1030 nm for Yb:YAG solid-state lasers. *Journal of the Optical Society of America B*, 17(6):927, June 2000.
- [88] A. Czajkowski, A.A. Madej, and P. Dubé. Development and study of a 1.5 μ m optical frequency standard referenced to the P(16) saturated absorption line in the ($\nu_1+\nu_3$) overtone band of ¹³C₂H₂. *Optics Communications*, 234(1-6):259–268, April 2004.
- [89] M. Tröbs and G. Heinzel. Improved spectrum estimation from digitized time series on a logarithmic frequency axis. *Measurement*, 39(2):120–129, February 2006.
- [90] J. Rutman and F. L. Walls. Characterization of frequency stability in precision frequency sources. *Proceedings of the IEEE*, 79(7):952–960, July 1991.

List of Figures

1.1. LISA - artistic impression	1
1.2. Piezo-tunable cavity	2
2.1. Effect of a gravitational wave with $+$ or \times polarization	7
2.2. LISA measurement band	8
2.3. LISA satellite constellation	9
2.4. Variation of the satellite distance	10
2.5. Variation in the velocity between the satellites leading to doppler shifts	10
2.6. LISA frequency noise reduction	11
2.7. Self phase locking scheme	12
2.8. Scheme of an unequal arm length interferometer	13
3.1. Fabry-Pérot Cavity	17
3.2. Airy function	20
3.3. Feedback control loop	22
3.4. Laser frequency stabilization with the Pound Drever Hall technique	23
3.5. PDH error signal	25
3.6. Deformation of a piezoelectric crystal	27
3.7. Perovskite structure of the PZT ceramic.	30
3.8. Domain structure of a ferroelectric ceramic	30
3.9. Polarization hysteresis loop	31
3.10. Strain hysteresis butterfly loop	31
3.11. Morphotropic phase transition in PZT	34
3.12. Types of piezoelectric actuators	35
4.1. Modifications of the piezo actuators for proper wiring	41
4.2. Details on the assembly of the piezo-tunable cavities.	42
4.3. Pictures of the cavities with incorporated piezo actuator	43
4.4. Influence of amplitude changes of the error signal.	47
4.5. Modification of the error signal by a parasitic resonator and RAM.	49
4.6. Simulation of the cavity deformation due to gravity	53
4.7. Amplifier noise model and amplifier with feedback	57
4.8. Photograph of the complete setup	59
4.9. Temperature stability on the thermal shields	63
4.10. Mounting of the cavities	64
4.11. Seismic noise and effect of vibration isolation	65
4.12. Optical setup	66

4.13. Performance of the PDH detectors	67
4.14. Reference cavities.	68
5.1. Influence of cavity losses	71
5.2. Beat cavity with PZN-PT actuator and the ULE reference	73
5.3. Influence of drift removal on ASD and Allan deviation	73
5.4. ASDs of the piezo-tunable cavities	74
5.5. Allan deviations of the piezo-tunable cavities	75
5.6. FSR lock of the cavity with PZT stack actuator	77
5.7. Sensitivity to intensity changes	78
5.8. Influence of parasitic resonators	79
5.9. Quadrature components of the RAM Signal	80
5.10. Influence of pressure changes	81
5.11. Scheme of the cavity with PZT tube actuator with gluing bridges.	82
5.12. Temperature noise converted to frequency noise	83
5.13. Influence of vibrations on the frequency stability	84
5.14. Tilt sensitivity and tilt fluctuations	87
5.15. Summary of influences on the frequency stability in the low frequency range . . .	88
5.16. Voltage noise of the OP27G operational amplifier	90
5.17. Frequency noise with applied voltage	90
5.18. Frequency separating filter	91
5.19. Slow frequency scan	92
5.20. Hysteresis of the cavity with PZT stack actuator.	93
5.21. Creep of the cavity with PZN-PT actuator	94
5.22. Tuning behavior of the cavity with quartz actuator	95
5.23. Scheme of possible electrostatic effects of the cavity with quartz piezo	95
5.24. Stabilization of the piezo-tunable cavity	97
5.25. ASD of the stabilized cavity	98
6.1. Photograph of the cavity with prestressed piezo actuator	101
6.2. Model of the cavity with prestressed piezo actuator (exploded view)	102
6.3. Schematic of the prestressed piezo actuator	103
6.4. Deformation of the cavity with prestressed piezo actuator (simulation)	105
6.5. Bonding procedure of the cavity with prestressed actuators	107
6.6. Mechanical resonances of the cavity with prestressed actuators	109
6.7. ASD and relative Allan deviation of the cavity with prestressed actuators	110
6.8. ASD of the cavity with prestressed piezo actuators while modulated	111
6.9. Modified PDH locking scheme	112
C.1. Sketch of the bond failure	122
C.2. Fizeau interferometer measurements	122
C.3. 3D plot of the end cap assembly	123

List of Tables

4.1. List of the applied piezo actuators	39
4.2. Relevant properties of the piezo materials used in this work	40
4.3. Details on the cavity assembly	42
4.4. Specifications of the piezo-tunable cavities assembled within this work	43
4.5. Estimated thermal expansion coefficients of the cavities	51
4.6. Estimated vibration sensitivity	52
4.7. Estimated tilt sensitivities	54
4.8. Thermal noise of the single cavity components	55
4.9. Calculated thermal noise limit of the different cavities	55
4.10. Summary of the calculated cavity properties and sensitivities	58
5.1. Properties of the different piezo-tunable cavities	69
5.2. Thermal expansion coefficients of the cavities.	82
5.3. Vibration sensitivity	85
5.4. Tuning coefficients	89
5.5. Maximum opening in the hysteresis curve in dependence of the applied voltage .	93
6.1. Properties of the cavity with prestressed piezo actuators	108
A.1. Characteristic slopes of different noise types in the ASD and Allan deviation . .	118

List of Abbreviations

AOM	acousto-optic modulator
ASD	amplitude spectral density
CTE	coefficient of thermal expansion
FS	fused silica
FSR	free spectral range
FWHM	full width at half maximum
HV	high voltage
LISA	Laser Interferometer Space Antenna
MPB	morphotropic phase boundary
NGO	New Gravitational Wave Observatory
PBS	polarizing beam splitter
PDH	Pound Drever Hall
PZN-PT	lead zinc niobate - lead titanate
PZT	lead zirconate titanate
RAM	residual amplitude modulation
TDI	time delay interferometry
TEM	transverse electromagnetic
ULE	ultra low expansion glass

Danksagung

Zum Schluss möchte ich mich ganz herzlich bei all denjenigen bedanken, die zum Gelingen dieser Arbeit beigetragen haben.

Zuallererst gilt mein Dank meinem Betreuer Achim Peters, der mich und mein Projekt all die Jahre mit seinem unerschöpflichen Fachwissen, seinen wertvollen Ideen und seiner ansteckenden Begeisterung begleitet und vorangebracht hat.

Besonderer Dank gebührt meinen Kollegen Moritz Nagel, Evgeny Kovalchuk und Klaus Döringshoff für die vielen wertvollen Diskussionen und die tatkräftige Hilfe im Labor. Ohne Moritz wären die vielen Stunden im Labor weniger ergiebig und auch deutlich langweiliger gewesen. Es hat mich sehr gefreut all die großen und kleinen Fragen der Physik und des restlichen Lebens mit ihm besprechen zu können. Auch für das ausführliche Korrekturlesen dieser Arbeit und die vielen nützlichen Anmerkungen bin ich sehr dankbar. Bei Evgeny bedanke ich mich vielmals für die vielen hilfreichen fachlichen Anregungen, die immer bereitwillig gewährte Unterstützung im Labor, die fürsorgliche Atmosphäre im Büro als auch für die wertvollen Korrekturen und Anmerkungen zu dieser Arbeit.

All meinen Kollegen danke ich für die hervorragende Atmosphäre in unserer Arbeitsgruppe. Die beinahe uneingeschränkte Hilfsbereitschaft, die gegenseitige Unterstützung und die vielen netten Gespräche habe ich immer sehr zu schätzen gewusst. Mein Dank gilt dabei auch Klaus Palis, der mir nicht nur bei elektronischen Problemen immer gerne weiterhalf.

Der Aufbau des Resonators mit vorgespanntem Piezoaktuator wäre ohne die Hilfe des Albert Einstein Instituts in Hannover nicht möglich gewesen. Ich möchte mich herzlich bei Johanna Bogenstahl bedanken, die das *hydroxide catalysis bonding* mit mir durchgeführt und mich bei den auftretenden Problemen tatkräftig unterstützt hat.

Mein besonderer Dank gilt auch Sven Herrmann für das Zurverfügungstellen des Zygo Interferometers und vor allem für das unermüdliche Korrekturlesen dieser Arbeit.

Nicht zuletzt möchte ich meiner Familie danken, besonders meinem Mann Max für dessen Unterstützung, Verständnis und Liebe. Es ist schön Menschen zu haben, die einfach immer für einen da sind.

Selbständigkeitserklärung

Ich erkläre, dass ich die vorliegende Arbeit selbständig und nur unter Verwendung der angegebenen Literatur und Hilfsmittel angefertigt habe. Ich habe mich anderweitig nicht um einen Doktorgrad beworben und besitze einen solchen auch nicht. Die dem Verfahren zugrunde liegende Promotionsordnung der Mathematisch-Naturwissenschaftlichen Fakultät I der Humboldt-Universität zu Berlin habe ich zur Kenntnis genommen.

Berlin, den 05.02.2013

Katharina Möhle